Fabrication of Photonic Crystal Structures for Optical Semiconductor Devices by Single Pulse Laser Interference Lithography

Zhiheng Lin

A thesis submitted in fulfilment of the requirements for the degree of

Doctor of Philosophy

Department of Electronic and Electrical Engineering

The University of Sheffield

April 2024

Abstract

Photonic crystal (PhC) structures formed by periodic surface nanostructuring have emerged as pivotal elements for controlling light-matter interactions. One important application is to mitigate losses due to the high surface reflectivity of semiconductor optoelectronic devices, for example, improving light absorption within photovoltaic cells or light extraction from light-emitting diodes (LEDs). Many methods have been established for the successful synthesis of PhC structures. Among them, single pulse laser interference lithography (LIL) is lauded for its simplicity and cost-efficiency, mitigating the financial constraints of nanofabrication. Moreover, it is recognized for its temporal efficiency, enabling rapid fabrication processes. Additionally, its capability to pattern over large areas further enhances its applicability in industrial-scale production.

In the first part of the thesis, we have employed single pulse LIL to fabricate antireflective PhC structures on GaAs substrates using a commercial photoresist. Exposure is performed with single (7 nanosecond, 355 nm pulses) of relatively low energy (<10 mJ). High-quality nanohole arrays of pitch of approximately 365 nm are fabricated following inductively coupled plasma (ICP) etching of the exposed photoresist. Reflectivity analyses confirmed that these structures reduce the average reflectance of GaAs to below 5% across the 450 nm to 700 nm visible wavelength range. PhC structures developed through this innovative high-throughput approach demonstrate considerable potential in elevating light extraction efficiency in LED applications and enhancing light trapping in solar cell technologies.

In the second part, we have effectively applied single pulse LIL to create PhC structures on GaAs/AlGaAs LED structures to achieve high-quality nanohole arrays when combined with ICP etching. Electroluminescence (EL) analyses confirm that these structures enhance the average EL intensity of the LED by up to 3.5 times at room temperature. This empirical evidence underscores the efficacy and potential of this fabrication approach in advancing the functional capabilities of semiconductor-based light-emitting devices.

In the final part, we use the direct laser interference patterning (DLIP) method to perform in-situ patterning of an (Al)GaAs layer during MBE epitaxial growth to obtain precisely aligned

Quantum Rings (QRs). The structural parameters, including pitch, size, and dimensions of the QR arrays, have been analyzed using AFM. Furthermore, to evaluate the optical properties of the QRs, comprehensive analyses have been conducted using both temperature-dependent and power-dependent PL techniques. Preliminary assessments indicate that the DLIP technique can achieve precise QR arrays without compromising the intrinsic characteristics of the QRs, suggesting a promising avenue for the development of advanced optoelectronic devices.

Acknowledgments

This thesis represents not just an academic achievement but a journey that was made possible through the support and encouragement of many individuals. I would like to express my deepest gratitude to all those who have contributed to this.

Foremost, I extend my heartfelt thanks to my supervisor, Prof. Mark Hopkinson, whose expertise, and guidance have been invaluable throughout this journey. Professor Mark Hopkinson's contributions to my development extend far beyond the conventional roles of a supervisor. His deep understanding of the subject matter and keen insight into experimental methods have significantly shaped my research approach, enabling me to navigate complex challenges with confidence and precision. Beyond the realms of academia and experimentation, Professor Hopkinson has been a steadfast source of moral support, providing encouragement and motivation during moments of doubt and uncertainty. Furthermore, Professor Mark Hopkinson's assistance in manuscript preparation has been invaluable. His meticulous attention to detail, combined with an exceptional ability to convey complex ideas with clarity, has immeasurably improved the quality of my scholarly writings. His feedback has not only refined my work but has also imparted crucial skills in academic writing that will undoubtedly benefit my future. For all these reasons and more, I am deeply indebted to Professor Mark Hopkinson and consider his guidance to be one of the most significant factors in my growth and achievements as a scholar.

I am also deeply thankful to my colleague, Dr. Yunran Wang, for her collaborative spirit and instrumental support in our experiments. Her insights and expertise have significantly contributed to the success of our research. Moreover, Dr. Wang's ability to communicate complex concepts with ease and clarity has facilitated our collaborative discussions, enabling us to refine our hypotheses and experimental designs effectively. Her meticulous attention to detail and commitment to excellence have set a high standard within our research team, inspiring me to strive for the utmost quality in their work.

My gratitude also extends to Dr. Im Sik Ham for his assistance with epitaxial growth, a crucial aspect of our research.

I would also like to acknowledge the support and companionship of my colleague Mr. Yaoxun Wang, who support both in the laboratory and in life. His assistance in various experiments and his moral support have been greatly appreciated.

I am grateful to my former colleagues Prof. Tao Wang, Dr. Jie Bai, Dr. Kai Huang, Dr. Shuoheng Shen, Dr. Xuanming Zhao, Dr. Nicolas Poyiatzis, Dr. Suneal Ghataora, Dr. Ling Jiu, Dr. Chenqi Zhu, Dr. Peter Fletcher, Dr. Peng Feng, Dr. Ye Tian, Dr. Jack Haggar, Dr. Volkan Esendag, and Dr. Guillem Martinez de Arriba for their contributions to my academic journey. Their collective wisdom and guidance have enriched my research experience.

I would like to express my heartfelt gratitude to my bros, Dr. Zilei Chen, Dr. Yiren Wu, and Mr. Chenxin Zhang, for their unwavering support and invaluable assistance throughout my Ph.D. journey. Their help in both writing and life has been instrumental to my success.

Additionally, I extend my sincere thanks to my homeys Dr. Ye Cao, Dr. Jinggui Zhou, Dr. Zhitong Ran, Dr. Zhongyi Xia, Mr. Chenhao Li, Mr. Mengke Wu, Mr. Yilun Zhou, Miss Ruiman Ma, Miss Qingxin Hui, and Miss Zili Zhang for their continuous support and encouragement. Their collective efforts have greatly enriched my doctoral experience, and I am deeply grateful for their contributions.

Meanwhile, I would like to thank Mr. Wei Zhong, Mr. Ce Xu, Miss. Rongzi Ni, and Mr. Xinchi Chen for their camaraderie and assistance in various capacities throughout my time in the lab.

Last but certainly not least, I wish to express my profound appreciation to my family for their unwavering moral encouragement and support. Their belief in my capabilities and their constant encouragement have been the bedrock of my perseverance and success.

This thesis is a testament to the collaborative effort and collective support of all the individuals, to whom I am eternally grateful.

To my dearest

小竹子

and

小竹子妈妈

Contents

List of Publications

Journal Publications

1. Zhiheng Lin, Yun-Ran Wang, Yaoxun Wang, and Mark Hopkinson "Design and fabrication of photonic crystal structures by single pulse laser interference lithography", Optics and Laser Technology, 2024, Under review.
2. Zhiheng Lin, Yaoxun Wang, Yun-Ran Wang, Im Sik Han 1, and Mark Hopkinson " Photonic Crystal Enhanced Light Emitting Diodes Fabricated by Single Pulse Laser Interference Lithography", Journal of Applied physics, 2024, Under review.
3. Zhiheng Lin, Yaoxun Wang, Yun-Ran Wang, Im Sik Han 1, and Mark Hopkinson "Fabrication of photonic crystal structures on GaAs by single pulse laser interference Lithography", Journal of Laser Micro/Nanoengineering, 2024, Under review.

Conference Contributions

4. Zhiheng Lin, Yun-Ran Wang, Im Sik Han, Yaoxun Wang, and Mark Hopkinson "Fabrication of GaAs antireflective nanostructures by single pulse laser interference lithography", UK Semiconductors, Sheffield, UK, 2023
5. Im Sik Han, Yun-Ran Wang, Zhiheng Lin, Yaoxun Wang, and Mark Hopkinson "Fabrication of droplet epitaxial III-V nanostructure arrays using in situ direct laser interference patterning", UK Semiconductors, Sheffield, UK, 2023
6. Yaoxun Wang, Zhiheng Lin, Yun-Ran Wang, Im Sik Han, and Mark Hopkinson "Photoluminescence investigation of laser patterned InGaAs DE quantum dot arrays", UK Semiconductors, Sheffield, UK, 2023
7. Mark Hopkinson, Yunran Wang, Im Sik Han, Yaoxun Wang, and Zhiheng Lin "In-situ pulsed laser interference for the site-controlled growth of InGaAs quantum dots", EuroMBE, Madrid, Spain, 2023

List of Abbreviations

GaAs	Gallium arsenide
Si	Silicon
HEMTs	High Electron Mobility Transistors
LDs	Laser diodes
LEDs	Light-emitting diodes
QWs	Quantum wells
QDs	Quantum dots
DOS	Density of states
SEM	Scanning Electron Microscope
TEM	Transmission electron microscopy
QR	Quantum ring
AFM	Atomic force microscopy
PhCs	Photonic crystals
1D	One-dimensional
DBRs	Distributed Bragg reflectors
2D	Two-dimensional
VCSELs	Vertical-cavity surface-emitting lasers
3D	Three-dimensional
MBE	Molecular beam epitaxy
MOCVD	Metal-organic chemical vapour deposition
EBL	Electron beam lithography
NIL	Nanoimprint lithography
DPN	Dip-Pen Nanolithography
PL	Photoluminescence
EL	Electroluminescence
TE	Transverse electric

TM	Transverse magnetic
Fp	The Purcell factor
Q factor	The quality factor
LEE	Light extraction efficiency
LIL	Laser interference lithography
DOE	Diffractive optic elements
SLMs	Spatial Light Modulators
DLIL	Direct Laser Interference Lithography
UV	Ultraviolet
DUV	Deep ultraviolet
SiO2	Silicon dioxide
Si3N4	Silicon nitride
QCM	Quartz crystal monitor
RIE	Reactive ion etching
RF	Radiofrequency
µ-PL	Micro-photoluminescence
µ-EL	Micro-Electroluminescence
ARCs	Antireflective coatings
PBG	Photonic band gap
BMS	Burstein-Moss shift
AB	Aharonov-Bohm
QNs	Quantum nanostructures
DLIP	Direct laser interference lithography patterning

Chapter 1

Introduction

1.1 The Evolution of III-V Compound Semiconductors

III-V compound semiconductors, comprised of elements from groups III and V of the periodic table, have found extensive application in electronic and optoelectronic devices due to their exceptional electronic characteristics. By combining elements listed in Group III and Group V, a diverse range of III-V compound semiconductors can be formed, including InAs, InP, GaAs, GaN, AlAs, GaSb, and more. Figure 1.1 illustrates a collection of semiconductor materials alongside their corresponding band gap energy and lattice constant.

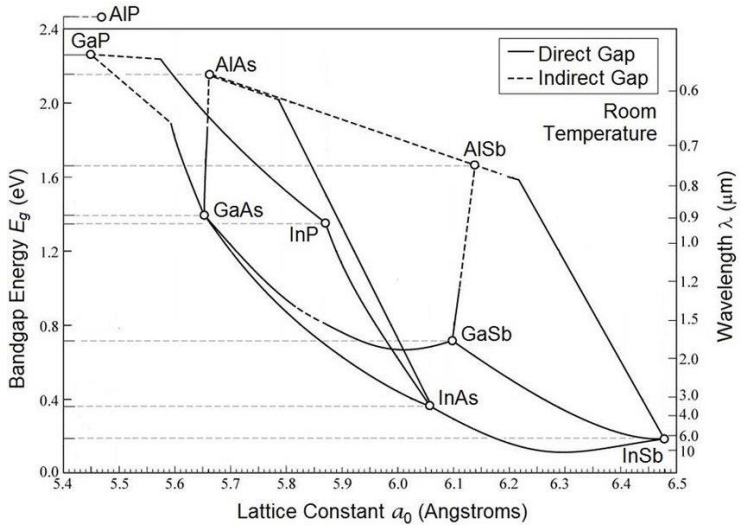

Figure1.1 The lattice constant and bandgap energy of different III-V semiconductors at room temperature (adapted from Tien, 1988)

In the late 19th century, French chemist Paul Emile Lecoq de Boisbaudran successfully synthesized Gallium arsenide (GaAs). Its semiconductor properties sparked investigations into potential applications in the 1950s. Throughout the 1950s and 1960s, researchers delved into III-V compounds such as GaAs and InP [1-3], revealing their exceptional attributes, including high electron mobility and superior performance compared to conventional elemental semiconductors like silicon (Si) [4].

The 1970s witnessed a significant milestone with the development of High Electron Mobility Transistors (HEMTs), key components for high-frequency and high-speed electronic devices that exhibited enhanced performance thanks to the incorporation of III-V materials [5-9]. Simultaneously, the 1960s and 1970s marked the advent of III-V compound semiconductor laser diodes (LDs) and light-emitting diodes (LEDs), bringing about a revolution in optoelectronics. These innovative devices unlocked various applications in telecommunications, optical data storage, and displays [10,11]. Researchers began employing quantum well structures in III-V compounds. Quantum wells (QWs), ultra-thin layers capable of precise control over electronic properties, contributed to notable improvements in laser diodes, detectors, and other optoelectronic devices [12-14].

In recent times, III-V compound semiconductors have ventured into nanotechnology as well as burgeoning domains like quantum computing [15-21]. Owing to their distinct electronic attributes, they stand out as promising materials for pioneering next-gen technologies. Within the realm of nanotechnology, these materials are incorporated into devices and structures at the nanoscale, offering improved computing power and energy efficiency.

Overall, the history of III-V compound semiconductors is marked by continuous research, development, and commercialization of advanced electronic and optoelectronic devices, cementing their place as essential materials in modern technology.

1.2 Semiconductor Nanostructures

Semiconductor nanostructures have been instrumental in shaping today's technological landscape. Through decades of dedicated research and development, these structures have undergone remarkable advancements, unleashing unparalleled possibilities across diverse fields.

The foundation for semiconductor physics and technology was established in the mid-20th century, driven by the groundbreaking contributions of visionaries like John Bardeen, Walter Brattain, and William Shockley. Their pivotal creation of the point-contact transistor in 1947 marked a monumental milestone, leading to the advent of the first commercial transistor in the early 1950s [22,23]. This revolutionary invention laid the groundwork for continuous exploration and advancement in the realm of semiconductor materials and devices.

During the late 1950s and 1960s, a profound exploration of quantum mechanics and its influence on electrons in solids commenced [24,25]. The significant exploration laid the foundation for the development of band theory, which granted a comprehensive comprehension of energy levels and offered researchers profound insights into the electronic properties of semiconductors.

From the 1980s to the 2000s, the development of semiconductor nanostructures, exemplified by QWs (1D confinement), quantum wires (2D confinement), and quantum dots (QDs) (3D confinement), played a pivotal role in driving the progress of optoelectronic devices [26-28]. Figure 1.2 provides schematic illustrations depicting the density of states (DOS) for bulk, 2D, 1D, and 0D materials. Quantum confinement effects in low-dimensional structures induce substantial changes in the DOS and energy band structure of these materials. The DOS represents the number of states per unit energy per unit volume and plays a crucial role in determining the energy distributions of carriers within a semiconductor.

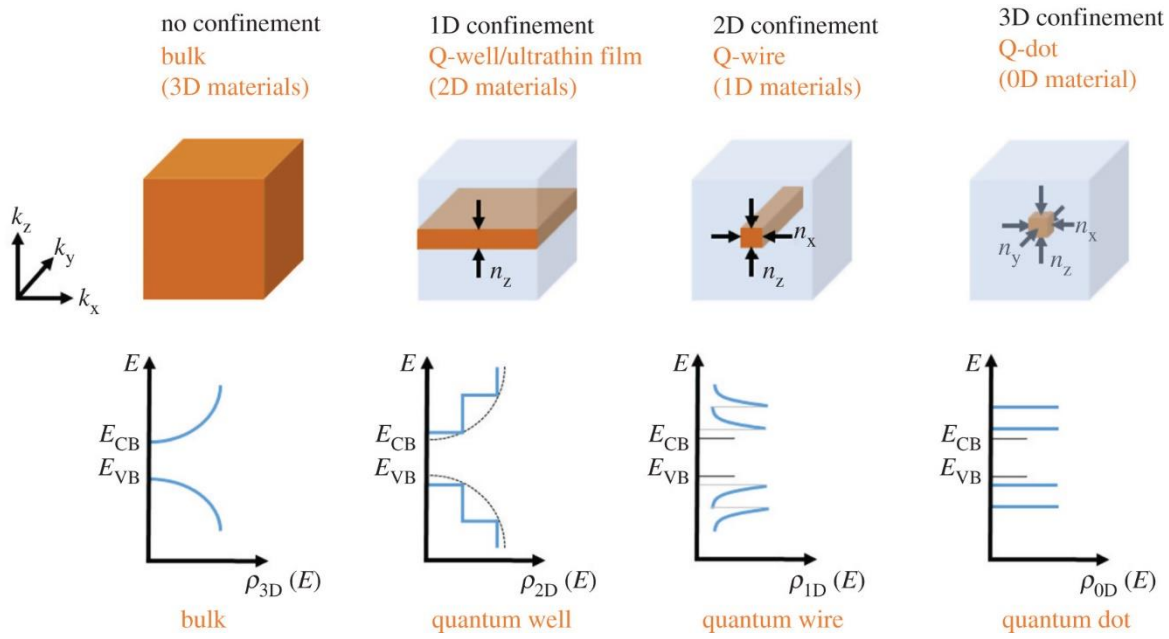

Figure 1.2 The density of states in different confinement configurations: bulk; quantum well; quantum wire; quantum dot [29].

QW nanostructures are typically composed of two different semiconductor materials with varying bandgaps, forming a layered structure. The central layer, known as the QW, is a thin region where electrons are confined in one dimension due to the potential energy barriers provided by the surrounding layers. This confinement leads to quantized energy levels. Figure 1.3 shows the QW band gap structure. III-V compound semiconductor QWs are essential in a wide range of applications, spanning from telecommunications and optoelectronics to high-speed electronic devices and advanced sensors [30]. Their unique electronic properties and tuneable bandgap make them valuable building blocks in various advanced technologies. Each QW structure has unique electronic and optical properties, leading to specific applications. Common QW structures are discussed below.

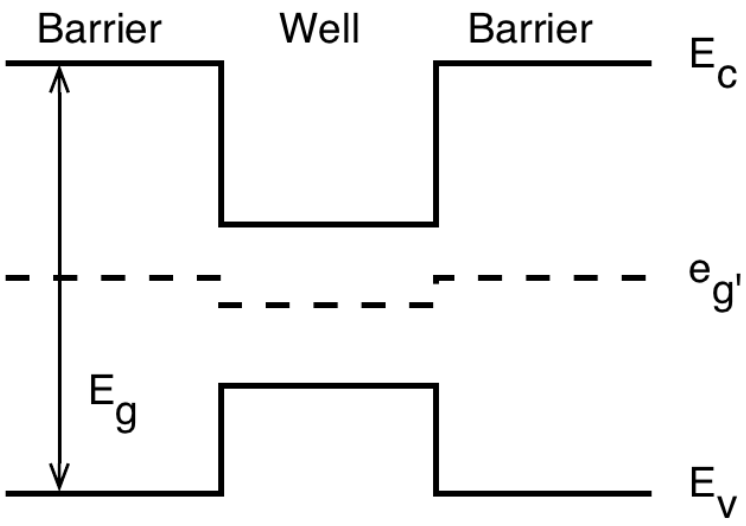

Figure 1.3 Quantum well bandgap structure [31]

The InGaAs/GaAs QWs exhibit a customizable bandgap, suitable for a diverse range of wavelength applications in the near infra-red range. Wavelength tunablity is achieved by adjusting the indium composition (x) in $In_xGa_{1-x}As$ QW. These quantum wells find extensive application in optoelectronic devices encompassing infrared LEDs [32], photodetectors [33] and optical communication devices such as lasers, optical amplifiers, optical switches and modulators [34].

Similarly, the GaAs/AlGaAs QW allows for bandgap engineering, enabling coverage across a wide spectrum of wavelengths, notably in the visible and near-infrared regions, accomplished by modifying the GaAs QW thickness in AlGaAs. This quantum well type finds widespread use in optoelectronic devices, such as visible lasers, visible LEDs [35], and other high-performance optoelectronic components.

For the InGaN/GaN quantum well, the addition of indium in InGaN enables a wide range of bandgap tunability, facilitating light emission across the visible and ultraviolet spectrum. InGaN/GaN quantum wells serve as critical components in LEDs for solid-state lighting, visible display technology and high-efficiency lighting applications [36]. Researchers continue to explore and optimize these QW structures to meet the demands of various advanced technologies.

Nanowires are quasi-one-dimensional structures, often with diameters on the nanometer scale, which can lead to quantum confinement effects. Unlike bulk materials that have continuous energy bands, the quantum confinement in nanowires results in discrete energy levels. This discretization can be used to design novel devices based on quantum effects. Furthermore, nanowires have an extremely high surface area compared to their volume, which gives nanowires unique surface-related properties, such as enhanced chemical reactivity and sensitivity to the surrounding environment. It makes nanowires attractive for applications in sensors. Figure 1.4 shows a Scanning Electron Microscope (SEM) picture of an array of GaAs nanowires and Si nanowires.

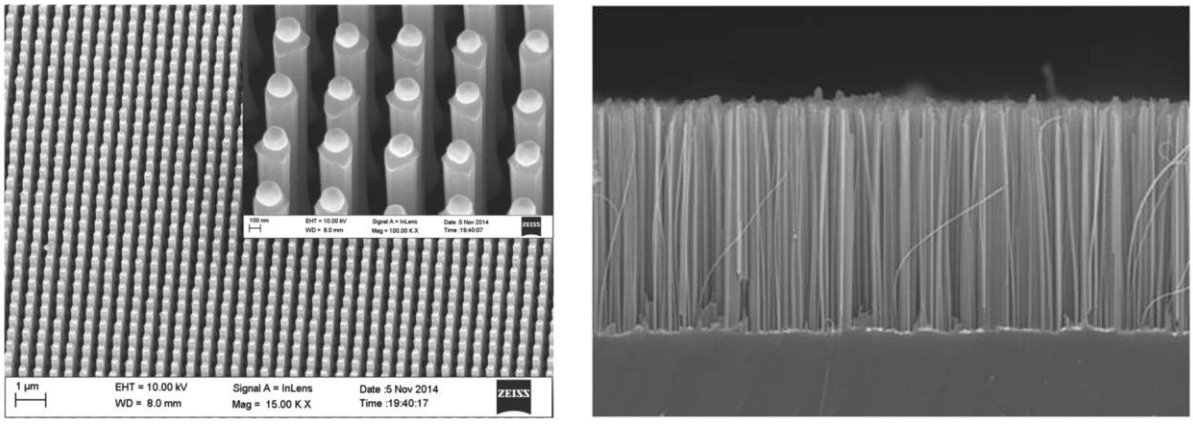

(a) (b)

Figure 1.4 (a) SEM of an array of GaAs nanowires [37]. (b) SEM of Si nanowires [38].

Like Nanowires, QDs exhibit quantum confinement effects, but in this case in three dimensions. This results in a highly localized confinement of charge carriers (electrons and holes) in which the size of the QD directly influences its electronic and optical properties and other factors become less significant. With QDs, we also see the emergence of further quantum phenomena such as quantum coherence, single photon emission and quantized spin effects. Figure 1.5 shows Transmission electron microscopy (TEM) Images of uncapped self-assembled InAs/GaAs quantum dots.

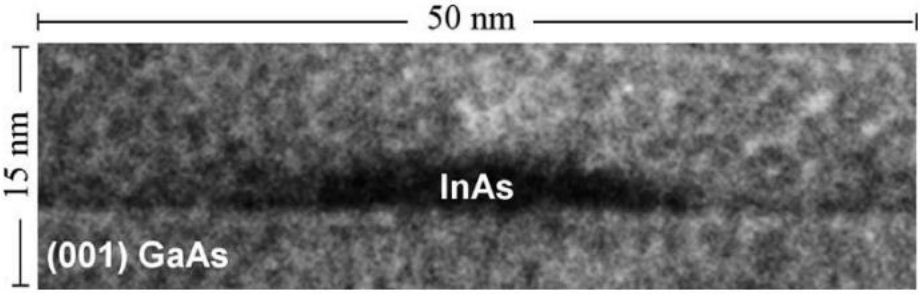

Figure 1.5 TEM of InAs/GaAs quantum dots [39]

The unique electronic and optical properties of QDs leads to diverse applications in various fields. In displays and lighting, colloidal QDs are utilized in Quantum Dot LED displays, offering a wider color gamut and improved accuracy compared to traditional displays. They also serve as energy-efficient light sources in semiconductor QD-based LEDs. In solar cells, quantum dots enhance efficiency through multiple exciton generation, increasing energy conversion from absorbed photons. As single-photon sources, quantum dots emit photons one at a time, playing a crucial role in quantum communication, quantum computing, and quantum cryptography [40-44].

A quantum ring (QR) is a type of nanoscale semiconductor structure with a ring-like geometry. Atomic force microscopy (AFM) pictures for AlGaAs/GaAs and InGaAs/GaAs QRs are shown in Figure 1.6. It is essentially a circular or annular semiconductor region that exhibits quantum confinement effects in the azimuthal direction (around the ring). QRs can be considered as a hybrid between QDs and QWs, as they possess properties of both structures due to their unique radial geometry. For the quantum confinement of a QR, electrons and holes are confined in the azimuthal direction, resulting in quantized energy levels, which are determined by the ring's size and shape. Their applications include quantum computing, information storage, sensors, communication, spintronics, optics, metrology, and energy harvesting. While these applications are still in the early stages, QRs show great potential for revolutionizing various fields of science and technology.

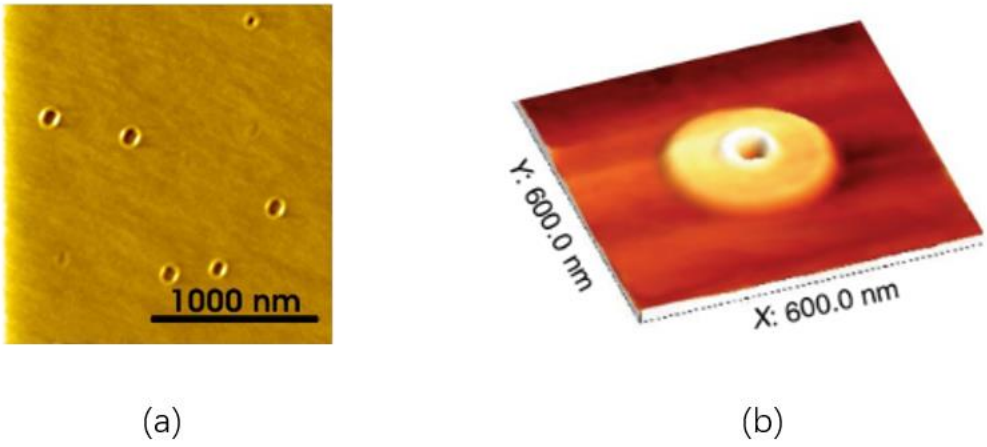

Figure 1.6 AFM of (a) AlGaAs/GaAs [45] and (b) InGaAs/GaAs [46] quantum rings

1.3 Photonic Crystals

Photonic Crystals (PhCs) are periodic structures that can manipulate the behavior of light in a manner analogous to how the transport of electrons is dependent on the periodic crystal structure in semiconductors. PhCs are engineered at the nanoscale, typically using dielectric or semiconductor materials, to form periodic lattices with alternating regions of high and low refractive index which interact with the wavelengths of light. This periodic arrangement creates bandgaps, where certain light wavelengths are blocked from propagating through the crystal, while other wavelengths can be allowed to pass through. PhCs can exhibit either complete or partial bandgaps, with the former fully prohibiting light across a specific frequency range, and the latter permitting some frequencies to pass. By engineering defects or disturbances in the periodic lattice, PhCs can guide and route light along desired paths, enabling compact and efficient photonic devices like waveguides and optical circuits.

There are three different dimensional types of PhCs shown in Figure 1.7. These different types of PhCs offer distinct optical properties and functionalities, making them valuable in various photonics and optoelectronics applications. The choice of dimension type depends on the specific requirements of the device or system and the desired control over light propagation and interaction with matter.

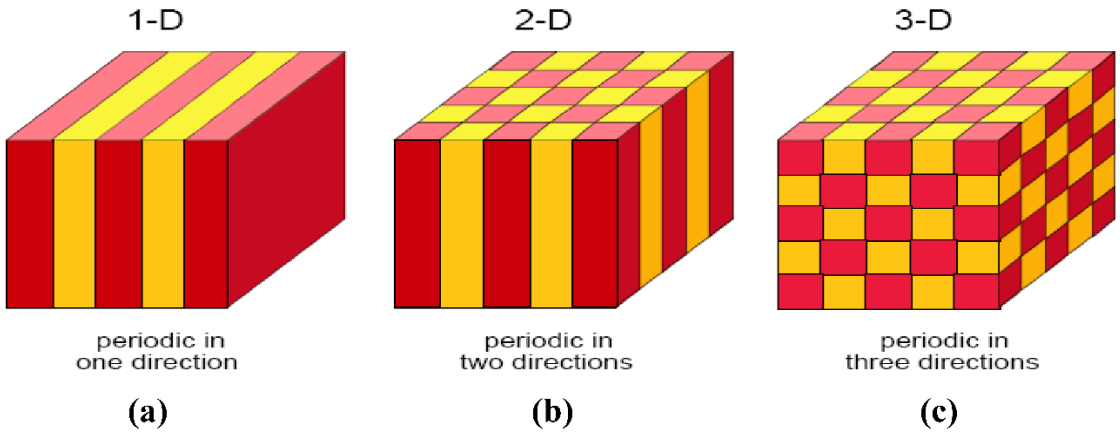

Figure 1.7 Different dimensional photonic crystals [47]

One-dimensional (1D) PhCs are periodic structures with a repeating pattern in only one spatial dimension. They are typically composed of alternating layers of materials with different refractive indices stacked along a single direction. The periodic arrangement of these layers creates a bandgap for certain wavelengths of light, allowing precise control over light propagation and optical properties. The periodicity of 1D PhCs leads to the constructive or destructive interference of light waves. This results in the formation of a bandgap, where certain frequencies of light are prohibited from propagating through the crystal, while others can pass through or be manipulated. 1D PhCs are commonly used as optical filters, as they can selectively transmit or reflect specific wavelengths of light. By engineering the layer thickness and refractive indices, these crystals can act as wavelength-selective mirrors or spectral filters [48-50]. The alternating layers of high and low refractive index in 1D PhCs create distributed Bragg reflectors (DBRs) and Distributed feedback lasers (DFBs), reflecting specific wavelengths with very high precision [50-52].

Two-dimensional (2D) PhCs consist of periodic structures exhibiting a repeating pattern in two spatial dimensions. Unlike 1D PhCs, which have periodicity in only one direction, 2D PhCs possess a periodic lattice in both the x and y directions. These structures are typically fabricated by creating a periodic array of holes or rods in a planar material, forming a 2D lattice. 2D PhCs can exhibit complete bandgaps, where certain ranges of frequencies are completely forbidden for light propagation in any direction within the crystal. This property allows precise control over light at different wavelengths. By engineering the lattice structure, 2D PhCs can guide and confine light along specific paths or particular guided modes. This

capability is crucial for creating integrated optical circuits and photonic devices. Such PhCs now play a significant role in the formation of optical cavities (ref: https://doi.org/10.1038/nature02063) in which a defect structure is introduced into the periodic array. The localized confinement which is produced can be used to enhance the emission of single photon emitters through an intense light-matter interaction. 2D PhCs are also now used in vertical-cavity surface-emitting lasers (VCSELs) [54].

Three-dimensional (3D) PhCs are periodic structures with a repeating pattern in all three spatial dimensions: x, y, and z. These crystals are more intricate to fabricate compared to lower-dimensional structures, yet they provide unparalleled and potent control over light propagation and optical properties. They can create complete bandgaps, completely forbidding certain ranges of frequencies for light propagation within the crystal, leading to total reflection or confinement of light within the crystal volume. 3D PhCs play a crucial role in developing high-quality lasers with low thresholds and narrow line widths, as the bandgap properties enable strong feedback and confinement of light, resulting in efficient laser emission [55]. These crystals find diverse applications in photonics, optoelectronics, and quantum technologies, offering advanced light control and manipulation capabilities. Although challenging to fabricate, continuous research and advancements in nanofabrication techniques expand the potential for practical implementation and discoveries in this field.

1.4 Semiconductor Nanostructures Fabrication

The history of semiconductor nanostructure fabrication methods is a story of continuous innovation and the development of increasingly sophisticated techniques. Present-day nanostructure fabrication involves a combination of top-down (e.g., lithography) and bottom-up (e.g., self-assembly) approaches to create intricate and functional nanostructures.

1.4.1 Epitaxial Growth Techniques

The historical progression of bottom-up approaches in semiconductor nanostructure fabrication centers on methods that construct nanostructures from individual atoms or molecules, encouraging them to autonomously self-assemble into desired configurations. These techniques leverage the principles of self-organization and molecular interactions to achieve the creation of intricate nanoscale structures.

Molecular beam epitaxy (MBE) was developed by J.R. Arthur and A.Y. Cho in the late 1960s and remains a widely used method for growing high-quality semiconductor films [56]. MBE operates under ultra-high vacuum conditions and allows extremely precise deposition of atoms or molecules onto a substrate, enabling precise control of layer thickness and composition. This technique plays a crucial role in the fabrication of nanostructures such as QWs, superlattices, and other semiconductor structures. Similarly, metal-organic chemical vapour deposition (MOCVD), developed in the 1970s, provides an epitaxial growth method for depositing thin films of semiconductor materials [57]. By decomposing metal-organic precursors in a heated reactor, MOCVD can produce high-quality films.

Both MBE and MOCVD are epitaxial growth techniques chosen for their respective strengths depending on the application's demands. MBE operates in an ultra-high vacuum (UHV) setting, ensuring minimized impurities and, consequently, delivering high-purity films. Its method supports layer-by-layer atomic growth, producing sharp interfaces ideal for quantum wells and superlattice constructs. The precision control over the effusion cell shutters in MBE ensures accurate atomic layer deposition. On the other hand, MOCVD boasts faster growth rates compared to MBE, aligning it more with commercial device production.

1.4.2 Lithography Techniques

Top-down approaches to semiconductor nanostructure fabrication refer to methods that start with a bulk material and then carve or shape it into the desired nanoscale structures. This contrasts with bottom-up approaches, where nanostructures are built atom-by-atom or molecule-by-molecule.

In the 1950s, photolithography was in its early stages for semiconductor applications [58]. The predominant method was contact printing, using visible light and rudimentary photoresists that required longer exposure times. Silicon Valley's rise during this decade and the invention of the integrated circuit in 1958 by Jack Kilby highlighted photolithography's importance. The 1970s saw the commercialization of proximity and projection mask aligners, enabling high-resolution patterning on semiconductor wafers [58]. These aligners played a crucial role in microelectronics, paving the way for further miniaturization. the 1980s was a decade of rapid advancements in photolithography, marked by the move to deep-UV wavelengths, refined equipment, improved photoresists, and heightened automation, all aiming to address the industry's push for smaller, more efficient semiconductor devices [59]. In addition, Electron beam lithography (EBL) is a specialized method for creating extremely fine patterns [63]. Unlike photolithography, EBL works by scanning a focused electron beam across a surface covered with an electron-sensitive film (resist). The electrons cause chemical changes in the resist, which can then be developed to reveal a pattern. Nanoimprint lithography (NIL) emerged in the 1990s [64] as a nanoscale patterning technique that uses a physical mold to "stamp" a desired pattern onto a substrate coated with a special resist. Instead of light or electrons, NIL relies on the direct physical deformation of the resist. Dip-Pen Nanolithography (DPN) is a nanoscale writing technique that uses an AFM tip coated with molecular "ink" to transfer molecules to a substrate. This method, inspired by traditional quill writing, can achieve resolutions of tens of nanometers [66][67]. This approach provided greater flexibility for prototyping and research.

The mentioned examples represent only a fraction of the diverse fabrication methods employed for creating semiconductor nanostructures. As nanotechnology progresses, researchers are actively exploring novel techniques and approaches to expand the horizons of semiconductor nanostructure fabrication and unlock even more possibilities in this field.

1.5 Motivation and Objective

The development of surface nanostructures has been widely explored to enhance the external energy conversion efficiency of various semiconductor photonic devices, such as solar cells, LEDs, and LDs [68-71]. Si and GaAs are significant materials used in these semiconductor optoelectronic devices. Unlike Si, GaAs is characterized by a direct bandgap, higher breakdown voltage, superior thermal stability, and significant resistance to radiation, ensuring its remarkable durability under demanding operational conditions [72-75]. However, both Si and GaAs, along with other semiconductors, suffer from high surface reflectivity as a consequence of a high refractive index, which diminishes the external efficiency of these devices. Specifically, GaAs has a reflectivity over 39% within the visible spectrum and silicon is not much lower. For GaAs-based solar cells, the power conversion efficiency is limited to around 17.57% [76], and for GaAs LEDs, the external quantum efficiency is restricted to about 3% [77] with surface reflectivity being a significant factor in these low values.

To solve this problem, the PhC structure introduced in this study aims to improve light extraction efficiency in light-emitting devices and enhance light absorption in photovoltaic systems. Various techniques have been developed for synthesizing PhC structures, including electron beam lithography (EBL) [78], [79] and nanoimprint lithography (NIL) [80-82]. Despite their effectiveness, these techniques are often associated with high patterning costs, which would not be compatible with mass-market devices. In contrast, Laser Interference Lithography (LIL) is celebrated for its simplicity, cost-effectiveness, and the ability to rapidly produce patterns over large areas, making it well-suited for industrial production [83-85].

Currently, the fabrication of PhC nanostructures using single-pulse LIL, particularly for GaAs and GaAs-based devices, has not been extensively reported, indicating a significant opportunity for innovative research. Investigating single-pulse LIL as a method for creating PhCs could herald substantial progress in photonic device technology. Single-pulse LIL is often preferred because it provides higher peak energy, better control over thermal effects, and avoids the complexities and potential inaccuracies associated with synchronizing multiple pulses. Ensuring that two pulses arrive at exactly the same spatial and temporal location to

create an interference pattern can be challenging. Any misalignment or timing error could result in a less accurate or blurred pattern. A single pulse inherently avoids these synchronization issues, ensuring the interference pattern is formed as intended. This leads to more precise, consistent, and reliable patterning outcomes.

This approach also allows for the creation of pre-patterns on structures during epitaxial growth, facilitating the precise array of QDs and QRs, thereby opening new avenues for enhancing device performance.

1.6 Outline

This thesis consists of 7 chapters:

Chapter 1 presents a comprehensive overview of the evolution of Group III-V semiconductors, tracing the historical development of semiconductor nanostructures and delineating the various fabrication methods employed in their integration into devices. Additionally, the chapter addresses the challenges and motivations driving this project.

Chapter 2 provides an in-depth background of physical and electrical properties that characterize semiconductors, offering a detailed background essential for understanding their behavior and application in various technologies. Additionally, this chapter elaborates on the conceptual and practical aspects of Photonic Crystal structures, including their theoretical underpinnings, design principles, and the role they play in manipulating photonic behavior. The method and technology of Laser Interference Lithography as a pivotal fabrication technique for creating intricate Photonic Crystal patterns are also thoroughly explored.

Chapter 3 provides an overview of the device fabrication processes used within the study, along with measurement equipment for characterization, electrical, and optical assessments.

Chapter 4 details our successful fabrication of Photonic Crystal structures on GaAs substrates employing the single pulse Laser Interference Lithography technique. The topographical features of these PhC structures were verified to match our design expectations, as

substantiated by Scanning Electron Microscopy and Atomic Force Microscopy observations. Furthermore, FDTD simulations were conducted to analyse the photonic bandgap properties inherent to the fabricated structures. The results suggest that these Photonic Crystal structures are promising candidates for integration into GaAs-based optoelectronic devices, offering the potential to enhance device performance across specific wavelength ranges. Experimental findings have demonstrated a significant reduction in the average reflectance of GaAs substrates equipped with Photonic Crystal structures, dropping to below 5% across a broad spectral range from 450 nm to 700 nm. Therefore, the Photonic Crystal structures engineered in this study stand to significantly boost light extraction efficiency in emitting devices and improve light absorption in photovoltaic applications.

Chapter 5 details the fabrication and assembly of photonic crystal structures on LED substrates through the application of nanosecond pulsed laser interference lithography, with subsequent pattern transfer accomplished via ICP etching. The quality of the photonic crystal structures on the LED sample was verified through SEM analysis, showing the effectiveness of a three-beam single pulse LIL technique combined with meticulously controlled ICP etching for depth adjustment. FDTD simulations were conducted to assess the photonic bandgap properties and enhancements in light extraction efficiency. Finally, electroluminescence measurements were performed on LEDs incorporating various photonic crystal depths to analyze their performance.

Chapter 6 describes the successful attainment of accurately arranged GaAs Quantum Rings using the Direct Laser Interference Patterning method within the MBE growth procedure. AFM analyses were performed to verify the structural coherence and orderly arrangement of the QRs. Furthermore, PL spectroscopy was applied to assess the optical characteristics of the QRs.

Chapter 7 provides a summary of the research findings detailed in this thesis and offers perspectives on potential future directions.

Reference

[1] A. I. Blum, N. P. Mokrovski, and A. R. Regel, "Seventh All-Union Conference on the Properties of Semiconductors (Kiev, USSR, 1950)," Izv. Akad. Nauk SSSR Ser. Fiz, vol. 16, pp. 139, 1952.

[2] H. Welker, “Über neue halbleitende Verbindungen,” Zeitschrift für Naturforschung A, vol. 7, no. 11, pp. 744-749, 1952.

[3] D. N. Nasledov, A. A. Rogachev, S. M. Ryvkin, and B. V. Tsarenkov, “Recombination radiation of gallium arsenide,” Sov. Phys. Solid State, vol. 4, pp. 782-784, 1962.

[4] M. P. Mikhailova, K. D. Moiseev, and Y. P. Yakovlev, “Discovery of III–V semiconductors: physical properties and application,” Semiconductors, vol. 53, pp. 273-290, 2019.

[5] D. Nirmal and J. Ajayan, Eds., Handbook for III-V high electron mobility transistor technologies. CRC Press, 2019.

[6] T. Mimura, “The early history of the high electron mobility transistor (HEMT),” IEEE Transactions on microwave theory and techniques, vol. 50, no. 3, pp. 780-782, 2002.

[7] T. Mimura, “Development of high electron mobility transistor,” Japanese Journal of Applied Physics, vol. 44, no. 12R, pp. 8263, 2005.

[8] R. Munusami and S. Prabhakar, "Group III–V Semiconductor High Electron Mobility Transistor on Si Substrate," Differ. Types Field-Effect Transistors-Theory Appl., 2017.

[9] A. Nathan, S. K. Saha, and R. M. Todi, Eds., "75th Anniversary of the Transistor," John Wiley & Sons, 2023.

[10] J. M. Liu, "Photonic devices," Cambridge University Press, 2009.

[11] E. F. Schubert, "Light-Emitting Diodes (2018)," E. Fred Schubert, 2018.

[12] I. Vurgaftman, M. P. Lumb, and J. R. Meyer, "Bands and Photons in III-V Semiconductor Quantum Structures," Oxford University Press, 2020.

[13] G. S. Agarwal, "Quantum optics," Cambridge University Press, 2012.

[14] A. M. Fox, "Quantum optics: an introduction," Oxford University Press, USA, 2006.

[15] D. Awschalom, D. Loss, and N. Samarth, "Semiconductor spintronics and quantum computation," Springer Science & Business Media, 2002.

[16] W. Zhang, S. Han, X. J. Ma, Y. Sun, and J. L. Xiao, "The Properties of the Polaron in III-V Compound Semiconductor Quantum Dots Induced by the Influence of Rashba Spin-Orbit Interaction," International Journal of Theoretical Physics, vol. 61, no. 5, pp. 131, 2022.

[17] C. Convertino et al., "A hybrid III–V tunnel FET and MOSFET technology platform integrated on silicon," Nat. Electron., vol. 4, no. February, 2021, doi: 10.1038/s41928-020-00531-3.

[18] C. Navarro et al., "Capacitor-less dynamic random access memory based on a III–V transistor with a gate length of 14 nm," Nat. Electron., 2019, doi: 10.1038/s41928-019-0282-6.

[19] K. Hennessy et al., "Quantum nature of a strongly coupled single quantum dot-cavity system," Nature, 2007, doi: 10.1038/nature05586.

[20] P. Zoller et al., "Quantum information processing and communication," Eur. Phys. J. D, 2005, doi: 10.1140/epjd/e2005-00251-1.

[21] M. Kroutvar et al., "Optically programmable electron spin memory using semiconductor quantum dots," Nature, 2004, doi: 10.1038/nature03008.

[22] Y. U. Peter and M. Cardona, "Fundamentals of semiconductors: physics and materials properties," Springer Science & Business Media, 2010.

[23] H. R. Huff, "John Bardeen and transistor physics," in AIP Conference Proceedings, vol. 550, no. 1, American Institute of Physics, 2001, pp. 3-32.

[24] B. K. Tanner, "Introduction to the Physics of Electrons in Solids," p. 264, 1995.

[25] R. H. Bube, "Electrons in solids: an introductory survey," Academic Press, 1992.

[26] D. Bimberg, Ed., "Semiconductor nanostructures," Springer Science & Business Media, 2008.

[27] M. Kneissl, A. Knorr, S. Reitzenstein, and A. Hoffmann, Eds., "Semiconductor nanophotonics: materials, models, and devices," vol. 194, Springer, 2020.

[28] T. Ihn, "Semiconductor Nanostructures: Quantum states and electronic transport," OUP Oxford, 2009.

[29] T. Edvinsson, "Optical quantum confinement and photocatalytic properties in two-, one- and zero-dimensional nanostructures," Royal Society Open Science, vol. 5, no. 9, p. 180387, 2018.

[30] R. D. Dupuis, "III–V semiconductor quantum-well devices grown by metalorganic chemical vapor deposition," Proceedings of the IEEE, vol. 101, no. 10, pp. 2188-2199, 2013.

[31] A. Zisowsky, A. Arnold, M. Ehrhardt, and T. Koprucki, "Transient Simulation of k · p-Schrödinger Systems Using Discrete Transparent Boundary Conditions," in Multi-Band Effective Mass Approximations: Advanced Mathematical Models and Numerical Techniques, Springer International Publishing, 2014, pp. 247-272.

[32] A. V. Malevskaya et al., "Infrared (850 nm) light-emitting diodes with multiple InGaAs quantum wells and 'back' reflector," Semiconductors, vol. 55, no. 8, pp. 686-690, 2021.

[33] A. G. U. Perera et al., "GaAs/InGaAs quantum well infrared photodetector with a cutoff wavelength at 35 μm," Applied Physics Letters, vol. 77, no. 5, pp. 741-743, 2000.

[34] A. Stöhr et al., "InGaAs/GaAs multiple-quantum-well modulators and switches," Optical and Quantum Electronics, vol. 25, pp. S865-S883, 1993.

[35] F. J. Towner, "Room temperature red light photoluminescence from AlGaAs multiple quantum well structures at very low excitation intensities," Journal of Vacuum Science & Technology B: Microelectronics and Nanometer Structures Processing, Measurement, and Phenomena, vol. 14, no. 3, pp. 2315-2317, 1996.

[36] K. C. Kim et al., "Improved electroluminescence on nonpolar m-plane InGaN/GaN quantum wells LEDs," physica status solidi (RRL)–Rapid Research Letters, vol. 1, no. 3, pp. 125-127, 2007.

[37] I. Åberg et al., "A GaAs nanowire array solar cell with 15.3% efficiency at 1 sun," IEEE Journal of Photovoltaics, vol. 6, no. 1, pp. 185-190, 2015.

[38] Z. Guo et al., "Optical properties of silicon nanowires array fabricated by metal-assisted electroless etching," in Next Generation (Nano) Photonic and Cell Technologies for Solar Energy Conversion, vol. 7772, SPIE, 2010, pp. 181-187.

[39] P. Boucaud and S. Sauvage, "Infrared photodetection with semiconductor self-assembled quantum dots," Comptes Rendus Physique, vol. 4, no. 10, pp. 1133-1154, 2003.

[40] R. J. Warburton, "Single spins in self-assembled quantum dots," Nature Materials, 2013, doi: 10.1038/nmat3585.

[41] M. Davanco et al., "Heterogeneous integration for on-chip quantum photonic circuits with single quantum dot devices," Nat. Commun., 2017, doi: 10.1038/s41467-017-00987-6.

[42] P. Senellart, G. Solomon, and A. White, "High-performance semiconductor quantum-dot single-photon sources," Nat. Nanotechnol., vol. 12, no. 11, pp. 1026–1039, 2017, doi: 10.1038/nnano.2017.218.

[43] E. Knill, R. Laflamme, and G. J. Milburn, "A scheme for efficient quantum computation with linear optics," Nature, 2001, doi: 10.1038/35051009.

[44] A. Beveratos et al., "Single Photon Quantum Cryptography," Phys. Rev. Lett., 2002, doi: 10.1103/PhysRevLett.89.187901.

[45] N. Pankaow, S. Thainoi, S. G. Matsik, H. C. Liu, M. Gao, W. J. Schaff, and W. Yeo, "Surface morphology and photoluminescence of InGaAs quantum rings grown by droplet epitaxy with varying In0. 5Ga0. 5 droplet amount," Journal of Crystal Growth, vol. 323, pp. 282-285, 2011.

[46] M. Gurioli, Z. Wang, A. Rastelli, T. Kuroda, and S. Sanguinetti, "Droplet epitaxy of semiconductor nanostructures for quantum photonic devices," Nature materials, vol. 18, no. 8, pp. 799-810, 2019.

[47] S. Robinson and R. Nakkeeran, "Photonic crystal ring resonator based optical filters," Advances in Photonic Crystals, vol. 1, pp. 1-26, 2013.

[48] Z. A. Alrowaili et al., "One-dimensional photonic crystal structure comprising a hyperbolic metamaterial for optical filtering purpose," Optical and Quantum Electronics, vol. 55, no. 1, p. 31, 2023.

[49] B. Mamri and O. Barkat, "Design of a selective filter based on one-dimensional superconductor photonic crystal," Journal of Superconductivity and Novel Magnetism, vol. 32, no. 11, pp. 3397-3405, 2019.

[50] L. Han, "1D photonic crystals: principles and applications in silicon photonics," Theor. Found. Appl. Photonic Cryst, pp. 159-180, 2018.

[51] S. O. Abdellatif and G. A. Alsayed, "Optimizing 1D photonic crystal structures for thin film solar cells," in 2019 IEEE Conference on Power Electronics and Renewable Energy (CPERE), IEEE, 2019, pp. 333-337.

[52] G. M. Paternò, G. Manfredi, F. Scotognella, and G. Lanzani, "Distributed Bragg reflectors for the colorimetric detection of bacterial contaminants and pollutants for food quality control," APL Photonics, vol. 5, no. 8, 2020.

[53] D. Benelarbi, T. Bouchemat, and M. Bouchemat, "Study of photonic crystal microcavities coupled with waveguide for biosensing applications," Optical and Quantum Electronics, vol. 49, pp. 1-16, 2017.

[54] T. C. Lu et al., "GaN-based two-dimensional surface-emitting photonic crystal lasers with AlN/ GaN distributed Bragg reflector," Applied Physics Letters, vol. 92, no. 1, 2008.

[55] S. Iwamoto, M. Nomura, A. Tandaechanurat, D. Cao, and Y. Arakwa, "2D and 3D photonic crystal nanocavity lasers with quantum dot gain," in IEEE Photonics Conference 2012, IEEE, 2012, pp. 866-867.

[56] A. Y. Cho and J. R. Arthur, "Molecular beam epitaxy," Prog. Solid State Chem., vol. 10, pp. 157-191, 1975.

[57] A. G. Thompson, "MOCVD technology for semiconductors," Mater. Lett., vol. 30, no. 4, pp. 255-263, 1997.

[58] V. K. Khanna, "Integrated nanoelectronics," NanoSci. Technol, vol. 10, pp. 978-81, 2016.

[59] B. J. Lin, "Deep UV lithography," Journal of Vacuum Science and Technology, vol. 12, no. 6, pp. 1317-1320, 1975.

[63] C. Vieu et al., "Electron beam lithography: resolution limits and applications," Appl. Surf. Sci., vol. 164, no. 1–4, pp. 111–117, 2000.

[64] S. Y. Chou, P. R. Krauss, and P. J. Renstrom, "Nanoimprint lithography," J. Vac. Sci. Technol. B Microelectron. Nanom. Struct. Process. Meas. Phenom., vol. 14, no. 6, pp. 4129–4133, 1996.

[65] W. L. Brown, T. Venkatesan, and A. Wagner, "Ion beam lithography," Nucl. Instruments Methods Phys. Res., vol. 191, no. 1–3, pp. 157–168, 1981.

[66] F. J. Towner, "Room temperature red light photoluminescence from AlGaAs multiple quantum well structures at very low excitation intensities," Journal of Vacuum Science & Technology B: Microelectronics and Nanometer Structures Processing, Measurement, and Phenomena, vol. 14, no. 3, pp. 2315-2317, 1996.

[67] K. C. Kim et al., "Improved electroluminescence on nonpolar m-plane InGaN/GaN quantum wells LEDs," physica status solidi (RRL)–Rapid Research Letters, vol. 1, no. 3, pp. 125-127, 2007.

[68] C. Ducros, A. Brodu, G. Lorin, F. Emieux, and A. Pereira, “Optical performances of antireflective moth-eye structures. Comparison with standard vacuum antireflection coatings for application to outdoor lighting LEDs,” *Surf Coat Technol*, vol. 379, Dec. 2019, doi: 10.1016/j.surfcoat.2019.125044.

[69] G. Tan *et al.*, “Broadband antireflection film with moth-eye-like structure for flexible display applications,” *Optica*, vol. 4, no. 7, p. 678, Jul. 2017, doi: 10.1364/optica.4.000678.

[70] S. Almenabawy, Y. Zhang, A. Flood, R. Prinja, and N. P. Kherani, “Nanometer-Mesa Inverted-Pyramid Photonic Crystals for Thin Silicon Solar Cells,” *ACS Appl Energy Mater*, vol. 5, no. 11, pp. 13808–13816, Nov. 2022, doi: 10.1021/acsaem.2c02437.

[71] D. Przybylski and S. Patela, “Modelling of a two-dimensional photonic crystal as an antireflection coating for optoelectronic applications,” *Opto-Electronics Review*, vol. 27, no. 1, pp. 79–89, Mar. 2019, doi: 10.1016/j.opelre.2019.02.004.

[72] A. Sharma and T. D. Das, “Electronic band structure and optical properties of GaAsSb/GaAs for optoelectronic device applications: A 14 band k.p study,” *Opt Mater (Amst)*, vol. 112, Feb. 2021, doi: 10.1016/j.optmat.2020.110734.

[73] T. Lin, J. nan Xie, S. huan Ning, Q. min Li, and B. Li, “Study on the p-type ohmic contact in GaAs-based laser diode,” *Mater Sci Semicond Process*, vol. 124, Mar. 2021, doi: 10.1016/j.mssp.2020.105622.

[74] S. Sederberg, F. Kong, F. Hufnagel, C. Zhang, E. Karimi, and P. B. Corkum, “Vectorized optoelectronic control and metrology in a semiconductor,” *Nat Photonics*, vol. 14, no. 11, pp. 680–685, Nov. 2020, doi: 10.1038/s41566-020-0690-1.

[75] T. Zaengle *et al.*, “A Novel Route to Fibers with Incongruent and Volatile Crystalline Semiconductor Cores: GaAs,” *ACS Photonics*, vol. 9, no. 3, pp. 1058–1064, Mar. 2022, doi: 10.1021/acsphotonics.2c00008.

[76] D. Parajuli, G. S. Gaudel, D. Kc, K. B. Khattri, and W. Y. Rho, “Simulation study of TiO2 single layer anti-reflection coating for GaAs solar cell,” *AIP Adv*, vol. 13, no. 8, Aug. 2023, doi: 10.1063/5.0153197.

[77] T. C. Lin *et al.*, “Large-Signal Modulation Performance of Light-Emitting Diodes with Photonic Crystals for Visible Light Communication,” *IEEE Trans Electron Devices*, vol. 65, no. 10, pp. 4375–4380, Oct. 2018, doi: 10.1109/TED.2018.2864346.

[78] S. P. Yu, D. C. Cole, H. Jung, G. T. Moille, K. Srinivasan, and S. B. Papp, “Spontaneous pulse formation in edgeless photonic crystal resonators,” *Nat Photonics*, vol. 15, no. 6, pp. 461–467, Jun. 2021, doi: 10.1038/s41566-021-00800-3.

[79] J. Li, J. Yan, L. Jiang, J. Yu, H. Guo, and L. Qu, “Nanoscale multi-beam lithography of photonic crystals with ultrafast laser,” *Light Sci Appl*, vol. 12, no. 1, Dec. 2023, doi: 10.1038/s41377-023-01178-3.

[80] K. J. Byeon, S. Y. Hwang, and H. Lee, “Fabrication of two-dimensional photonic crystal patterns on GaN-based light-emitting diodes using thermally curable monomer-based nanoimprint lithography,” *Appl Phys Lett*, vol. 91, no. 9, 2007, doi: 10.1063/1.2776980.

[81] M. Torras, P. Molet, L. Soler, J. Llorca, A. Roig, and A. Mihi, “Au/TiO2 2D-Photonic Crystals as UV–Visible Photocatalysts for H2 Production,” *Adv Energy Mater*, vol. 12, no. 6, Feb. 2022, doi: 10.1002/aenm.202103733.

[82] H. Zhao, X. Cao, Q. Dong, C. Song, L. Wang, and L. Gao, “Large-area silicon photonic crystal supporting bound states in the continuum and optical sensing formed by nanoimprint lithography,” *Nanoscale Adv*, vol. 5, no. 5, pp. 1291–1298, Jan. 2023, doi: 10.1039/d3na00001j.

[83] Y. R. Wang, I. S. Han, C. Y. Jin, and M. Hopkinson, “Precise Arrays of Epitaxial Quantum Dots Nucleated by in Situ Laser Interference for Quantum Information Technology Applications,” *ACS Appl Nano Mater*, vol. 3, no. 5, pp. 4739–4746, May 2020, doi: 10.1021/acsanm.0c00738.

[84] N. Pérez, T. Tavera, A. Rodríguez, M. Ellman, I. Ayerdi, and S. M. Olaizola, “Fabrication of sub-micrometric metallic hollow-core structures by laser interference lithography,” in *Applied Surface Science*, Elsevier B.V., Sep. 2012, pp. 9370–9373. doi: 10.1016/j.apsusc.2012.03.185.

[85] M. Ellman *et al.*, “High-power laser interference lithography process on photoresist: Effect of laser fluence and polarisation,” *Appl Surf Sci*, vol. 255, no. 10, pp. 5537–5541, Mar. 2009, doi: 10.1016/j.apsusc.2008.07.201.

Chapter 2

Background

2.1 Semiconductors

Solids can be classified based on their electronic bandgap (Eg), which is the energy range between the valence band (VB) and the conduction band (CB) in their electronic band structure [1]. The bandgap determines a material's electrical conductivity and optical properties. Figure 2.1 shows the main classifications of solids based on their bandgap.

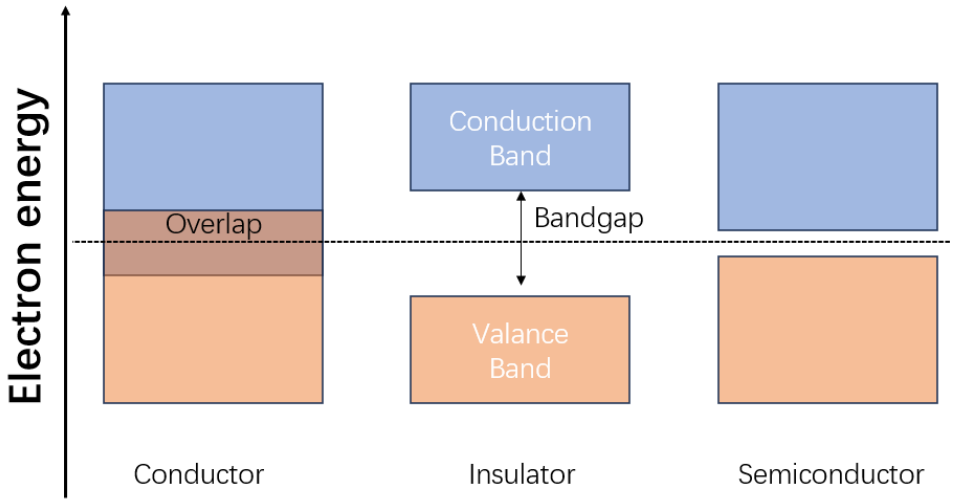

Figure 2.1 Schematic illustration of band-structure of conductor, semiconductor, and insulator

Conductors have a very small or nearly zero bandgap, meaning that their valence and conduction bands overlap. In conductors, electrons can easily move between the bands,

leading to high electrical conductivity. Metals are the most common examples of conductors, with materials like gold, aluminum, and silver being excellent conductors of electricity. Insulators have a relatively large bandgap, and as a result, very few electrons can be excited to the conduction band at room temperature or with low energy input. Insulators have high electrical resistance and do not conduct electricity.

Semiconductors occupy a special position between conductors and insulators due to their distinct electronic band structure, featuring a bandgap—an energy range separating the valence band from the conduction band.

Conductivity characterizes a material's capacity to conduct electrical charge. The conductivity of a material is defined as:

$$\sigma = ne\mu_n + ne\mu_p \tag{2.1}$$

In the provided equation 2.1, e represents the electronic charge (1.6 x 10^{-19} C), and μ_n and μ_p denote the electron and hole mobility, respectively. n and p represent the concentrations of electrons and holes, respectively. Conductors possess a high conductivity on the order of 10^7 $(\Omega \cdot m)^{-1}$. However, insulators display minimal conductivity on the order of 10^{-10} to 10^{-20} $(\Omega \cdot m)^{-1}$. Additionally, Semiconductors exhibit conductivities that lie between those of metals and insulators [2].

Semiconductors are special in that they can change their conductivity when subjected to external influences including temperature, light, and electric fields. At low temperatures or without additional energy input, semiconductors behave more like insulators, with most electrons confined to the valence band. However, with the application of energy, some electrons can be excited to the conduction band, resulting in partial electrical conductivity.

One way to control the conductivity of semiconductors is doping [3]. Semiconductor doping is a deliberate process in which impurity atoms, known as dopants, are intentionally introduced into a semiconductor material to modify its electrical properties. This controlled introduction of dopants alters the number of free charge carriers (electrons or holes) in the semiconductor, thereby affecting its conductivity and other electronic characteristics.

Dopants can be either donors or acceptors, depending on whether they contribute extra electrons or create holes in the crystal lattice of the semiconductor. Donor dopants, like

phosphorus or arsenic in silicon, provide extra electrons that become mobile charge carriers, increasing the material's electron concentration, and enhancing its conductivity. These types of semiconductors are known as n-type (negative-type) because of the excess of negatively charged electrons.

On the other hand, acceptor dopants, such as boron or gallium in silicon, create holes in the semiconductor crystal structure by accepting electrons from neighboring atoms. This results in an excess of positively charged carriers, making the material p-type (positive-type).

2.1.1 Direct and Indirect Band Structure

Semiconductors can have either direct or indirect band structures [4], which refers to the nature of electron transitions between the valence band and the conduction band in the semiconductor's energy band diagram shown in Figure 2.2.

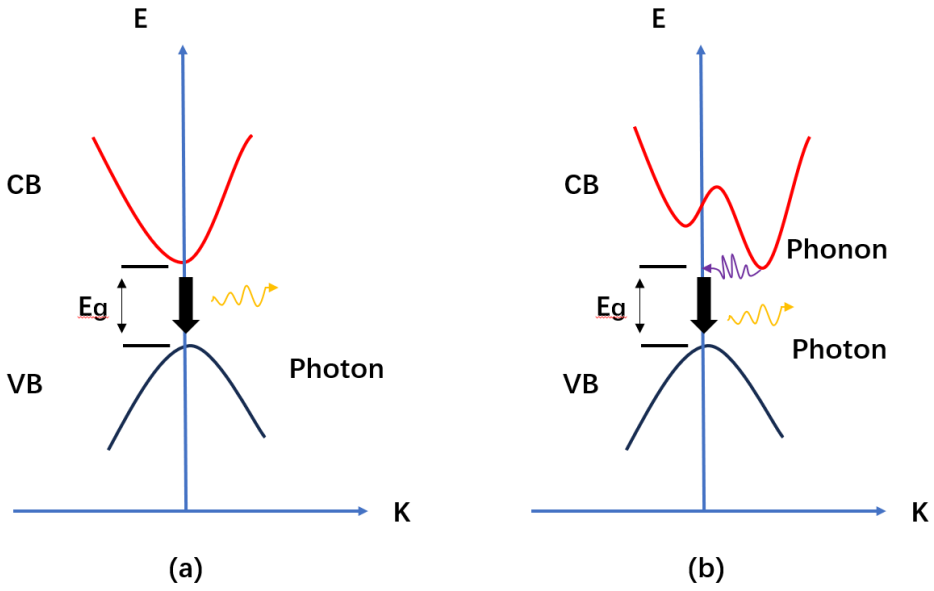

Figure 2.2 Schematics of (a) direct and (b) indirect band-structure

In direct band gap semiconductors, the energy minimum of the conduction band aligns directly with the energy maximum of the valence band in momentum space. This means that the momentum of the electron remains approximately the same during the transition from the valence band to the conduction band, emitting a photon which has a very small momentum. As a result, direct band gap semiconductors are efficient in absorbing and emitting photons with energies corresponding to the bandgap. This property makes them ideal for optoelectronic applications, such as LEDs and LDs, where direct transitions between the energy bands are crucial for efficient emission and absorption of light.

In contrast, indirect band gap semiconductors present a different scenario. Here, the energy minimum of the conduction band does not align with the energy maximum of the valence band in momentum space. As a result, electron transitions between the valence band and the conduction band involve a change in momentum, which requires the participation of another particle with significant momentum, principally a phonon (lattice vibration), to conserve momentum. This extra step involving phonon participation makes the transitions less probable and less efficient for photon emission and absorption compared to direct band gap semiconductors.

2.1.2 Absorption

Absorption occurs when photons with energies equal to or higher than the bandgap energy interact with the semiconductor material, they can be absorbed by the electrons in the valence band [5]. This absorption provides the electrons with sufficient energy to jump across the bandgap into the conduction band, creating electron-hole pairs. The absorbed energy from the photons is converted into excitation energy for the electrons and holes. The efficiency of bandgap absorption depends on the semiconductor's bandgap energy and the energy of the incident photons.

2.1.3 Luminescence

Opposite to absorption, luminescence refers to the emission of light when these materials undergo specific processes following excitation. When semiconductors are exposed to photons or an electric field, electrons can be excited from the valence band to the conduction band, creating electron-hole pairs. These excited electrons may subsequently recombine with the holes, releasing excess energy as photons (radiative transition) or by phonons (non-radiative transition)

Photoluminescence (PL) is the process where a material absorbs light and then re-emits it. This occurs in a series of steps: excitation, where the material absorbs light; relaxation, where the excited electron loses some energy; and emission, where the electron returns to its original state, emitting a photon [6,7]. The emitted light often has a longer wavelength than the absorbed light due to energy loss. Photoluminescence spectroscopy is a technique to study materials' luminescent properties and provides insights into their electronic structure and defects.

Electroluminescence (EL) in semiconductors occurs through electron-hole recombination, where excited electrons move to higher energy levels in the conduction band, creating electron-hole pairs [8,9]. Excess energy is released as photons, with energies corresponding to the semiconductor's bandgap.

2.1.4 Recombination

Radiative recombination

Figure 2.3 provides a schematic representation of several significant Radiative recombination mechanisms in semiconductors.

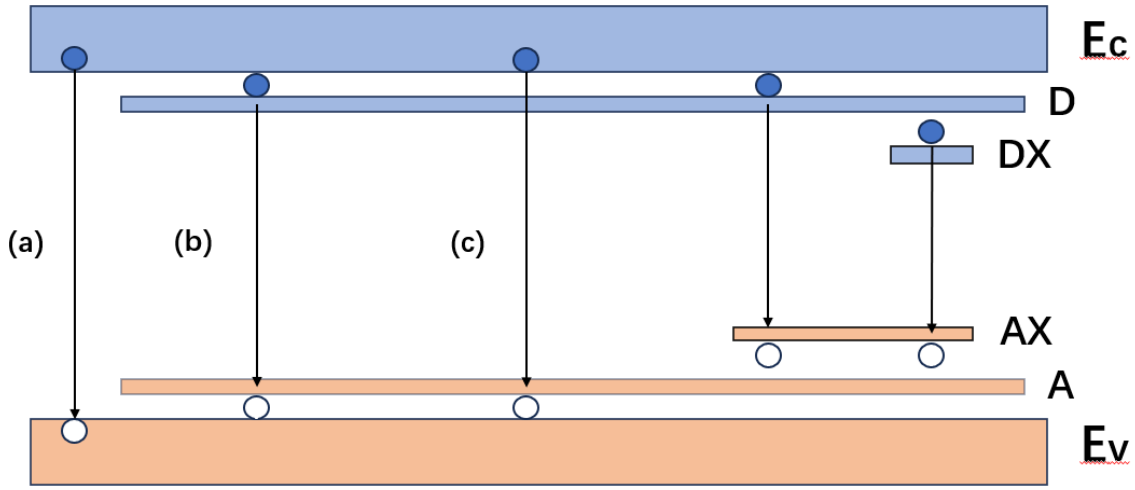

Figure 2.3 (a) band-to-band recombination (b) DAP recombination (c) exciton recombination.

(a) Band-to-band recombination [10]

During the recombination process in semiconductor materials, the photon energy of emission is equal to the bandgap energy (E_g) of the material.

(b) Donor-Acceptor pair (DAP) recombination [11]

Donor-acceptor recombination occurs in semiconductors that have been doped with impurities. It involves the recombination of a free electron (donor) with a hole bound to an impurity atom (acceptor). D and A is the energy level for donors and acceptors respectively. This process can lead to light emission or energy transfer, depending on the material and the specific impurity level.

(c) Excitonic recombination [12,13]

Excitonic recombination involves the recombination of an electron with a hole, forming an exciton (X), which is a bound electron-hole pair with lower energy than the unbound carriers. DX and AX is the energy level for donor-bound exciton and acceptor-bound exciton respectively. This process often occurs in materials with strong electron-hole interactions, such as quantum wells, quantum dots, and certain organic semiconductors.

Non-radiative recombination

Figure 2.4 provides a schematic representation of two non-radiative recombination mechanisms in semiconductors.

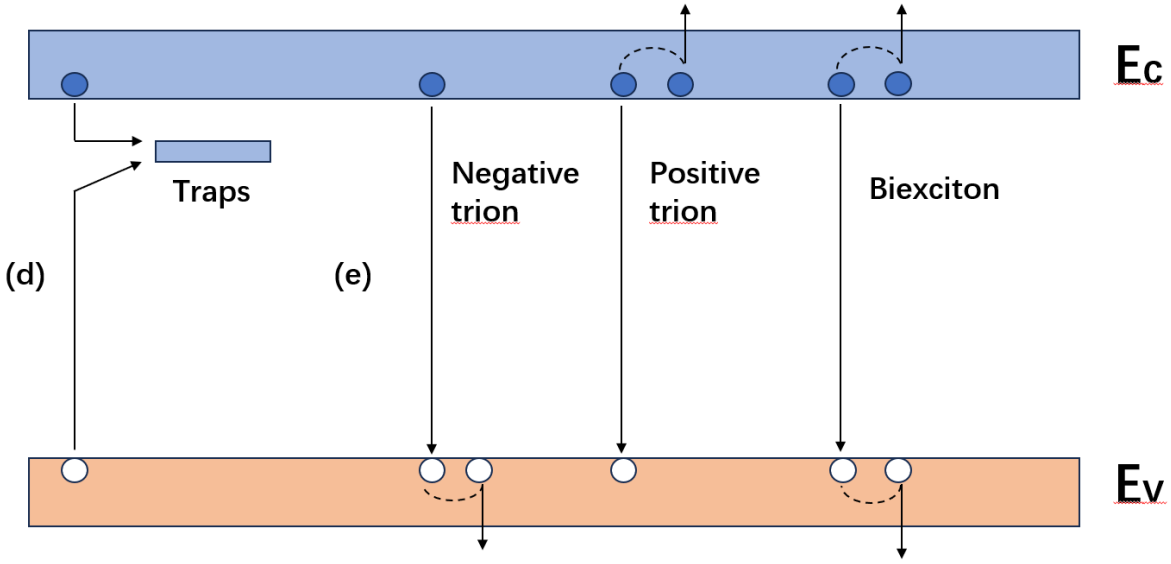

Figure 2.4 (d) Shockley-Read-Hall recombination (e) Auger recombination.

(d) Trap-assisted (Shockley-Read-Hall) recombination [14,15]

Trap-assisted recombination, also known as Shockley-Read-Hall recombination, is a non-radiative carrier recombination process that occurs in semiconductors with defects or impurities. In this mechanism, a free carrier (electron or hole) encounters a trap state, which is an energy level introduced by defects or impurities in the crystal lattice. The carrier can then be captured by the trap state, leading to a temporary immobilization. Subsequently, the trapped carrier can recombine non-radiatively with another free carrier, releasing its excess energy as heat or transferring it to a lattice vibration (phonon).

(e) Auger recombination [16]

In Auger recombination, a carrier (either an electron or a hole) recombines with another carrier, instead of emitting a photon, by transferring its excess energy to a third carrier. This leads to the production of a higher-energy carrier and the loss of energy as heat, rendering it undesirable for optoelectronic devices.

A positive trion is a type of charged exciton in semiconductors. It consists of two electrons and one hole bound together as a positively charged complex. Positive trions can form

when two electrons are excited across the bandgap and become trapped by a hole in the valence band.

A negative trion is another charged exciton in semiconductors, but it has a negative charge. It consists of two holes and one electron bound together in a negatively charged complex. Negative trions can form when two holes are excited across the bandgap and become trapped by an electron in the conduction band.

A biexciton is a doubly excited state in semiconductors, consisting of two electrons and two holes bound together. It is a complex with a net neutral charge. Biexcitons can form when two electrons and two holes are excited across the bandgap and become trapped near each other.

2.2 Photonic Crystal Devices

Different types of photonic crystals were introduced in Chapter One. Due to their unique optical properties and ability to control the behavior of light, PhCs have found numerous applications in various photonic devices. The principle behind PhC devices lies in the manipulation of light at the nanoscale using periodic structures with alternating regions of high and low refractive index. This periodicity creates a bandgap for certain wavelengths of light, prohibiting their propagation through the crystal while allowing other wavelengths to pass through or be manipulated.

2.2.1 Resonant Optical Cavities

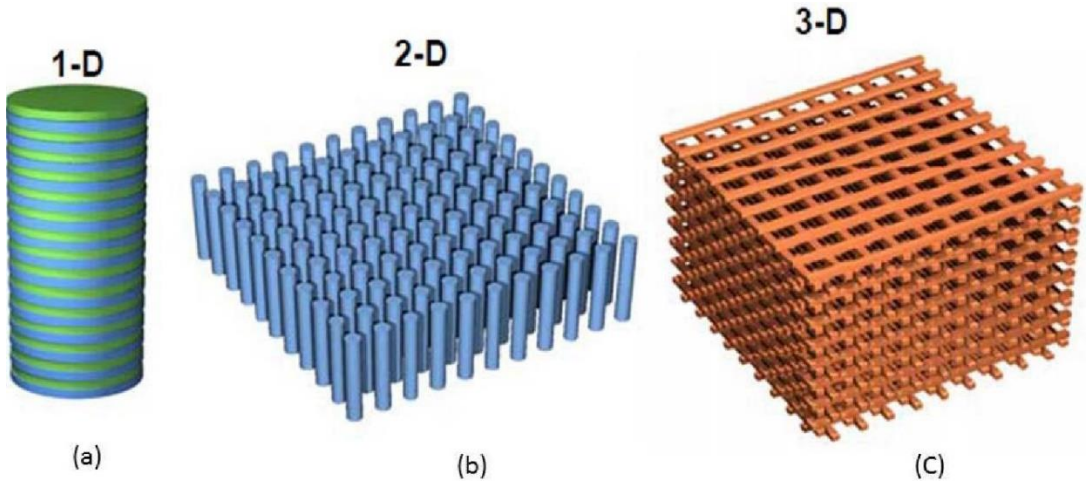

Figure 2.5 photonic crystals (a) 1D (b) 2D and (c) 3D [17]

Figure 2.5 provides a schematic representation of (a) 1D (b) 2D and (c) 3D PhCs. Semiconductor optical devices can improve device performance and regulate light emission by using different dimensions of PhC resonant optical cavities. These cavities are engineered to confine and manipulate light within the semiconductor structure, leading to improved efficiency, wavelength selectivity, and light extraction.

1D PhC cavities, such as DBRs, are precisely engineered constructs within semiconductor devices, characterized by alternating layers of materials with varying refractive indices. In formula 2.2. The reflectivity (R) of a DBR is determined by the refractive indices (n_1 and n_2) of the two alternating materials within the structure [18,19].

$$R = |(n_1\text{-}n_2)/(\, n_1\text{+}n_2)\, |^2 \tag{2.2}$$

In semiconductor lasers, they function as reflective mirrors, strategically positioned at the laser cavity's ends, imparting crucial optical feedback pivotal for laser oscillation [20-22]. This, in turn, intensifies light amplification and increases the overall laser efficiency. A meticulous design of DBR layer thicknesses facilitates the selective enhancement or suppression of distinct wavelengths, a pivotal attribute for realizing single-mode laser emission at targeted wavelengths. The fundamental formula 2.3 governing DBR design is [23,24]:

$$t_1 = \lambda_0\ /4n_1$$

$$t_2 = \lambda_0\ /4n_2 \tag{2.3}$$

Here, λ_0 represents the target wavelength of reflection, n_1 and n_2 denote the refractive indices of the high and low-index materials respectively, and t_1 and t_2 stand for the thicknesses of the respective layers.

In the realm of LEDs, DBRs assume the role of increasing the light-extraction. Placing a DBR beneath the active LED layer redirects otherwise trapped light within the semiconductor material toward the upper surface, resulting in elevated light extraction and LED efficiency [25-27]. The manipulation of DBR layer thicknesses enables the creation of resonant modes within the cavity, thus exerting influence over the emission characteristics of the device. This adaptability proves especially advantageous for applications necessitating precise emission features, such as achieving a fine-tuned emission spectrum or exercising control over emission direction. Although they can be very effective, DBRs considerably increase the complexity and the growth time for epitaxial structures.

3D PhC structures, depicted in Figure 2.5 (c), exhibit a remarkable ability to create a comprehensive photonic bandgap, effectively blocking the propagation of electromagnetic states across a frequency range in all directions. This extraordinary attribute allows for the confinement of light through defects in the periodic arrangement. Despite this exceptional potential, the fabrication of 3D PhC has proven to be challenging. Various methods have been extensively explored, including techniques like drilling [28], woodpiling [29], and self-assembly [30]. However, these processes are intricate and more difficult to control in comparison to the fabrication of two-dimensional PhC structures. This disparity in complexity and cost has acted as a deterrent, limiting in-depth research and development of 3D PhCs for photonic integration purposes.

2D PhC structures have proven particularly advantageous for the development of photonic integrated devices [31]. These planar structures facilitate the integration of various photonic devices, enabling efficient coupling of light in and out of the device. There are two common configurations for 2D PhC structures. The first involves creating holes within a membrane material, where there is a substantial refractive index contrast between the holes and the membrane. The second configuration employs high refractive index material pillars surrounded by air, as Figure 2.5 (b) depicts. In both cases, these structures prevent the existence of modes with frequencies within the photonic bandgap (PBG).

2.2.2 Band Diagrams of Two-dimensional Photonic Crystals

Band diagrams of 2D photonic crystals illustrate the allowed and forbidden energy ranges for electromagnetic waves within the crystal's structure. These diagrams depict the dispersion of energy states along the crystal's wavevector directions, revealing the presence of photonic bandgaps where certain frequencies cannot propagate. In a 2D PhC, the band diagram shows multiple photonic bands separated by these bandgaps, reflecting the unique periodic arrangement of the crystal. These diagrams provide insights into the optical properties, such as mode confinement and light propagation, and aid in designing and optimizing photonic devices based on these structures.

The inherent mirror symmetry of 2D PhCs across all perpendicular planes results in electromagnetic waves exhibiting distinct polarization behaviors. Specifically, these waves polarize either parallel to the electric field within the crystal plane, known as transverse electric (TE) polarization, or perpendicular to the electric field, termed transverse magnetic (TM) polarization [32,33]. Notably, hole-based PhCs tend to exhibit stronger TE-like bandgaps, while structures featuring pillars are more conducive to TM-like bandgaps [33]. This distinction arises from the continuous flow of electric field lines within hole-based structures and the unique characteristics of pillars in shaping polarization-dependent bandgap properties.

This study primarily concentrates on 2D PhC membrane structures encased in air, which doesn't induce a photonic bandgap in the z direction but effectively reduces losses by maintaining a favorable refractive index contrast. There are different kinds of these 2D PhC structures shown in Figure 2.6 including (a) square lattice, (b) triangular lattice, and (c) hexagonal lattice. Our work will solely focus on the square lattice 2D PhC membrane structures encased in air.

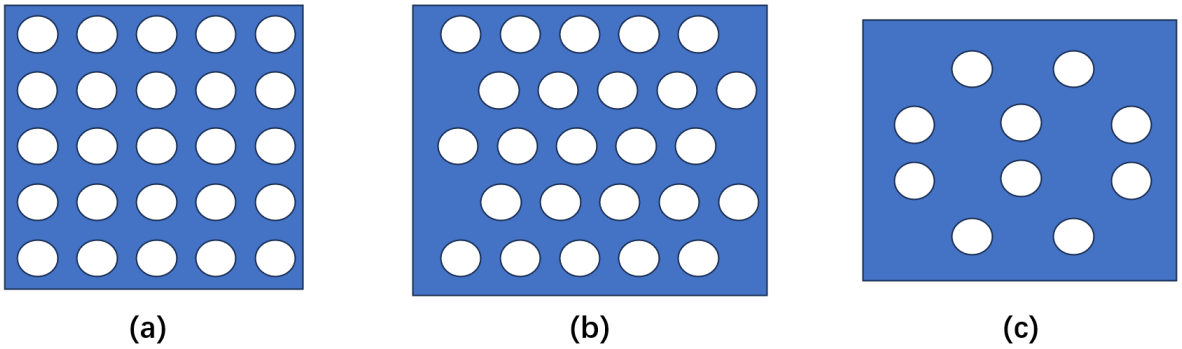

Figure 2.6 2D PhC structures (a) square lattice, (b) triangular lattice, and (c) Graphite- type hexagonal lattice.

The Brillouin zone is a fundamental concept in the study of periodic structures, particularly crystal lattices, serving as a geometric representation in reciprocal space that captures the symmetry and periodicity of a crystal lattice. It plays a crucial role in understanding the electronic and vibrational properties of materials, especially in solid-state physics and condensed matter research. In a crystal lattice, the Brillouin zone is the smallest unit cell in reciprocal space that encompasses the reciprocal lattice, providing a reference for describing the allowed energy states of electrons and phonons [34]. Divided into distinct parts, it characterizes different electronic states or vibrational modes. High-symmetry points within the Brillouin zone aid in material property characterization, such as analyzing electronic band structures. Figure 2.7 shows the 2D (a) square and (b)hexagonal Brillouin zone in reciprocal space.

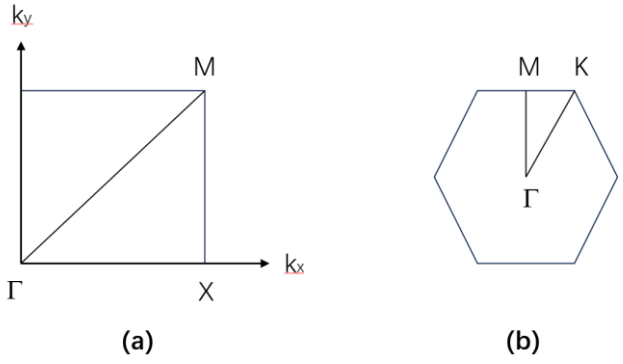

Figure 2.7 the 2D (a) square and (b)hexagonal Brillouin zone.

For GaAs, which possess a zinc-blende crystal structure, its 2D Brillouin zone shape is determined by its lattice symmetry. For a specific crystallographic plane, like the (001) plane, the 2D Brillouin zone adopts a square configuration, as depicted in Figure 2.7 (a). This square shape arises from the square lattice symmetry of GaAs's (001) plane, projecting its Brillouin zone onto this plane. The wave vectors within the square Brillouin zone follow the path ΓMXΓ. On the other hand, GaN features a wurtzite crystal structure characterized by hexagonal unit cells. In GaN, considering the (0001) plane, its 2D Brillouin zone takes the form of a hexagon, illustrated in Figure 2.7 (b). This hexagonal shape emerges due to the hexagonal lattice symmetry of GaN's (0001) plane, projecting its Brillouin zone onto this plane. The wave vectors within the hexagonal Brillouin zone traverse the path ΓMKΓ.

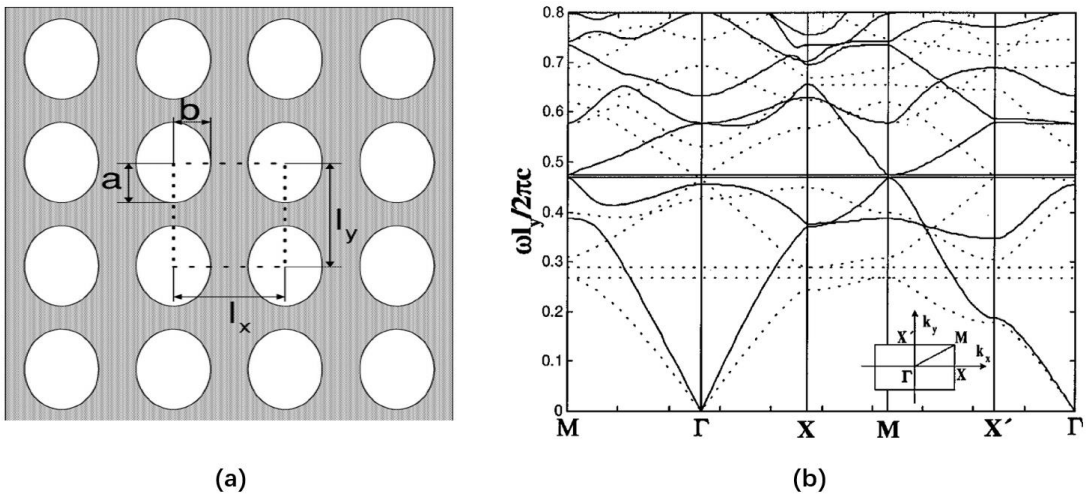

Figure 2.8 (a) 2D square photonic crystal (PhC) structures (b) Band structure for a 2D photonic crystal with circular air holes on GaAs material [35].

Let's consider GaAs 2D square PhC structures as an illustrative example. In Figure 2.8 (a), we observe a 2D array of air holes arranged in a periodic rectangular pattern within the GaAs material. The air hole radius is denoted as r (= a = b) = $0.38l_y$. The ratio of periods is $l_x/l_y = 0.77$, while the refractive index of GaAs is 3.85. Moving to Figure 2.8 (b), we examine the band structure of this 2D photonic crystal featuring circular air holes on the GaAs substrate. The solid curves correspond to TM polarization, while the dotted curves pertain to TE polarization. The photonic bandgap, represented between two solid lines, emerges within this region, rendering TE-polarized electromagnetic modes available.

The tuning of the hole radius (r) relative to the lattice constants (I_x and I_y) and the index contrast between the holes and the membrane offers control over the enhancement of the photonic bandgap. A smaller r/I ratio results in a narrower bandgap that increases linearly with this ratio. However, an escalating r leads to heightened loss rates due to reduced guiding material and fabrication challenges due to intricate features between larger holes. Consequently, a compromise arises between the bandgap size and practical limitations. The bandgap's frequency hinges on the effective refractive index of the entire structure. Elevating the air content in the structure by increasing r/I amplifies the central bandgap frequency. In Figure 2.9, while maintaining a constant ratio of periods (I_x/I_y = 0.77), we modify r by increasing a from $0.38I_y$ to $0.45I_y$, while keeping b constant at $0.38I_y$. Notably, the bandgap (shaded region) substantially expands. Thus, in a purely 2D structure, the bandgap's magnitude and location are determined by the hole size (r), lattice constant (I_x and I_y), and refractive index of the material.

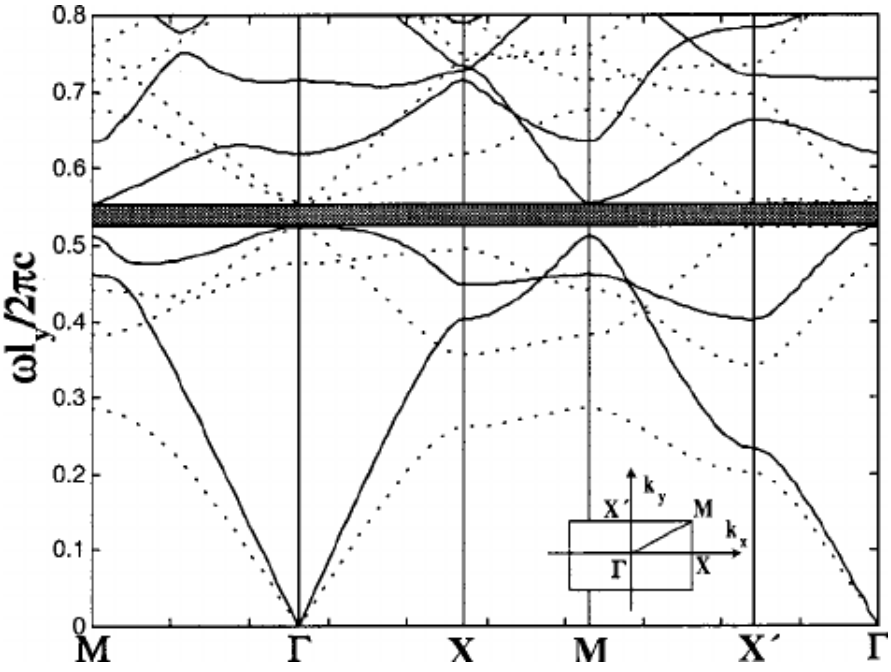

Figure 2.9 Band structure for a 2D photonic crystal with circular air holes on GaAs material [35].

2.2.3 Purcell Effect

The Purcell effect refers to the enhancement of spontaneous emission rate of an excited quantum system, such as an atom, molecule, or quantum dot, when it is placed in a resonant optical cavity. This phenomenon arises from the interaction between the quantum emitter and the electromagnetic modes within the cavity [36]. According to the Purcell effect, the emission rate is modified by the density of optical states at the emitter's transition frequency and the quality factor of the cavity. When the emitter's transition frequency matches the resonant frequency of the cavity, the Purcell effect can significantly increase the probability of photon emission, leading to faster radiative decay. This effect has important implications for various applications, including enhancing the efficiency of light-emitting devices, quantum information processing, and studying strong coupling between light and matter in cavity quantum electrodynamics.

The Purcell factor quantifies the enhancement of the spontaneous emission rate of an emitter when it is placed inside a resonant cavity compared to when it is in free space [36-38]. In simple terms, it provides a measure of how strongly an emitter can couple to a particular mode in a cavity, and as a result, how its spontaneous emission properties can be modified by its environment.

The Purcell factor (F_p) is a dimensionless quantity that quantifies the enhancement of the spontaneous emission rate of a quantum emitter placed inside a resonant optical cavity. It is defined by the formula 2.4:

$$F_P = \frac{3}{4\pi^2}\left(\frac{\lambda}{n}\right)\frac{Q}{V} \tag{2.4}$$

Where λ represents the wavelength of emitted light, n is the refractive index of the medium, Q is the quality factor measuring cavity energy storage, and V stands for the mode volume of the cavity mode aligned with the emitter's transition frequency.

The quality factor (Q factor) is a fundamental parameter that describes the behavior of resonant systems, such as optical cavities and mechanical oscillators. It reflects the ratio of

the energy stored in the system to the energy dissipated per cycle when the system undergoes damped oscillations. The higher the Q factor, the less energy is lost per cycle, resulting in a more pronounced resonance and longer oscillation times.

Equation 2.5 presents the determination of the quality factor (Q), with ω_0 representing the resonant frequency and FWHM denoting the full width at half maximum of the resonance peak within the frequency domain.

$$Q = \frac{\omega_0}{FWHM} \tag{2.5}$$

In optical systems, a higher Q factor indicates stronger light confinement and longer photon lifetimes within the resonant cavity. This property is crucial for applications such as lasers, where a high Q factor enhances stimulated emission and lasing action.

2.2.4 Photonic Crystal Light Emitting Diode

Figure 2.10 shows the structure of a common type AlGaAs/GaAs LED. The LED will emit at around 850nm and is commonly found as an infrared emitter (for example, in an infrared remote control or security illumination). The LED structure typically consists of the following layers: N-type GaAs substrate, N-type AlGaAs, N-type AlGaAs, Active region, P-type AlGaAs, and P-type GaAs. Metal contacts are added to the n- and p-type layers to facilitate electrical connections.

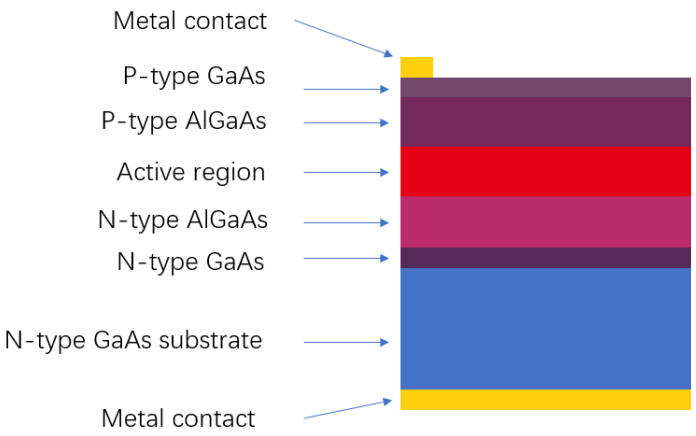

Figure 2.10 the structure of a common type AlGaAs/GaAs LED.

The LED active region is a crucial component within an LED that is responsible for generating light through the process of electron-hole recombination. It is strategically designed to maximize the efficiency of this recombination process and, consequently, the emission of photons. We discussed semiconductor nanostructure in Chapter One. Here we describe some types of LED active regions including (a) QD), (b) QW, (c) MQWs, (d) MQDs, and (e) QW and QD shown in Figure 2.11.

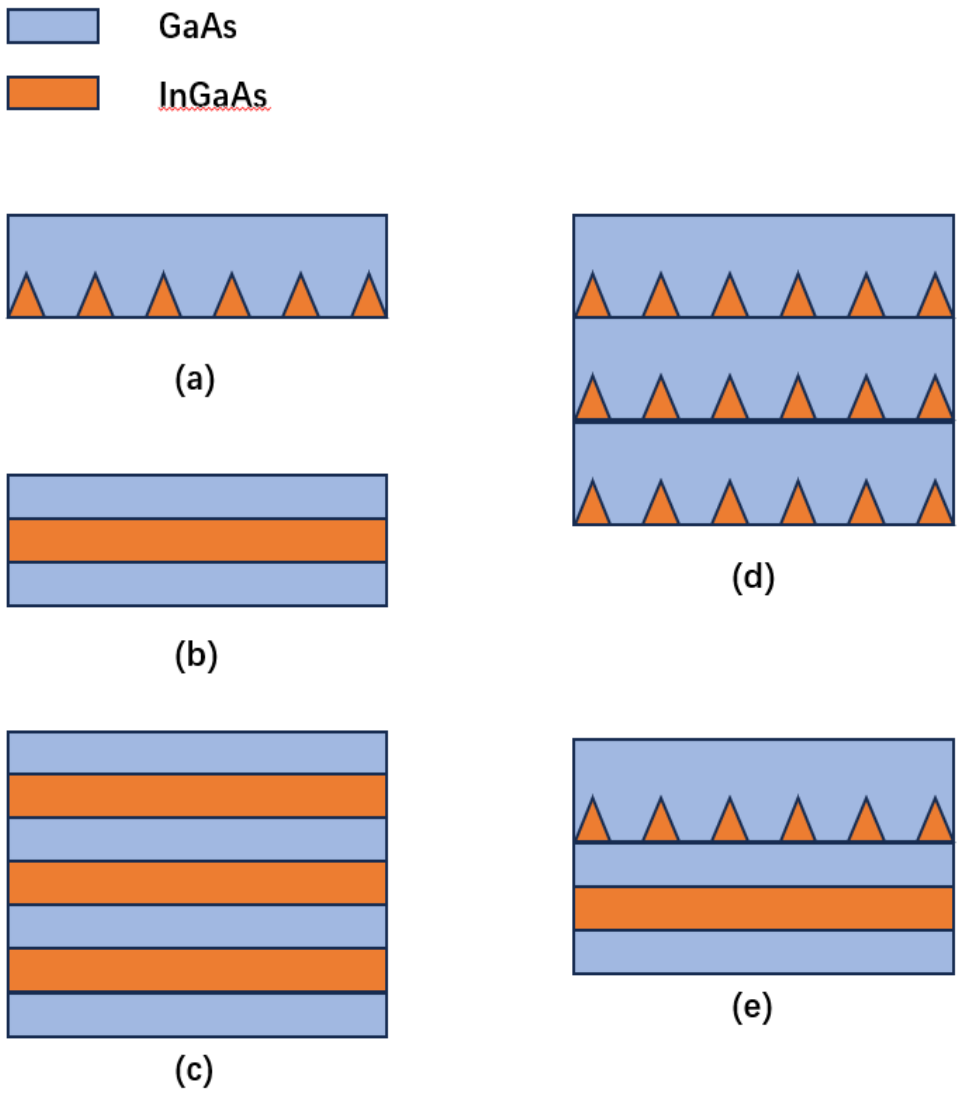

Figure 2.11 Different types of LED active regions (a) Quantum Dot, (b) Quantum Well, (c) Multiple Quantum Wells, (d) Multiple Quantum Dots, and (e) Quantum Well and Quantum Dot

QD and QW-based LEDs utilize quantum mechanical properties for enhanced light emission, showing advancements in semiconductor technology in lighting, displays, and telecommunications.

A QD-based LED employs quantum dots [39-41], which are nanoscale semiconductor particles with quantized energy levels. When a voltage is applied, electrons and holes are confined within the discrete energy levels of the quantum dots. As these charges recombine, they emit photons with precise wavelengths determined by the quantum dot, allowing for tunable and

narrowband emission. In a QW-based LED [42-44], a thin layer with a lower energy bandgap (quantum well) is sandwiched between two layers with higher energy bandgaps (barrier layers). This arrangement confines electrons and holes within the quantum well, enhancing carrier recombination and photon emission efficiency. QW-based LEDs provide control over emission wavelengths by adjusting the thickness of the quantum well layer. Multiple quantum wells are stacked layers of quantum wells with different bandgaps. They provide enhanced carrier confinement and recombination due to the multiple potential barriers. Similar to MQWs, MQDs involve multiple layers of quantum dots. MQDs can offer enhanced carrier capture and emission, potentially leading to improved LED performance. Quantum Well and Quantum Dot hybrid structure combines the benefits of quantum wells and quantum dots. It allows tailored control over carrier dynamics and emission characteristics, leading to optimized LED performance.

PhC LEDs combine the principles of PhC with LED technology to create advanced light sources with improved optical characteristics, making them promising candidates for various applications in lighting, displays, and communication systems.

1D PhC LEDs are advanced devices combining 1D PhCs (DBR) for efficient control and manipulation of light emission in various applications [25-27]. In 1D PhC-LEDs, the periodic structures in PhCs enhance the LED's efficiency by directing light emission more effectively, reducing losses; the DBRs can be engineered to reflect specific wavelengths, providing precision control over the light's spectrum; and, compared to conventional LEDs that emit light randomly, the inclusion of DBRs ensures a more focused light emission. Consequently, this synergy between PhCs and LEDs paves the way for advanced optoelectronic devices, elevating the performance of LED-based displays and lighting systems.

Figure 2.12 (a) illustrates the integration of AlGaAs/GaAs LED with 2D PhC structures. In contrast to 1D PhC structures (DBR), the fabrication process for 2D PhC LED employs a top-down approach. As mentioned earlier, various techniques such as EBL, and NIL can be employed to achieve this objective. Through the incorporation of a precisely engineered 2D PC structure into the LED, these devices attain exceptional control over the emitted light's properties. The periodic arrangement of materials in the 2D PC generates bandgaps that influence the transmission of specific wavelengths, enabling tailored emission spectra and

improved light extraction efficiency (LEE). Figure 2.12 (b) displays the SEM image of 2D PhC structures on the LED.

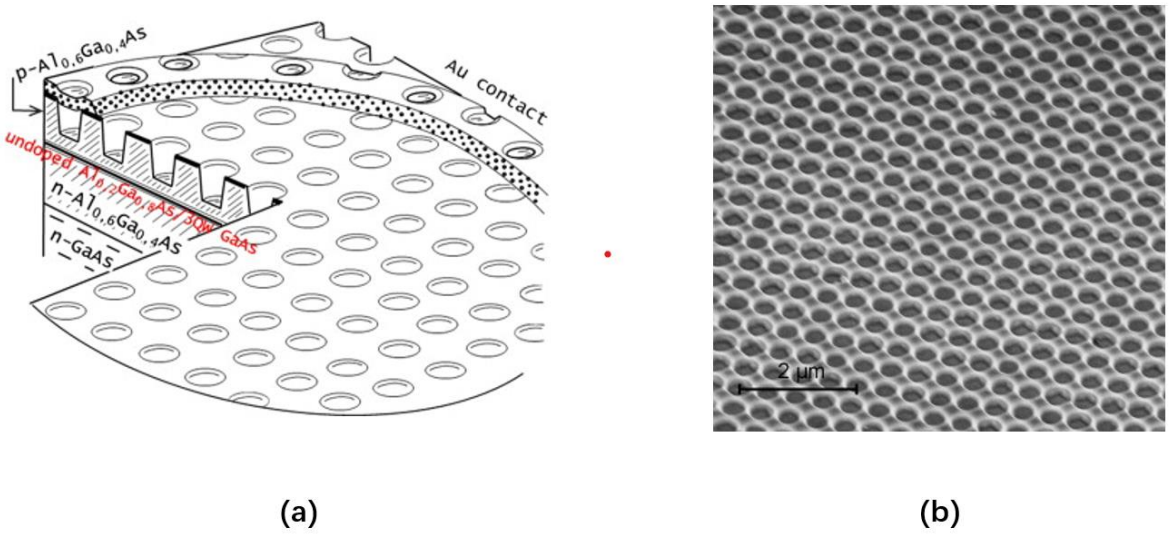

Figure 2.12 (a) the combination of 2D PhC structures and AlGaAs/GaAs LED (b) the SEM of 2D PhC structures on the LED [45].

2.3 Laser Interference Lithography

Laser interference lithography (LIL) is a precision nanofabrication technique that employs the interference patterns of laser beams to create intricate periodic structures on a substrate [46,47]. In this process, coherent laser beams are directed onto a photosensitive material, causing the constructive and destructive interference of light waves. In regions of constructive interference, the amplitudes of the individual waves reinforce each other, resulting in higher intensity and bright fringes. In regions of destructive interference, the amplitudes cancel each other out, leading to lower intensity and dark fringes.

2.3.1 Key Milestones of Laser Interference Lithography

By the 1970s and 1980s, as the importance of nanotechnology and microfabrication began to be realized, LIL started gaining traction. This method offered a way to bypass the resolution limitations of traditional lithographic methods, especially as the need for smaller structures in semiconductor manufacturing grew [48]. As laser technology improved, LIL gained enhanced precision in generating nanoscale features, finding applications in photonics [49], plasmonics [50], bioengineering [51], magnetic storage [52], nanofluidics [53], and various research domains.

2.3.2 Two-beam Laser Interference Lithography

One of the most popular two-beam laser interference lithography setups is called Lloyd's mirror interferometer [54,55], which is an optical setup used to create interference patterns by splitting a light beam into two paths and then recombining them, as shown in Figure 2.13. The Lloyd's mirror interferometer comprises a beam splitter, a mirror, and a viewing screen. The beam splitter separates the incoming light beam into two components: one is directly reflected by the mirror, while the other is reflected from the surface of the beam splitter. These two beams then overlap on the viewing screen, creating interference fringes due to their phase difference. This setup is named after its inventor, Humphrey Lloyd. It is commonly used in optics experiments and provides insights into wave properties of light and the principles of interference.

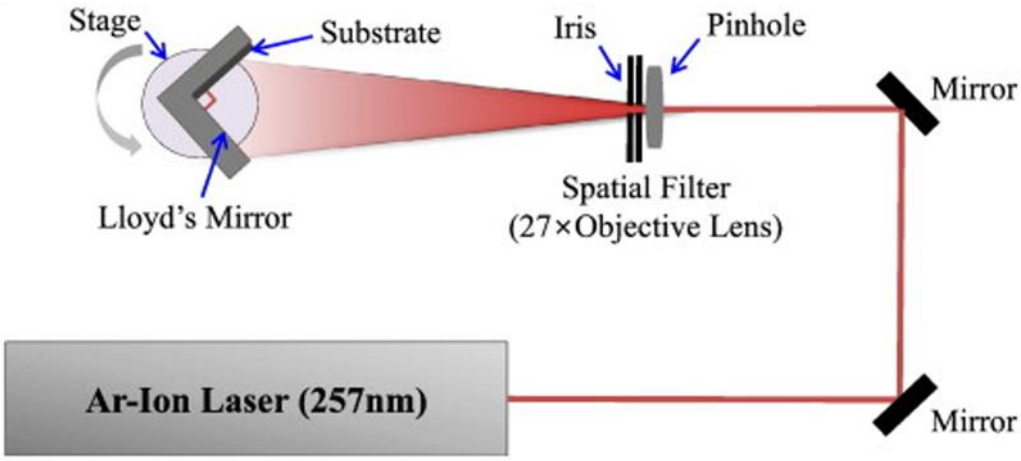

Figure 2.13 The setup of Lloyd's mirror interferometer [56].

The principle of two-beam laser interference lithography entails the overlapping of two coherent laser beams, sharing the same wavelength, onto a substrate, as depicted in Figure 2.14 (a). These laser beams are symmetrically projected onto the substrate at a predetermined angle of incidence. The interaction of these two laser beams leads to the formation of line interference fringe patterns on the substrate's surface. Following the pattern exposure during the subsequent development steps, line-patterned structures can be achieved. Figure 2.14 (b) shows an example of the two-beam interference SEM result pattern. The resulting intensity distribution of these interference fringe patterns can be mathematically represented by the equation (2.6) [46].

$$I = I_1 + I_2 + 2\sqrt{I_1 I_2}\cos\phi \tag{2.6}$$

In this formula, I_1 and I_2 represent the intensities of the two light beams, and ϕ representing the phase difference between these beams at a particular X-coordinate on the photoresist layer, as articulated by equation (2.7) [46].

$$\phi = \frac{2\pi}{\lambda} x \cos 2\theta \tag{2.7}$$

The resulting interference pattern's period, denoted as P, is contingent upon factors including the laser's wavelength, λ, the photoresist's refractive index, n, and the angle, θ, at which the two beams intersect. This relationship is illustrated by the equation (2.8) [46,56,57] provided below.

$$P = \frac{\lambda}{2\sin\theta} \tag{2.8}$$

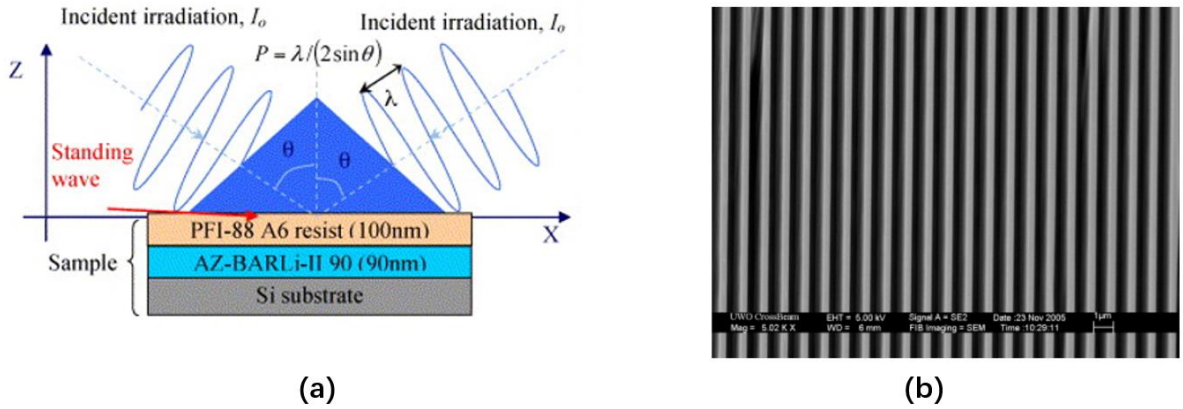

Figure 2.14 (a) The creation of line interference fringe patterns through two-beam interference [58]. (b) The SEM pattern of two-beam interference [59].

2.3.3 Multi-beam Laser Interference Lithography

The principle of multi-beam LIL involves the simultaneous superposition of multiple coherent laser beams onto a substrate to create intricate patterns. By controlling the angles and phases of the laser beams, complex interference patterns can be generated, allowing for the precise patterning of nanostructures and photonic devices. This technique harnesses the constructive and destructive interference of the laser beams to create fine features on the substrate's surface, enabling high-resolution and scalable fabrication processes.

Various laser interference setups are available for multi-beam LIL. Notably, Lloyd's mirror interferometer, designed for two-beam LIL, accomplishes this with first exposure, yielding one-dimensional line patterns. A 90-degree rotation of the sample for a second exposure generates two-dimensional dot patterns, exemplified in Figure 2.15.

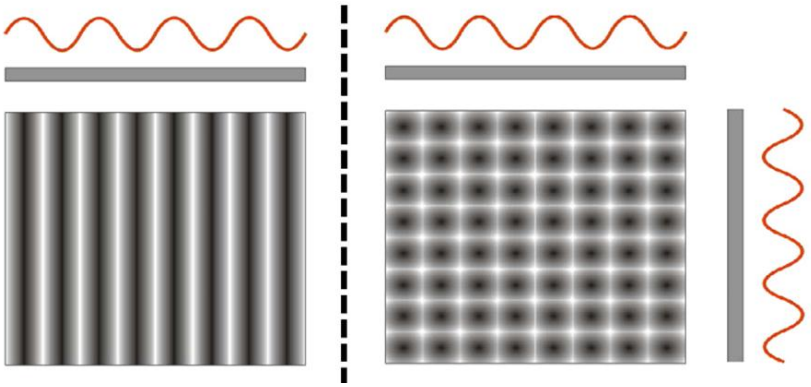

Figure 2.15 SEM images of (left) one-dimensional and (right) two-dimensional patterns [56].

Figure 2.16 (a) shows a LIL setup which uses diffractive optic elements (DOE) to split the beams [60-62]. In this setup, a coherent laser source emits a light beam, which is then collimated to achieve a uniform and parallel beam. The laser beam is then directed towards a DOE, which consists of microstructured patterns that impose phase shifts on the incident light, causing it to split into multiple beams with specific angles and intensity distributions. These diffracted beams interfere with each other, creating complex interference patterns that determine the resulting nanostructure. The DOE design and fabrication need to be tailored to achieve the desired interference patterns and angles. The modulated beam is directed onto a substrate coated with photoresist. The exposure process creates a patterned distribution of light intensity on the sample, resulting in a photochemical or physical change in the photoresist. Subsequent processing steps, development, and etching, transfer the pattern onto the substrate.

In laser interference lithography setups shown in Figure 2.16 (b), a Spatial Light Modulator (SLM) is used to control the laser beams splitting [63,64]. SLMs are advanced optical devices that can modify the phase, amplitude, or polarization of light spatially across a two-dimensional plane. A phase only SLM works are a reconfigurable DOE. In this setup, a coherent laser beam is directed toward the SLM, which consists of an array of controllable pixels. Each pixel can be individually manipulated to impose specific phase shifts on the incident light passing through it. The laser beam passes through the SLM, where its properties are dynamically modified according to a predetermined pattern. By altering the phase of the light waves across the SLM's surface, the beam's trajectory can be adjusted, leading to the

formation of complex interference patterns, which can be tailored to achieve specific nanostructure designs. After passing through the SLM, the laser beam encounters additional optical components such as lenses, mirrors, and beam splitters to further manipulate its properties and direct it toward the substrate coated with the photoresist. The interference patterns created by the modified laser beams expose the photoresist. Further processing stages involve development and etching, which facilitate the transfer of the exposed pattern onto the substrate, thereby facilitating the creation of intricate nanostructures.

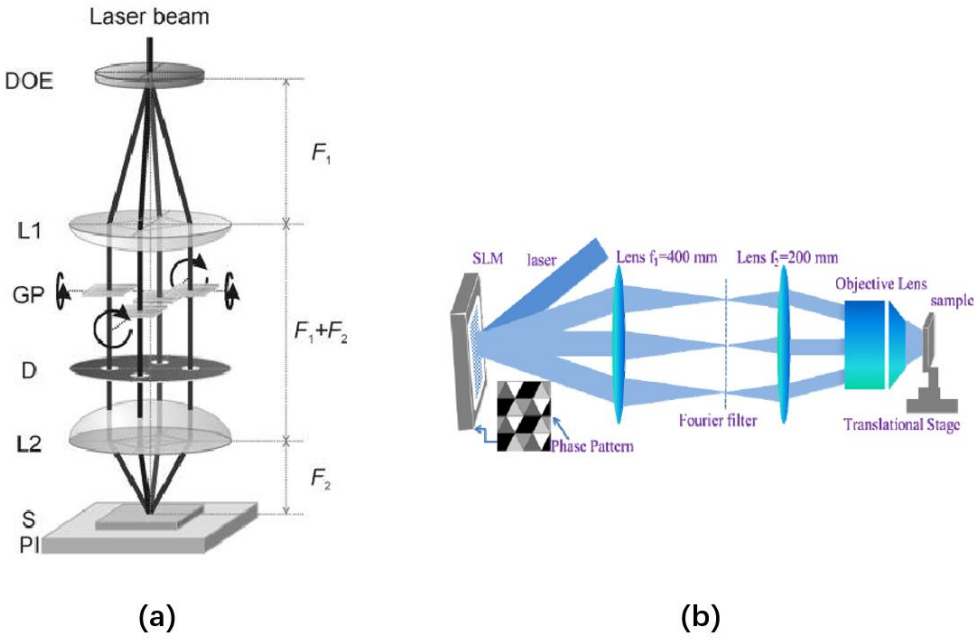

Figure 2.16 LIL setup diagrams of (a) the DOE configuration [65], (b) the SLM configuration [63].

Several of the above setups can implement multi-beam LIL and are widely used. However, these methods have certain constraints, such as the need for precise incidence angle adjustments, susceptibility to polarization effects, low laser power thresholds (especially for SLMs), and limited interference pattern resolution. As a more flexible solution to these basic arrangements, setups employing beam splitting and steering offer greater versatility for multi-beam interference lithography, especially when diverse incidence angles and polarizations are necessary. Furthermore, they can effectively manage high laser power intensities. Figure 2.17 illustrates a schematic representation of a 4-beam LIL configuration achieved through beam splitting.

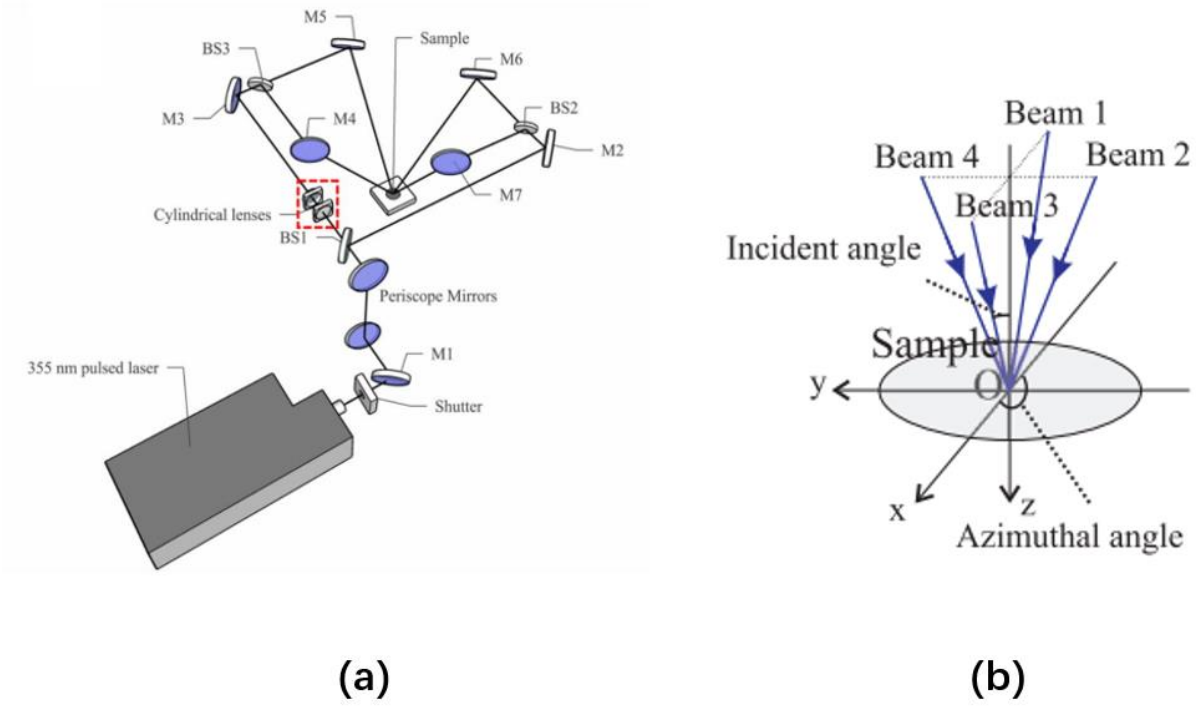

Figure 2.17 (a) Four-beam lithography configuration by beam splitting and beam steering [66] (b) Scheme of the four-beam interference system [67].

Multi-beam interference can be understood as the linear combination of numerous coherent electromagnetic waves. This entails the summation of electric field vectors to define the overall intensity distribution. The calculation of the intensity distribution for N-beam interference in the z = 0 plane can be expressed as the following equation (2.9) [68-70]:

$$I = \left|\sum_{i=1}^{n} \overrightarrow{E_i}\right|^2 \tag{2.9}$$

The electric field vector of the mth beam can be expressed as formula (2.10):

$$\overrightarrow{E_m} = A_m \overrightarrow{P_m} exp\left[i\left(\overrightarrow{k_m} * \vec{r} + \delta_m\right)\right] \tag{2.10}$$

In formula (2.10), A_m signifies the amplitude, $\overrightarrow{P_m}$ denotes the unit polarization vector, $\overrightarrow{k_m}$ represents the wave vector indicating the direction of propagation, $\vec{r}$ is the position vector, and signifies the initial phase. In formula (2.10), the quantities $\overrightarrow{P_m}$, $\overrightarrow{k_m}$, and $\vec{r}$ are functions dependent on spatial coordinates, which can be expressed individually as follows:

$$\overrightarrow{P_m} = -(\cos\theta_m \cos\varphi_m \cos\psi_m - \sin\varphi_m \sin\psi_m) * \vec{\imath}$$

$$-(\cos\theta_m \cos\varphi_m \cos\psi_m + \sin\varphi_m \sin\psi_m) * \vec{j}$$

$$-(\sin\theta_m \cos\psi_m) * \vec{k} \quad (2.11)$$

$$\overrightarrow{k_m} = k\left(\sin\theta_m \cos\varphi_m * \vec{\imath} + \sin\theta_m \sin\varphi_m * \vec{j} - \cos\theta_m * \vec{k}\right) \quad (2.12)$$

$$\vec{r} = x * \vec{\imath} + y * \vec{j} + z * \vec{k} \quad (2.13)$$

$$k = \frac{2\pi}{\lambda} \quad (2.14)$$

Here, k stands for the wave number, λ corresponds to the laser wavelength, θ_m denotes the angle of incidence, φ_m represents the azimuthal angle, and ψ_m signifies the polarisation angle.

2.3.4 Direct Laser Interference Lithography

Direct Laser Interference Lithography (DLIL) [71-73] is a nanofabrication technique that uses the interference patterns of coherent laser beams to create intricate patterns directly on semiconductor substrates like Si, and GaN without a transfer medium (photoresist). This process involves the superposition of multiple laser beams with a generally high power, resulting in interference fringes that expose materials. DLIL offers precise control over pattern geometry and is suitable for applications requiring complex periodic or quasi-periodic structures.

Using Si as an illustration [74], consider Figure 2.18 (a) which depicts the outcome of a single pulse from a four-beam DLIL pattern applied to the Si surface. The interference field's energy is sufficiently intense to induce localized melting and ablation on the Si surface. When energetic photons are absorbed by a solid, they can induce lasting alterations by causing processes like melting and re-solidification, vaporization, or material ablation. The molten Si particles disperse across the Si surface within the interference region, and this ablation process continues with subsequent laser pulses. Moving to Figure 2.18 (b), the Si surface subjected to 300 laser pulses reveals that the molten silicon has been deposited within the

illuminated area influenced by laser interference. Si in the vapor phase migrates to the interstitial spaces between these enhanced areas. This subsequently enlarges the etching holes, allowing the Si deposition process to persist. Ultimately, this leads to the formation of tapered cones featuring glossy Si formations.

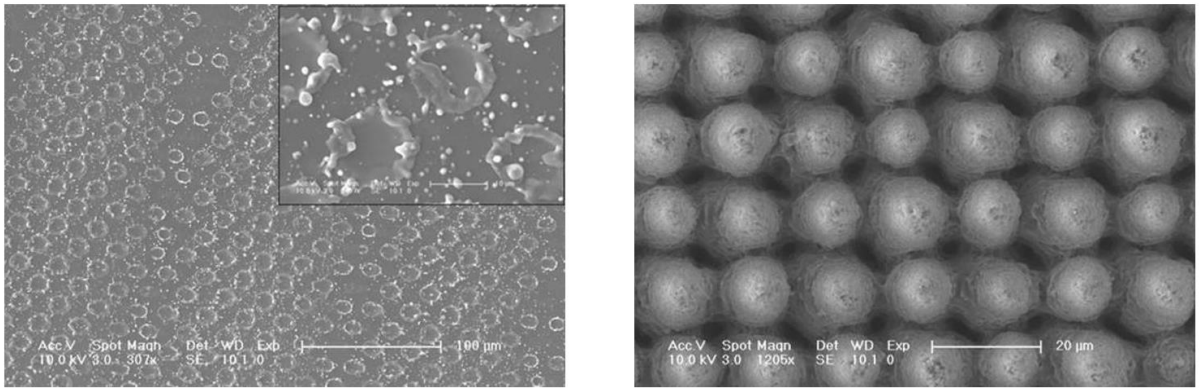

(a) (b)

Figure 2.18 SEM images of Si surface structures formed by four-beam interference lithography with (a) one pulse and (b) 300 pulses.

There are clear advantages in using DLIL to directly structure the surface. However, the complexity of the laser-material interaction and the potential for surface damage has made this approach difficult to employ to relatively low melting point materials, such as semiconductors.

2.4 Multi-beam Laser Interference Lithography Patterns

The shape of the interference pattern is governed by equations (2.10-2.14), which are influenced by factors such as polarization orientations and the count of beams. Concurrently, the incident angle and laser wavelength impact the periodicity of the resultant intensity distribution. This implies that when employing more than two beams, a diverse range of two-

dimensional array patterns can be achieved, encompassing circular, square, triangular, and hexagonal geometries.

To investigate the effects of varying beam parameters on the resulting interference patterns, theoretical simulations were executed using MATLAB. The simulations adopted a laser wavelength of 355 nm, equal amplitudes for all incident beams, and zero initial phases. Illustrated in Figure 2.19 and Figure 2.10 are the simulated distributions of interference intensities achieved by manipulating the number of interfering beams. These simulations consider the symmetrical placement of all interfering beams at identical incidence angles of 30°.

Displayed in Figure 2.19 are laser interference patterns generated by varying beams, ranging from 2 to 7 beams. The polarization angle is fixed at 0°, designating the TM mode [75,76]. Within this mode, the period adheres to equation (2.15).

$$P = \frac{\lambda}{\sqrt{2}\sin\theta} \tag{2.15}$$

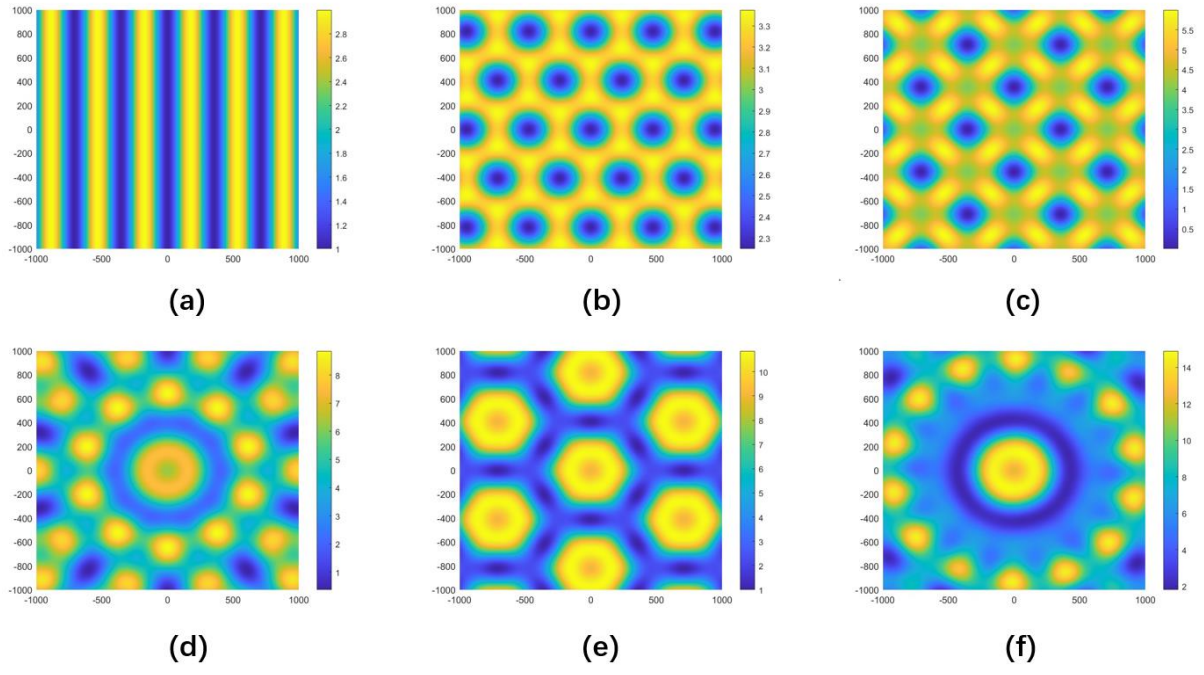

Figure 2.19 Simulation of interference patterns by (a-f) 2-, 3-, 4-, 5-, 6-, 7-beam interference (TM mode), respectively. The unit of the x and y-axis is nm.

Illustrated in Figure 2.20 are laser interference patterns resulting from a varying number of beams, ranging from 2 to 7 beams. The polarization angle is fixed at 90°, signifying the TE mode [69,77,78]. Within the TE mode, the period adheres to equation (2.16).

$$P = \frac{\lambda}{2\sin\theta} \tag{2.16}$$

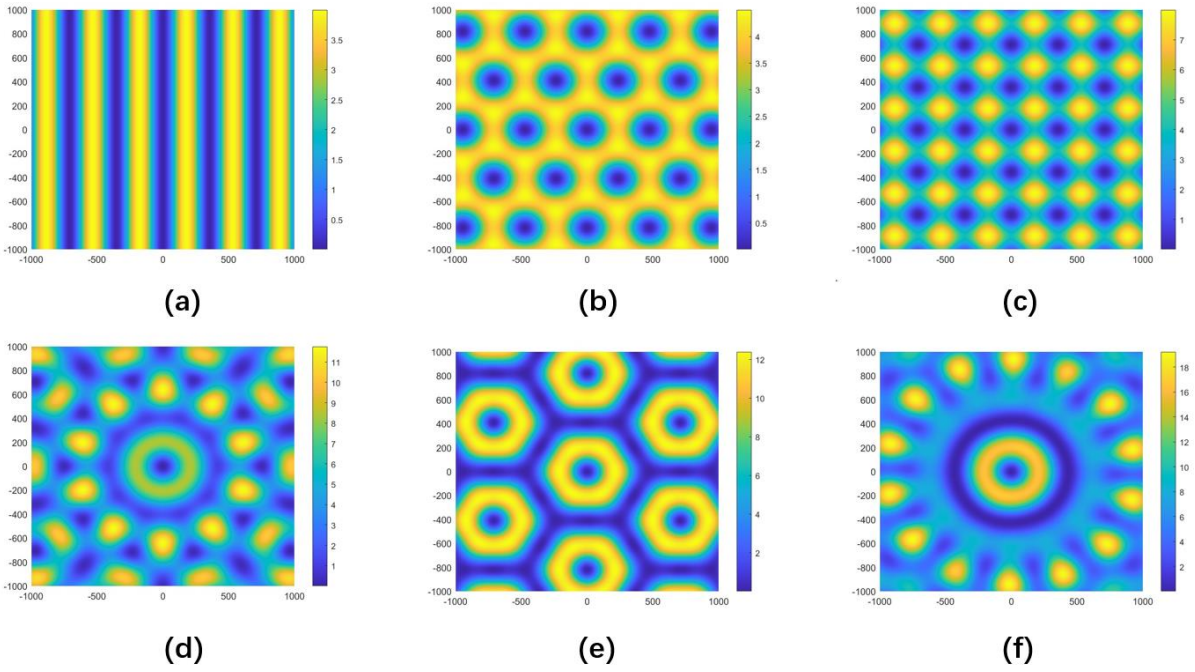

Figure 2.20 Simulation of interference patterns by (a-f) 2-, 3-, 4-, 5-, 6-, 7-beam interference (TE mode), respectively. The unit of the x and y-axis is nm.

References

[1] J. R. Hook and H. E. Hall, "Solid state physics," vol. 30, John Wiley & Sons, 1995.

[2] W. D. Callister and D. G. Rethwisch, "Materials Science and Engineering: An Introduction," Eighth Edition, John Wiley & Sons, Inc., 2010.

[3] L. S. Miller and J. B. Mullin (Eds.), "Electronic materials: from silicon to organics," Springer Science & Business Media, 2012.

[4] L. D. Yuan, H. X. Deng, S. S. Li, S. H. Wei, and J. W. Luo, "Unified theory of direct or indirect band-gap nature of conventional semiconductors," Physical Review B, vol. 98, no. 24, p. 245203, 2018.

[5] S. S. Li and S. S. Li, "Optical properties and photoelectric effects," in Semiconductor Physical Electronics, pp. 213-245, 1993.

[6] M. A. Reshchikov, "Measurement and analysis of photoluminescence in GaN," Journal of Applied Physics, vol. 129, no. 12, 2021.

[7] A. Amo, M. D. Martín, L. Viña, A. I. Toropov, and K. S. Zhuravlev, "Interplay of exciton and electron-hole plasma recombination on the photoluminescence dynamics in bulk GaAs," Physical Review B, vol. 73, no. 3, p. 035205, 2006.

[8] A. Buckley (Ed.), "Organic light-emitting diodes (OLEDs): materials, devices and applications," Elsevier, 2013.

[9] R. Mach, "Electroluminescence in Polycrystalline Semiconductors," in Polycrystalline Semiconductors: Physical Properties and Applications: Proceedings of the International School of Materials Science and Technology at the Ettore Majorana Centre, Erice, Italy, July 1–15, 1984, pp. 186-208, Springer Berlin Heidelberg, 1985.

[10] F. Scholz, "Compound Semiconductors: Physics, Technology, and Device Concepts," CRC Press, 2017.

[11] M. A. Reshchikov and H. Morkoç, "Luminescence properties of defects in GaN," J. Appl. Phys., vol. 97, no. 6, pp. 5–19, 2005.

[12] G. H. Wannier, "The structure of electronic excitation levels in insulating crystals," Phys. Rev., vol. 52, no. 3, p. 191, 1937.

[13] W. Y. Liang, "Excitons," Phys. Educ., vol. 5, no. 4, p. 226, 1970.

[14] R. N. Hall, "Electron-hole recombination in germanium," Phys. Rev., vol. 87, no. 2, p. 387, 1952.

[15] W. Shockley and W. T. Read Jr, "Statistics of the recombinations of holes and electrons," Phys. Rev., vol. 87, no. 5, p. 835, 1952.

[16] J. Iveland, L. Martinelli, J. Peretti, J. S. Speck, and C. Weisbuch, "Direct measurement of Auger electrons emitted from a semiconductor light-emitting diode under electrical injection: identification of the dominant mechanism for efficiency droop," Phys. Rev. Lett., vol. 110, no. 17, p. 177406, 2013.

[17] S. Robinson and R. Nakkeeran, "Photonic crystal ring resonator based optical filters," Advances in Photonic Crystals, vol. 1, pp. 1-26, 2013.

[18] R. K. Sharma, S. D. Gupta, H. S. Jatana, and S. Singh, "Effect of optical parameters on design of highly reflecting distributed Bragg reflectors based on compound semiconductors for space applications," Bulletin of Materials Science, vol. 44, pp. 1-7, 2021.

[19] D. Keskar, S. Survase, and M. Thakurdesai, "Designing Of Distributed Bragg Reflector (DBR) by Transfer Matrix Method," in 2021 4th Biennial International Conference on Nascent Technologies in Engineering (ICNTE), pp. 1-3, IEEE, 2021.

[20] W. Streifer, D. Scifres, and R. Burnham, "Coupled wave analysis of DFB and DBR lasers," IEEE Journal of Quantum Electronics, vol. 13, no. 4, pp. 134-141, 1977.

[21] P. Xing, H. Olesen, and B. Tromborg, "A theoretical model of multielectrode DBR lasers," IEEE journal of quantum electronics, vol. 24, no. 12, pp. 2423-2432, 1988.

[22] B. A. Taha, M. S. Mehde, A. J. Haider, and N. Arsad, "Mathematical model of the DBR laser for thermal tuning: Taxonomy and performance effectiveness with PbSe materials," Journal of Optics, pp. 1-11, 2022.

[23] A. A. Sharhan, "Transfer matrix mathematical method for evaluation the DBR mirror for light emitting diode and laser," Journal of Physics: Conference Series, vol. 1535, no. 1, p. 012018, 2020.

[24] K. E. Połczyńska, K. Sobczak, and W. Pacuski, "Distributed Bragg reflector made of CdSe and ZnTe," Superlattices and Microstructures, vol. 139, p. 106422, 2020.

[25] H. Y. Lin et al., "Improvement of light quality by DBR structure in white LED," Optics express, vol. 23, no. 3, pp. A27-A33, 2015.

[26] G. S. Chen, B. Y. Wei, C. T. Lee, and H. Y. Lee, "Monolithic red/green/blue micro-LEDs with HBR and DBR structures," IEEE Photonics Technology Letters, vol. 30, no. 3, pp. 262-265, 2017.

[27] T. Zhi et al., "High Performance Wide Angle DBR Design for Optoelectronic Devices," IEEE Photonics Journal, vol. 13, no. 1, pp. 1-6, 2021.

[28] E. Yablonovitch and T. J. Gmitter, "Photonic Band Structure: The Face-Centered-Cubic Case," Physical Review Letters, vol. 63, no. 18, pp. 1950–1953, 1989.

[29] S. Noda, K. Tomoda, and N. Yamamoto, "Full Three-Dimensional Photonic Bandgap Crystals at Near-Infrared Wavelengths," Science, vol. 289, no. July, pp. 604–607, 2000.

[30] P. Radaelli, "Symmetry in crystallography: understanding the international tables," Oxford University Press, 2011.

[31] E. Kuramochi et al., "Large-scale integration of wavelength-addressable all-optical memories on a photonic crystal chip," Nature Photonics, vol. 8, no. May, pp. 2-9, 2014.

[32] S. G. Johnson and J. D. Joannopoulos, Photonic Crystals: The Road from Theory to Practice, Springer Science & Business Media, 2001.

[33] E. Yablonovitch, "Photonic Crystals: Towards Nanoscale Photonic Devices," Physics Today, vol. 59, no. 8, pp. 54-55, 2006.

[34] P. Radaelli, Symmetry in Crystallography: Understanding the International Tables, vol. 17, Oxford University Press, 2011.

[35] M. Qiu and S. He, "Large complete band gap in two-dimensional photonic crystals with elliptic air holes," Physical Review B, vol. 60, no. 15, pp. 10610.

[36] A. M. Fox, "Quantum optics: an introduction," Oxford University Press, USA, 2006.

[37] G. C. des Francs, J. Barthes, A. Bouhelier, J. C. Weeber, A. Dereux, A. Cuche, and C. Girard, "Plasmonic Purcell factor and coupling efficiency to surface plasmons. Implications for addressing and controlling optical nanosources," Journal of Optics, vol. 18, no. 9, p. 094005, 2016.

[38] H. Iwase, D. Englund, and J. Vučković, "Analysis of the Purcell effect in photonic and plasmonic crystals with losses," Optics express, vol. 18, no. 16, pp. 16546-16560, 2010.

[39] A. Onal, G. O. Eren, R. Melikov, L. Kaya, and S. Nizamoglu, "Quantum Dot Enabled Efficient White LEDs for Wide Color Gamut Displays," Advanced Materials Technologies, vol. 8, no. 9, p. 2201799, 2023.

[40] T. Y. Lee et al., "Ameliorating Uniformity and Color Conversion Efficiency in Quantum Dot-Based Micro-LED Displays through Blue–UV Hybrid Structures," Nanomaterials, vol. 13, no. 14, p. 2099, 2023.

[41] Y. Gu et al., "Investigation on the Optical Properties of Micro-LEDs Based on InGaN Quantum Dots Grown by Molecular Beam Epitaxy," Nanomaterials, vol. 13, no. 8, p. 1346, 2021.

[42] R. Gurjar, C. P. Singh, A. S. Meena, and K. Ghosh, "Effect of Parabolic Quantum Well on Internal Quantum Efficiency of InGaN/GaN based Micro-LED at low current density," in 2022 International Conference on Numerical Simulation of Optoelectronic Devices (NUSOD), pp. 89-90, IEEE, September 2022.

[43] K. Zhang, C. Hu, V. G. Thirupakuzi Vangipuram, K. Kash, and H. Zhao, "Design of InGaN-ZnSnGa2N4 quantum wells for high-efficiency amber light emitting diodes," Journal of Vacuum Science & Technology A, vol. 41, no. 3, 2023.

[44] Z. Liu et al., "Effect of the AlN strain compensation layer on InGaN quantum well red-light-emitting diodes beyond epitaxy," Optics Letters, vol. 47, no. 23, pp. 6229-6232, 2022.

[45] D. Pudis, L. Suslik, J. Skriniarova, J. Kovac, J. Kovac Jr, I. Kubicova, and P. Schaaf, "Effect of 2D photonic structure patterned in the LED surface on emission properties," Applied surface science, vol. 269, pp. 161-165, 2013.

[46] Y. Shimizu, "Laser interference lithography for fabrication of planar scale gratings for optical metrology," Nanomanufacturing and Metrology, vol. 4, no. 1, pp. 3-27, 2021.

[47] J. H. Seo et al., "Nanopatterning by laser interference lithography: applications to optical devices," Journal of nanoscience and nanotechnology, vol. 14, no. 2, pp. 1521-1532, 2014.

[48] H. van Wolferen and L. Abelmann, "Laser interference lithography," in Lithography: Principles, processes and materials, pp. 133-148, 2011.

[49] G. Von Freymann et al., "Three-dimensional nanostructures for photonics," Adv. Funct. Mater., 2010.

[50] M. E. Stewart et al., "Nanostructured plasmonic sensors," Chemical Reviews, 2008.

[51] Q. Luo et al., "Protein Assembly: Versatile Approaches to Construct Highly Ordered Nanostructures," Chemical Reviews, 2016.

[52] M. Albrecht et al., "Magnetic multilayers on nanospheres," Nat. Mater., 2005.

[53] S. Jeon, V. Malyarchuk, J. O. White, and J. A. Rogere, "Optically Fabricated Three Dimensional Nanofluidic Mixers for Microfluidic Devices," Nano Lett., 2005.

[54] I. Byun and J. Kim, "Cost-effective laser interference lithography using a 405 nm AlInGaN semiconductor laser," J. Micromechanics Microengineering, 2010.

[55] J. de Boor, N. Geyer, U. Gösele, and V. Schmidt, "Three-beam interference lithography: upgrading a Lloyd's interferometer for single-exposure hexagonal patterning," Opt. Lett., 2009.

[56] E. M. Park et al., "Investigation of the effects of bottom anti-reflective coating on nanoscale patterns by laser interference lithography," Thin Solid Films, 2011.

[57] H. F. Yang et al., "Simulation and fabrication of nanostructures with laser interference lithography," Laser Physics, 2014.

[58] Q. Xie et al., "Fabrication of nanostructures with laser interference lithography," Journal of alloys and compounds, 2008.

[59] C. Lu and R. H. Lipson, "Interference lithography: a powerful tool for fabricating periodic structures," Laser & Photonics Reviews, 2010.

[60] T. Kondo et al., "Femtosecond laser interference technique with diffractive beam splitter for fabrication of three-dimensional photonic crystals," Appl. Phys. Lett., 2001.

[61] S. Eckhardt et al., "Fabrication of highly efficient transparent metal thin film electrodes using Direct Laser Interference Patterning," 2015.

[62] J. Berger et al., "Direct and High-Throughput Fabrication of Mie-Resonant Metasurfaces via Single-Pulse Laser Interference," ACS Nano, 2020.

[63] J. Lutkenhaus et al., "Digitally tunable holographic lithography using a spatial light modulator as a programmable phase mask," Opt. Express, 2013.

[64] S. Behera, M. Kumar, and J. Joseph, "Submicrometer photonic structure fabrication by phase spatial-light-modulator-based interference lithography," Opt. Lett., 2016.

[65] B. Voisiat et al., "Flexible Microstructuring of Thin Films Using Multi-beam Interference Ablation with Ultrashort Lasers," Journal of Laser Micro/Nanoengineering, 2011.

[66] Y. R. Wang et al., "Direct patterning of periodic semiconductor nanostructures using single-pulse nanosecond laser interference," Optics Express, 2020.

[67] C. Tan et al., "Ordered nanostructures written directly by laser interference," Nanotechnology, 2008.

[68] A. Rodríguez et al., "Laser interference lithography for nanoscale structuring of materials: From laboratory to industry," Microelectronic Engineering, 2009.

[69] Z. Xu et al., "Periodic antireflection surface structure fabricated on silicon by four-beam laser interference lithography," Journal of Laser Applications, 2014.

[70] M. Ellman et al., "High-power laser interference lithography process on photoresist: Effect of laser fluence and polarisation," Applied Surface Science, 2009.

[71] D. Wang et al., "Direct modification of silicon surface by nanosecond laser interference lithography," Applied Surface Science, 2013.

[72] A. Rodriguez, M. Echeverría, M. Ellman, N. Perez, Y. K. Verevkin, C. S. Peng, et al., "Laser interference lithography for nanoscale structuring of materials: From laboratory to industry," Microelectronic Engineering, vol. 86, no. 4-6, pp. 937-940, 2009.

[73] J. Xu, Z. Wang, Z. Zhang, D. Wang, and Z. Weng, "Fabrication of moth-eye structures on silicon by direct six-beam laser interference lithography," Journal of Applied Physics, vol. 115, no. 20.

[74] J. Xu, Z. Wang, Z. Zhang, D. Wang, and Z. Weng, "Effective intensity distributions used for direct laser interference exposure," RSC Advances, vol. 5, no. 68, pp. 54947-54951, 2015.

[75] S. Alamri and A. F. Lasagni, "Development of a general model for direct laser interference patterning of polymers," Opt. Express, 2017, doi: 10.1364/oe.25.009603.

[76] M. Bieda, M. Siebold, and A. F. Lasagni, "Fabrication of sub-micron surface structures on copper, stainless steel and titanium using picosecond laser interference patterning," Appl. Surf. Sci., 2016, doi: 10.1016/j.apsusc.2016.06.100.

[77] J. Berger, M. Grosse Holthaus, N. Pistillo, T. Roch, K. Rezwan, and A. F. Lasagni, "Ultraviolet laser interference patterning of hydroxyapatite surfaces," Appl. Surf. Sci., 2011, doi: 10.1016/j.apsusc.2010.10.120.

[78] Z. Zhang, Z. Wang, D. Wang, and Y. J. Ding, "Periodic antireflection surface structure fabricated on silicon by four-beam laser interference lithography," Journal of Laser Applications, vol. 26, no. 1.

[79] M. Ellman, A. Rodríguez, N. Pérez, M. Echeverria, Y. K. Verevkin, C. S. Peng, et al., "High-power laser interference lithography process on photoresist: Effect of laser fluence and polarization," Applied Surface Science, vol. 255, no. 10, pp. 5537-5541, 2009.

[80] D. Wang, Z. Wang, Z. Zhang, Y. Yue, D. Li, and C. Maple, "Effects of polarization on four-beam laser interference lithography," Applied physics letters, vol. 102, no. 8.

[81] C. Tan, C. S. Peng, V. N. Petryakov, Y. K. Verevkin, J. Zhang, Z. Wang, et al., "Line defects in two-dimensional four-beam interference patterns," New Journal of physics, vol. 10, no. 2, p. 023023, 2008.

[82] D. Wang, Z. Wang, Z. Zhang, Y. Yue, D. Li, and C. Maple, "Direct modification of silicon surface by nanosecond laser interference lithography," Applied Surface Science, vol. 282, pp. 67-72, 2013.

Chapter 3

Experimental techniques

3.1 Fabrication Equipment

This section includes the fabrication equipment used for pattern transfer, etching, and deposition methods to create patterns on samples.

3.1.1 Photolithography Equipment

The photolithography equipment plays an essential role in semiconductor manufacturing. It facilitates the transfer of patterns to wafers, which is vital for producing semiconductor devices. This process involves wafer cleaning, photoresist coating, exposure, and development.

Wafer Cleaning

Wafer cleaning is a critical process in semiconductor fabrication to ensure that the wafers are free from contaminants, particles, and residues before proceeding with subsequent manufacturing steps. In our work, the cleaning process involves three steps: first, a solvent cleaning stage utilizing n-butyl acetate (nBA), acetone, and isopropyl alcohol (IPA); second,

rinsing the wafer with deionized water to eliminate solvent residues; third, using clean nitrogen to blow-dry the wafer and subsequently applying a de-moisturizing step through hot plate baking at 100°C to prevent water stains.

Photoresist Coating

Figure 3.1 shows the image of the Electronic Micro Systems Spin Coater Model-4000 which is a specialized device used in semiconductor fabrication and microfabrication processes to evenly coat thin films or layers of liquids, such as photoresists onto the surface of a substrate. The spin coater operates by rapidly spinning the substrate, causing the liquid material to spread outwards due to centrifugal force, resulting in a uniform and controlled layer thickness [1]. In some of our processes, we utilize the Electronic Micro Systems Spin Coater Model-4000 to apply SPR-350 photoresist coating, creating a uniform layer of approximately 1 μm thickness. This is achieved by spinning at 4000 RPM for 30 seconds. Following this, the photoresist is solidified on the wafer's surface through a subsequent soft-bake process.

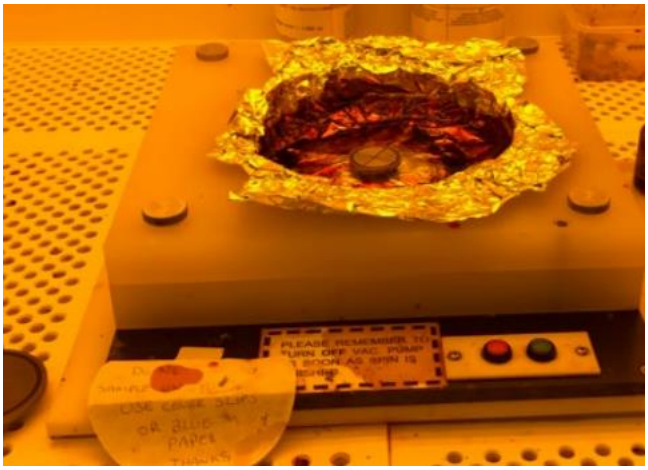

Figure 3.1 Electronic Micro Systems Spin Coater Model-4000.

Exposure

Exposure is a fundamental step in semiconductor photolithography, a critical process in semiconductor manufacturing that involves transferring intricate circuit patterns onto a photoresist. During exposure, a photomask—containing the desired circuit pattern—is positioned over the wafer's photoresist-coated surface. Light, often ultraviolet (UV) or deep ultraviolet (DUV), is directed through the mask onto the wafer, initiating a photochemical reaction in the photoresist that alters its solubility properties [2].

In this study, the Karl Suss MJB3 UV400 Mask Aligner, illustrated in Figure 3.2, is utilized for priming a structured resist film. The procedure involves placing the sample, covered in coated photoresist, onto the aligner's sample holder. A photomask, composed of a glass or quartz plate with a patterned chromium coating, makes contact with the sample. This allows UV light to pass through the transparent sections, exposing the resist film, while blocking light with the opaque segments. As a result, a one-to-one replication of the photomask pattern is imprinted onto the resist film. The chosen SPR-350 Photoresist, categorized as a positive type, contains light-sensitive polymers or polymer precursors dissolved in an organic solvent. To prevent premature reactions between the photoresist and short-wavelength emissions, this entire process is conducted within a yellow room equipped with a light filter. The UV lamp of the Karl Suss MJB3 UV400 Mask Aligner emits light at 405 nm, boasting a print resolution of 0.8 μm under optimal conditions. Consequently, exposure to UV light initiates a photochemical reaction in the photoresist, resulting in distinct outcomes based on the resist type. In the case of positive-type photoresist, exposure decomposes and increases solubility, whereas negative-type resist is polymerized or cross-linked, forming a hardened coating resistant to the developer solution. To maintain precise focus and pattern resolution, meticulous control of the distance between the photomask and wafer surface is paramount.

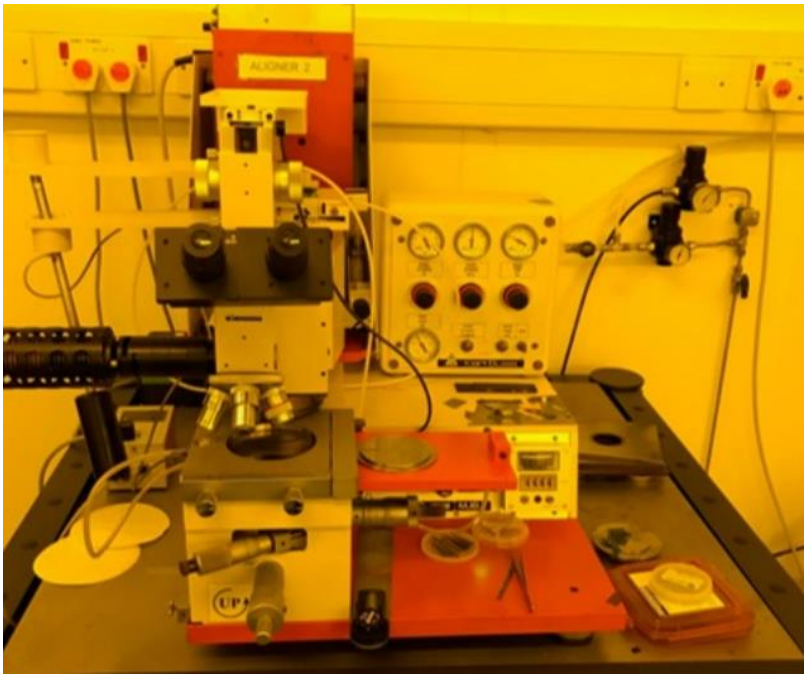

Figure 3.2 Karl Suss MJB3 UV400 Mask Aligner

Development

Developing follows the exposure step and is essential for revealing the desired pattern by selectively removing either the exposed or unexposed areas of the photoresist, depending on whether a positive or negative photoresist is used. In the case of positive photoresist, the exposed areas become more soluble due to the photochemical reaction triggered by light exposure. The developer solution is applied to the wafer. The soluble portions of the photoresist dissolve in the developer, leaving behind the desired pattern of resist material on the wafer. For negative photoresists, the exposed areas become less soluble, making them resistant to the developer solution. When the developer solution is applied, it selectively removes the unexposed regions, leaving behind the pattern of hardened resist on the wafer. The result is the inverse of the desired pattern. In addition, developing time, temperature, and the concentration of the developer solution are crucial parameters that influence the effectiveness of the developing process. Proper control of these parameters ensures that the pattern transfer is accurate, reproducible, and of high quality. The developer solution

effectively washes away the target regions, creating the pattern that will guide subsequent fabrication steps such as etching or deposition. After the developing step, the wafer is rinsed with deionized water to remove any remaining developer solution and dissolved photoresist.

Plasma Asher

Plasma ashing is a critical step in the photolithography process used to remove the photoresist material from a semiconductor wafer after the desired pattern has been transferred through exposure and development. The plasma asher employs a plasma, which is a highly energized and ionized gas, to chemically break down and remove the photoresist material from the wafer's surface. Plasma ashing offers advantages such as high selectivity (removing photoresist while leaving underlying materials intact), controlled process conditions, and efficiency in removing tough residues. Different types of ashers and process conditions may be used depending on the specific photoresist and wafer characteristics. In our works, we use PVA TEPLA Plasma Asher as shown in Figure 3.3. Normally select 1min 0_2 gas. The ashing process is essential because after exposure and development, the photoresist material that has not been dissolved by the developer solution needs to be removed to expose the underlying layers for subsequent processing, such as etching, deposition, or implantation.

Figure 3.3 PVA TEPLA Plasma Asher

3.1.2 Deposition Equipment

Plasma-Enhanced Chemical Vapor Deposition (PECVD)

PECVD is a process that uses a combination of chemical reactions and plasma to deposit thin films onto a substrate [3]. In PECVD equipment, reactive gases are introduced into a vacuum chamber, and a plasma is formed using RF or microwave energy. This allows the controlled deposition of materials such as silicon dioxide (SiO_2), and silicon nitride (Si_3N_4).

In this study, the SiO_2 film deposition is carried out using the Plasma-Therm 790 series PECVD system, as depicted in Figure 3.4. The sample stage is heated to 300°C, while the sidewall is maintained at 60°C. The deposition process employs SiH_4, NH_3, and N_2 as reactant gases, flowing at rates of 160 sccm, 900 sccm, and 240 sccm, respectively. With a reactor pressure of 900 mTorr and an RF power of 25W, the deposition rate averages around 40 nm/min.

Figure 3.4 Plasma-Therm 790 series PECVD system

Thermal Evaporator

A thermal evaporator is a specialized deposition tool used to deposit thin films of metals onto substrates through the process of thermal evaporation. In this work, an Edwards E306A thermal evaporator is employed (shown in Figure 3.5) to deposit metals onto semiconductor devices, specifically for creating n and p-contacts in LEDs.

Metals are positioned within a tungsten coil, which is then situated about 12 cm above the sample to guard against any possible harm from high temperatures. The rate of metal deposition is tracked using a quartz crystal monitor (QCM), with the sample placed adjacent to the QCM. After the chamber's vacuum reaches approximately 10^{-6} Torr, metals are melted and evaporated by sending a significant current, on the order of tens of Amps, through the tungsten coil.

Figure 3.5 Edwards E306A thermal evaporator

3.1.3 Etching Equipment

Reactive-Ion Etching

Reactive ion etching (RIE) is a technique that uses radiofrequency (RF) discharge-excited species, such as radicals and ions, to etch substrates or thin films within a low-pressure chamber [4]. In this study, the Plasma-Therm Shuttlelock RIE system (illustrated in Figure 3.6) is utilized for executing selective area etching on a SiO_2 mask. CHF_3 serves as the reactant gas, generating plasmas through a 13.56 MHz RF power set at 150 W. The etching procedure is carried out at a reduced pressure of 35 mTorr, yielding an approximate etching rate of 40 nm/min. Furthermore, the introduction of sidewall passivation augments the etching's anisotropy by depositing carbon polymers from the reactant gases onto the SiO_2 sidewall, thereby hindering chemical reactions. Nevertheless, an excessive accumulation of such sidewall polymeric passivation can decrease the etching rate, leading to the formation of oxide residues resembling grass, resulting in uneven etching patterns. To counteract this, a flow rate of 5 sccm O_2 is introduced to eliminate the polymers during the etching process. After the RIE etching step, the SiO_2 remains covered by the photoresist, while the exposed area undergoes etching.

Figure 3.6 Plasma-Therm Shuttlelock Series RIE.

Inductively Coupled plasma (ICP)

ICP etching and RIE are plasma etching techniques used in microfabrication [5]. ICP generates plasma using an RF coil, allowing for high-density plasma at lower pressures and more controlled ion directionality, leading to smoother, vertical etching profiles [6]. RIE generates plasma directly above the wafer with capacitively coupled plates. It offers versatility and is widely used in semiconductor etching but has less control over ion directionality, potentially leading to varied etching profiles.

In this research, the Oxford Instruments PlasmalabSystem 100 ICP-RIE system, depicted in Figure 3.7, is employed. Reactive gases are introduced into an ICP chamber, where ions formed within the plasma are used to etch through GaAs layers. The GaAs etching process use $SiCl_4$ gas, known for its high anisotropy and rapid etching rate. Software control enables the monitoring and regulation of RF power and gas flow. Specifically, for GaAs etching, the ICP power is set to 250W, while the etching power is conservatively maintained at 100W. A $SiCl_4$ gas flow rate of 5 sccm is employed. This recipe delivers an etching rate of approximately 400nm/min.

Figure 3.7 the Oxford Instruments PlasmalabSystem 100 ICP-RIE system

Wet Chemical etching

Chemical wet etching is a fundamental process used in semiconductor fabrication to selectively remove specific materials from the surface of a substrate using chemical reactions. Unlike dry etching methods, which utilize plasma-based techniques, wet etching involves immersing the substrate in a liquid chemical solution, known as an etchant, to dissolve or react with the material being removed [7].

In this research, our objective is to perform etching on a GaAs-based mesa diode. The sample is subjected to agitation within a commonly referred-to chemical etchant known as "1:1:1 etch." This etchant comprises one part Hydrobromic acid, one part Acetic acid, and one part Potassium Dichromate solution. The etch rate for this solution is approximately 2 μm/min, and the etching process is isotropic. The etching action penetrates entirely through the active region and extends into the n+ doped region, reaching a depth of approximately 1 μm. To accomplish this, an etch time of around 30 seconds is employed, resulting in an etch depth of approximately 1 μm. Considering a resist thickness of 1 μm, this approach achieves the desired mesa etch configuration.

3.2 Morphological Characterization Equipment

Morphological characterization is essential in semiconductor device fabrication to ensure that devices are manufactured accurately and consistently. As semiconductor devices continue to shrink in size, the need for precision characterization tools becomes even more crucial.

3.2.1 Dektak Profilometer

The DEKTAK 150 shown in Figure 3.8 employs a stylus-based measurement technique to scan across a sample's surface, recording variations in height [8][9]. the DEKTAK 150 is more suitable for larger-scale surface profiling (micrometer level). This provides precise data about the 1D surface profile and helps ensure the uniformity and consistency of thin films and layers. By measuring the depth of features and variations on the sample's surface, the DEKTAK 150 can determine the thickness of thin films and layers used in semiconductor devices.

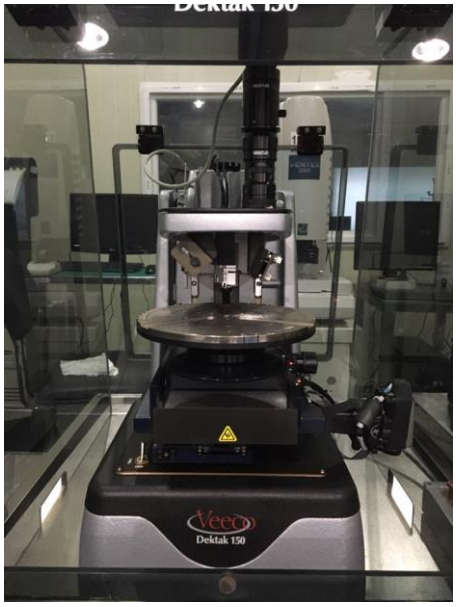

Figure 3.8 DEKTAK 150

3.2.2 Scanning Electron Microscope (SEM)

Figure 3.9 depicts the Raith SEM. This SEM offers superior resolution and magnification compared to traditional optical microscope systems [10]. Within the SEM, an electron gun releases electrons which are then accelerated by voltages reaching up to 10kV. To prevent scattering, SEM operations require a high vacuum environment, typically around 5×10^{-5} mBar.

Following this, electrons are directed by a condenser lens and subsequently move through an aperture system. Deflection coils then focus the electron beam onto the sample, producing backscattered and secondary electrons [11]. These emitted electrons are captured by two detectors and, after computer processing, are converted into images.

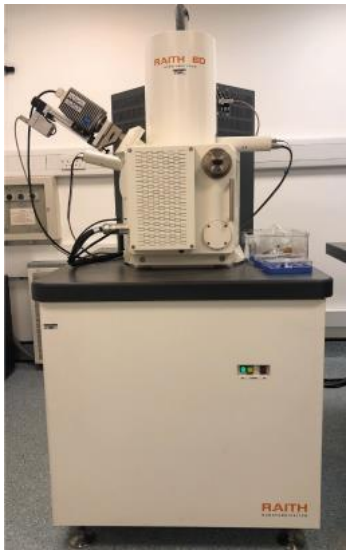

Figure 3.9 Raith SEM

3.2.3 Atomic Force Microscopy (AFM)

Atomic Force Microscopy (AFM) and DEKTAK Profilometer are both surface characterization tools used in semiconductor device fabrication. However, they employ different principles and offer distinct capabilities for analyzing surface features and properties. AFM is adept at high-resolution imaging, offering atomic-scale surface topography details, while the DEKTAK Profilometer is suitable for larger-scale surface profiling. AFM is ideal for nano-focused research, whereas the DEKTAK Profilometer suits industries seeking accurate measurements of step heights and surface profiles [12].

The heart of the AFM is the probe, which is mounted at the end of a tiny cantilever shown in Figure 3.10 (a). The probe is usually a sharp tip made of a material like silicon or silicon nitride.

The cantilever is flexible supports the probe and can deflect as interactions occur. The sample is mounted on a stage that can move in two dimensions (X, Y). The AFM probe is positioned above the sample, and the cantilever is lowered toward the surface which can move in Z dimension. Due to the van der Waals forces, interactions take place between the atoms or molecules on the probe and those on the sample's surface when the probe gets closer to the sample's surface. The deflection data from the cantilever is converted into a three-dimensional image of the surface. Brighter areas in the image represent higher points, while darker areas represent lower points. AFM can operate in various modes beyond simple contact imaging. Tapping mode, non-contact mode, and dynamic mode are examples of specialized modes that provide additional information about surface properties [13]. In our works, the dynamic mode is our customary choice. Illustratively, Figure 3.10 (b) showcases the image of the FSM Nanoview-1000 atomic force microscope.

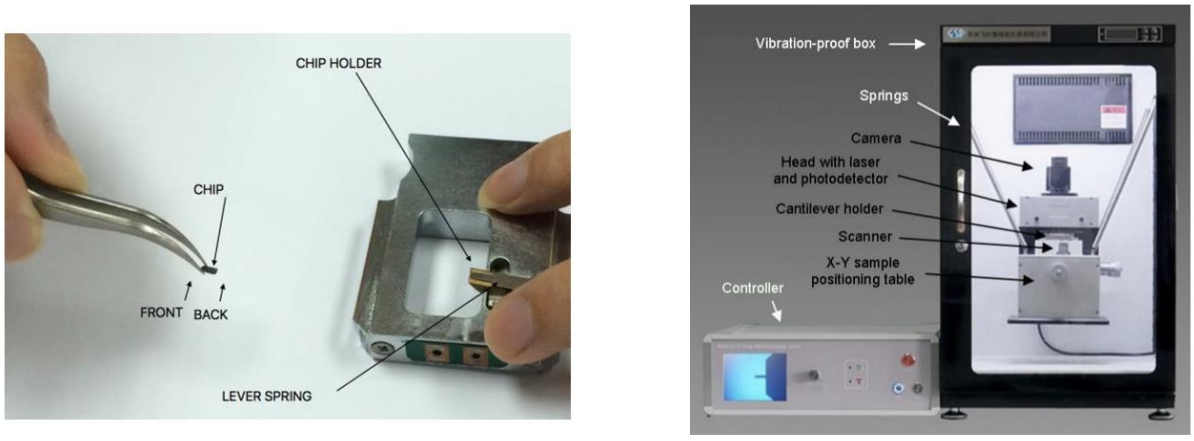

(a) (b)

Figure 3.10 (a) Mount the cantilever. (b) FSM Nanoview-1000 atomic force microscope.

3.3 Optical Characterization Equipment

Optical characterization equipment plays a critical role in semiconductor fabrication processes. These tools are used to measure and analyze various optical properties of

semiconductor materials and devices. These properties provide insights into the quality, performance, and functionality of the fabricated components. The information obtained from these techniques helps engineers and researchers ensure the quality and performance of semiconductor devices (the band structures, composition, emission energy, and more), optimize fabrication processes and develop new technologies. This section introduces some commonly used optical characterization techniques and equipment in semiconductor fabrication in this works.

3.3.1 Micro-Photoluminescence

Micro-photoluminescence (μ-PL) is particularly valuable for studying materials with spatial variations in optical properties and for analyzing individual nanostructures [14]. Figure 3.11 (a) shows a schematic diagram of the μ-PL system used in this experiment. focused laser beam is used to illuminate a 2 μm spot of the sample which is in the high vacuum cryostat chamber. Using air cooling and a mechanical pump, our cryostat can theoretically achieve approximately 55K, managed through the Lakeshore temperature controller shown in Figure 3.11 (b). This setup facilitates optical measurements across various temperature ranges. The energy of the laser is typically higher than the bandgap energy of the material under investigation. This energy is absorbed by the material, exciting its electrons to higher energy levels. Laser power can be managed through connected computer software, offering a tunable power span from 1mW to 20mW. Moreover, the overall laser power can be adjusted by substituting the ND Filter positioned in front of the laser shown in Figure 3.11 (b), facilitating power-dependent PL. After excitation, the electrons relax back to their lower energy levels. During this relaxation process, photons are emitted with energies corresponding to the energy levels of the material. This emitted light is known as photoluminescence which we discussed in Chapter 2. The emitted photoluminescence is collected and analyzed using the Horiba FHR1000 spectrometer, featuring a 1 m focal length and providing a spectral resolution of 0.01 nm with 10 μm slits, as illustrated in Figure 3.11

(c). The spectrometer separates the emitted light into distinct wavelengths, facilitating the assessment of both the energy and intensity of emitted photons, which are subsequently captured by a cooled InGaAs or Si detector.

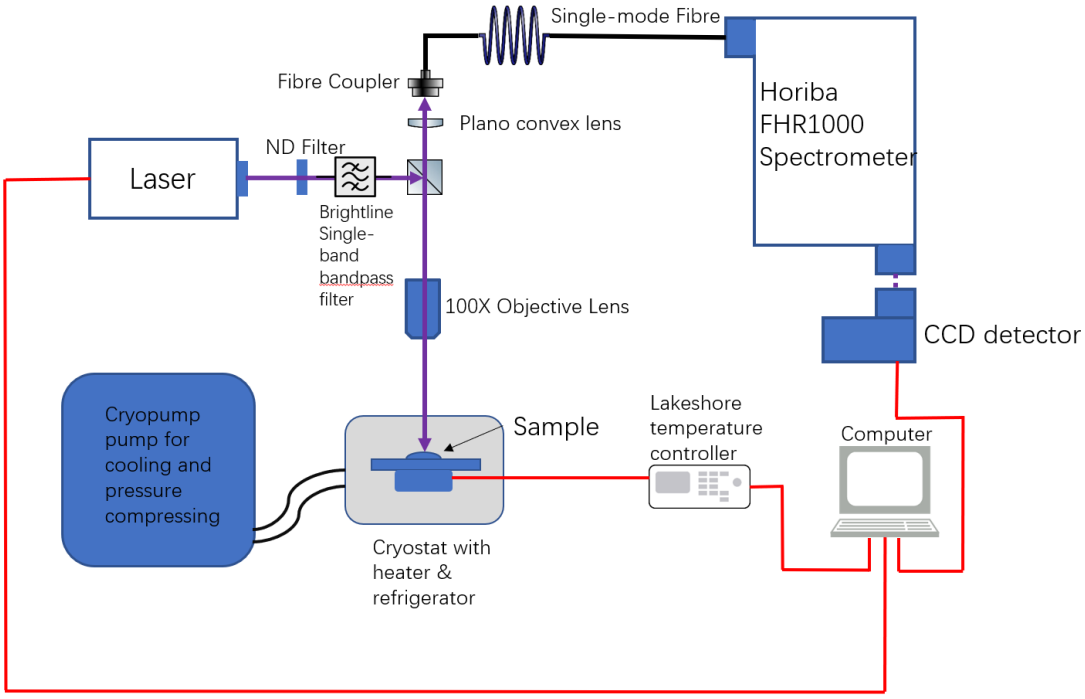

(a)

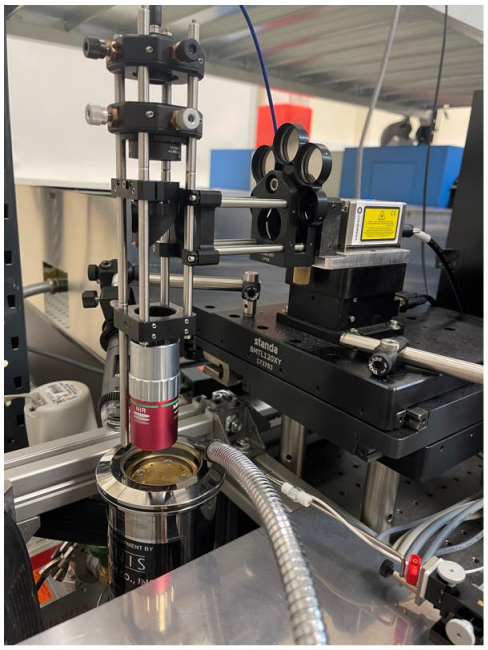

(b)

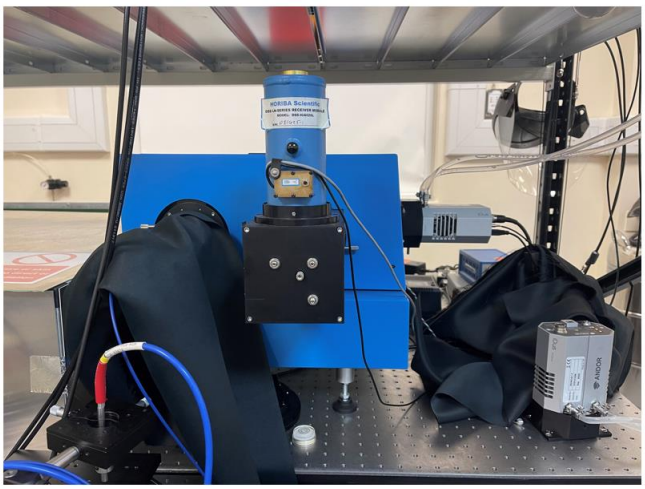

(c)

Figure 3.11 (a) schematic diagram of the μ-PL system. (b) cryostat chamber. (c) Horiba FHR1000 spectrometer and CCD detectors.

3.3.2 Micro-Electroluminescence

Micro-Electroluminescence (μ-EL) is a technique used to study the light emission properties of microscale or nanoscale semiconductor devices when an electric current is passed through them [15]. As shown in Figure 3.12 (a), Electrical contacts are carefully attached to the sample. These contacts provide a pathway for the electric current to flow through the semiconductor structure. A voltage source shown in Figure 3.12 (b) is connected to the electrical contacts. When the voltage is applied, The electric current flows through the semiconductor structure. This current drives the movement of electrons and holes within the material. As the electric current passes through the semiconductor structure, electrons and holes are injected into the material. When electrons recombine with holes at the junction or within the material, they release energy in the form of photons. This energy corresponds to the bandgap energy of the material, determining the emitted light's wavelength. The recombination of electrons and holes leads to the emission of light. This emitted light is the electroluminescence which is discussed in Chapter 2. The wavelength and intensity of the emitted light provide information about the material's properties, energy levels, and the efficiency of the recombination process. The emitted light is collected and analyzed using the same optical systems illustrated in Figure 3.11 (c).

(a) (b)

Figure 3.12 (a) Electrical contacts. (b) Keithley 2401 sourcemeter.

3.3.3 Reflectance Measurement Equipment

For the reflectance measurement, we use the ASEQ instruments high-resolution spectrometer, seamlessly integrated with an optical microscope, and equipped with visible illumination spanning from 450 to 700 nm, as illustrated in Figure 3.13. This measurement technique enables the acquisition of material reflectance data.

To ensure precision in our measurements, we meticulously control the sample's positioning using translation stages. Furthermore, we employ aperture control within the microscope to confine the illumination to specific patterned regions. This setup allows us to capture the reflected signal across a broad angular range by utilizing a high numerical aperture, which can reach up to 1. In our setup, we employ a 50X microscope objective with an NA of 0.56, which encompasses a half-cone angle of 33.3°.

(a) (b)

Figure 3.13 (a) Optical microscope. (b) The ASEQ instruments high-resolution spectrometer.

3.4 Laser Interference Lithography system

In this investigation, Figure 3.14 illustrates the utilization of a laser interference lithography system. This system incorporates a flash-lamp pumped Nd: YAG laser characterized by a wavelength of 355 nm, a frequency of 5 Hz, a pulse duration of 7 ns, and a Gaussian beam diameter of 5 mm as the laser interference source. To achieve this, the laser beam is divided into four equal beams through three beam splitters, where one of the beams is intentionally blocked. Each of these beams traverses a half-wave plate and a Glan-laser polarizer to manage both pulse energy and polarization states. Subsequently, these three beams are recombined on the surface of the wafer. For the precise generation of periodic interference patterns, the incident angles of the three beams are carefully adjusted to approximately 30°, while the azimuth angles remain fixed at 0°, 90°, and 180°.

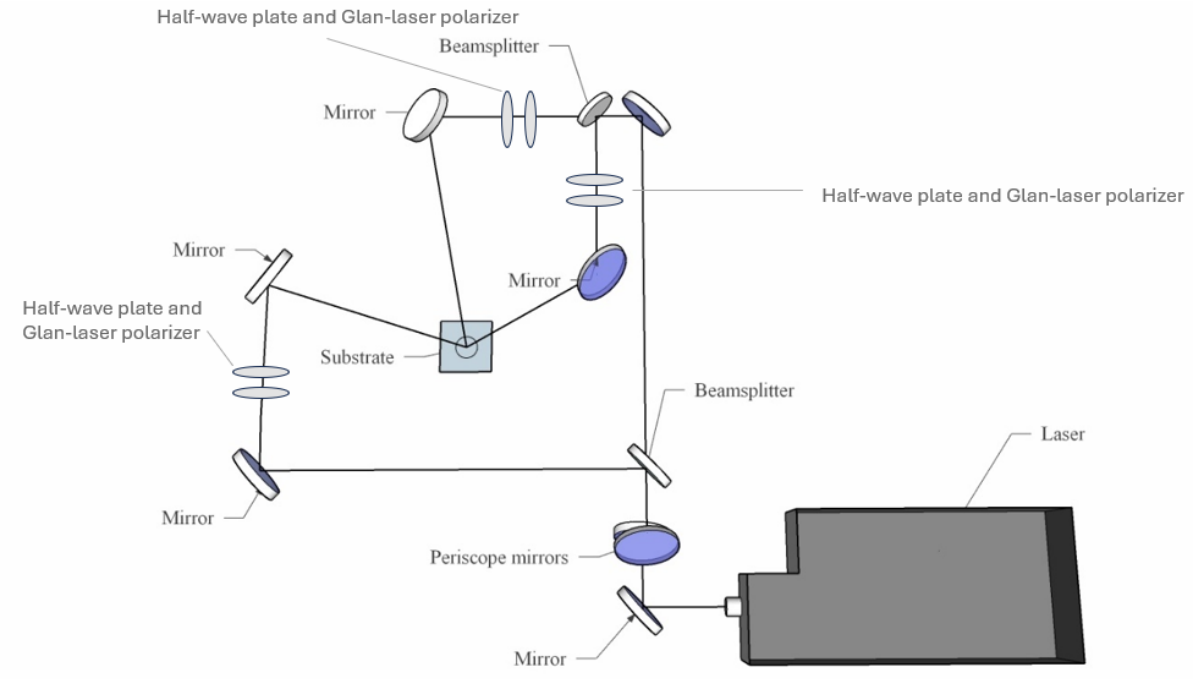

Figure 3.14 (a) schematic diagram of the three beams laser interference lithography system.

3.4.1 Moiré pattern

A moiré pattern in Multi-beams LIL is a visual phenomenon when two or more sets of fine patterns overlay with slight angles or differences in spacing, creating a larger, visible pattern.

In the simplest terms, when using a two-beam setup in LIL, the interference pattern is straightforward—the beams interfere directly with each other to form a regular pattern of high and low intensity that can be used for lithography. This pattern is predictable and doesn't produce complex moiré patterns because there's only one set of interactions to consider.

When you move to a three-beam setup, the interaction still tends to be relatively straightforward, assuming the beams are designed to interfere in a controlled manner. Each pair of beams creates an interference pattern, and the third beam can be used to modulate the result, enhancing or suppressing certain features. The complexity doesn't inherently lead to moiré patterns because the setup and angles can be carefully controlled to ensure that the resulting superposition of patterns is still regular and useful for lithography purposes.

However, as you increase the number of beams beyond three, managing these interactions becomes exponentially more complex. Each beam interacts with every other beam, leading to a multitude of pairwise interference patterns that overlay. Without extremely precise control over the angle, phase, and spacing of each beam, this can result in unintentional and often undesirable complex moiré patterns. These patterns are a result of overlapping interference patterns that no longer align in a simple, predictable manner. The complexity and unpredictability increase with each additional beam, making it challenging to use such setups for applications like lithography, where precision and predictability are crucial. To avoid the interference of Moore's pattern and to get our desired pattern, three-beam LIL was used in this experiment.

3.5 Molecular beam epitaxy

As shown in Figure 3.15, a modified solid-source MBE system (Dr. Eberl MBE Komponenten GmbH, Germany) was utilized to grow III-V materials for this dissertation. The system consists of three main chambers: the growth chamber (main chamber), the buffer chamber, and the load lock chamber. These chambers are separated by gate valves. The growth chamber is equipped with Group III effusion cells for In, Al, and Ga, n:Si and p:Be dopant cells, and valved-cracker cells for As and Sb from Group V. The system achieves base pressures much lower than 10^{-10} mbar using a cryopump and a Ti sublimation pump. Cell shutters controlled by an automated computer system are installed in front of each cell to interrupt the beam fluxes. Thermocouples in contact with the crucible provide temperature measurements of the effusion cells. The beam equivalent pressure can be measured using the beam flux monitor, which is an unshielded Bayard-Alpert style ionization gauge that can be positioned directly below the substrate. All GaAs samples in this dissertation were prepared as follows: Epi-ready 2-inch wafers or quarter wafers were loaded into the load lock chamber and pumped down by a turbo pump until the pressure reached approximately 1×10^{-8} mbar. The wafer was then transferred to the buffer chamber using a transfer rod and degassed on a heater stage at 300 °C for at least 30 minutes. Subsequently, the wafer was moved to the main chamber, where the substrate temperature was raised to around 650 °C to remove the native oxide on GaAs. An arsenic flux was provided at temperatures above 400 °C to prevent substrate dissociation. Growth then proceeded to establish a GaAs buffer layer, which smooths the interface and buries any interfacial contamination. The quality of the growth was confirmed by observing strong surface reconstructions in the RHEED pattern.

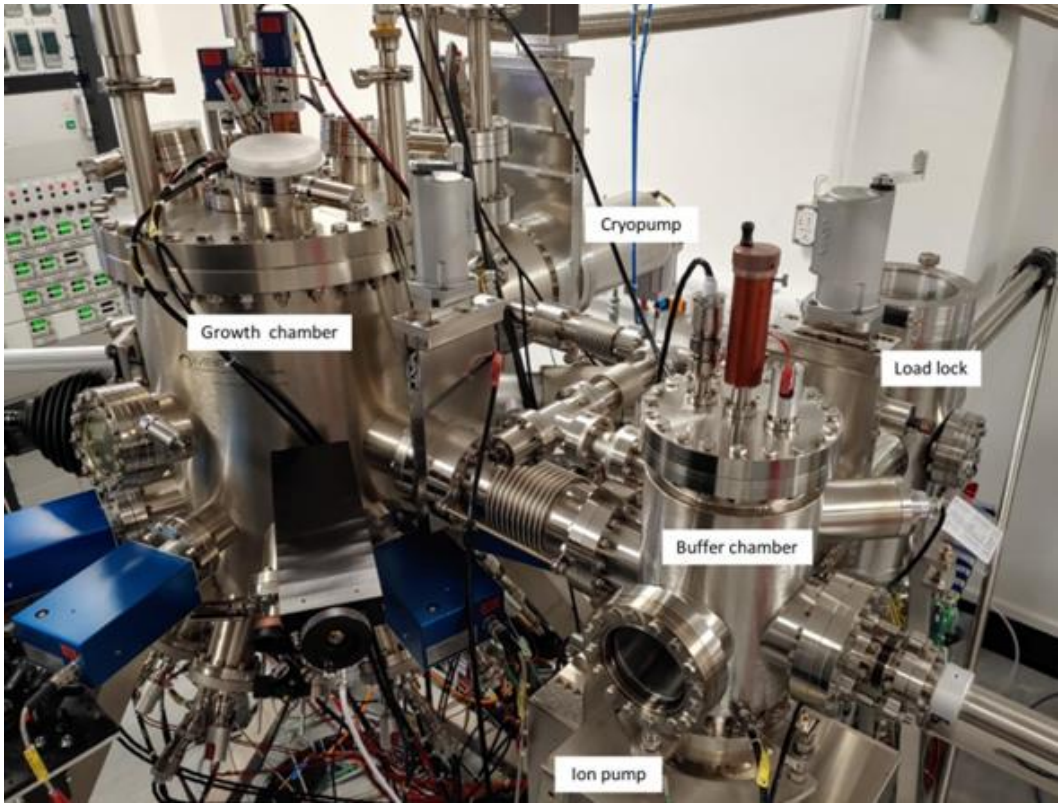

Figure 3.15 Photograph of the MBE system.

3.5.1 Integration of direct laser interference patterning with the molecular beam epitaxy system

This section details the laser interference setup designed for the in situ growth of semiconductor nanostructures using MBE. A four-beam DLIP setup was constructed, similar to our previous ex situ LIL setup. Given that the MBE system consists of a large vacuum chamber where optics cannot be placed, the laser interference setup required a specialized design.

The laser is positioned on an optical table adjacent to the MBE chamber, with a set of optical components arranged on three sub-optical breadboards around the MBE system. The output

light beam is first redirected to an optical sub-frame using a beam steering mirror. A periscope assembly aligns the laser beam height to match that of the MBE optical viewports. Three 50:50 beam splitters are used to divide the beam into four sub-beams. These four sub-beams are then directed into the MBE chamber through four symmetrically positioned UV anti-reflection coated optical viewports at 0°, 90°, 180°, and 270°. The angle of incidence to the substrate is fixed at 58° due to the position of the viewports, which cannot be altered once welded. The optical path in the setup measures approximately 3.5-4 meters. Figure 3.16 (a-c) shows photographs of some of the optical setups around the MBE chamber.

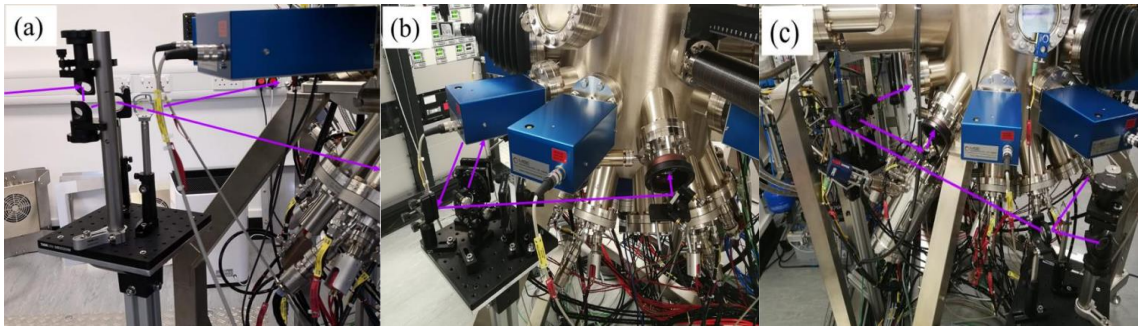

Figure 3.16 (a-c) Photographs of part of the DLIP setup around the MBE chamber.

3.5.2 Experimental details

The GaAs samples for DLIP were prepared as follows: First, native oxide desorption was performed at a substrate temperature (Ts) of 620 °C. Following this, a 1000 nm-thick GaAs buffer layer was grown at Ts = 600 °C to smooth the surface. Subsequently, Ts was lowered to 500 °C for the growth of an additional 500 nm GaAs epilayer. This method typically results in a surface that is almost atomically flat, with occasional meandering terraces, as observed by AFM. After growth, the wafer was immediately irradiated by the in situ single-pulse DLIP inside the MBE chamber. A stabilized arsenic flux was supplied during the growth. This process completes the pre-patterning, making the sample ready for the next step of epitaxial growth (QDs or QRs).

3.5.3 The mechanisms during pulsed DLIP of semiconductor surfaces

Several mechanisms may occur during the interaction of nanosecond pulsed laser interference with materials, resulting in different surface morphologies. Mass transport is the predominant mechanism. Photothermal simulations indicate that a 2D thermal gradient is generated on the GaAs surface due to the interference patterning. When the thermal energy exceeds the atom diffusion barrier energy, surface atoms migrate from the interference maxima (hot regions) towards the minima (cold regions). Figure 3.17(a) shows a schematic diagram of atom migration driven by a thermal gradient.

Another well-known mechanism during laser-matter interaction is the Marangoni effect, commonly observed in laser patterning on metals [16-19]. The schematic diagram of Marangoni flow is presented in Figure3.17(b). If the material surface reaches its melting point under laser irradiation, the localized molten material may move outward driven by a thermocapillary force or inward due to a chemicapillary force [18]. The resulting structure is determined by the competition between these two flows.

In addition to laser melting, thermal evaporation of the material is also possible. If the surface temperature exceeds a certain threshold under laser irradiation, such as the congruent evaporation temperature of GaAs (over 625 °C) [20][21], GaAs decomposition occurs, where arsenic atoms evaporate, leaving free Ga atoms on the surface, which can form Ga-rich metallic droplets [20]. It is well-known that Ga droplets can self-etch the surface to create nanoholes, with surface mass transport occurring during this process [22]. Figure 3.17(c) describes the schematic processes of Ga droplets etching and hole formation.

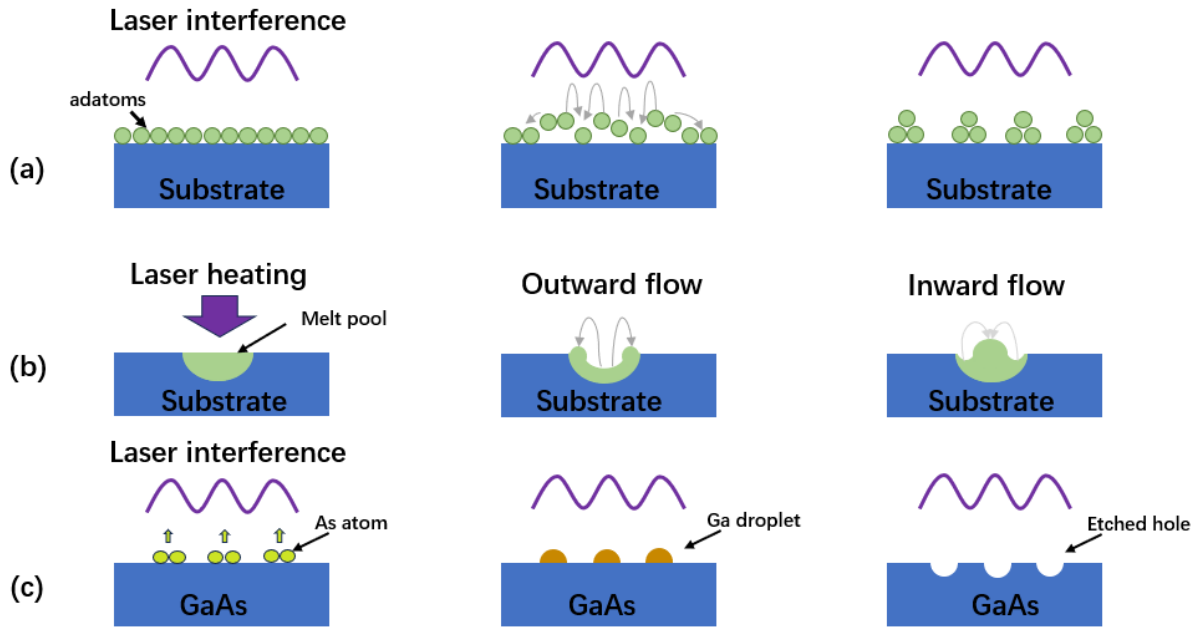

Figure 3.17 Schematic diagrams of (a) surface adatom migration driven by DLIP thermal gradients, (b) laser-induced Marangoni effect, and (c) DLIP-induced Ga droplet etching process.

3.6 Finite-Difference Time-Domain (FDTD)

The FDTD technique is a computational method used to solve Maxwell's equations for electromagnetic wave propagation. This method is widely used in the fields of optics, photonics, and electromagnetic research. It discretizes both space and time to simulate how electromagnetic fields evolve over time. The computational domain is divided into a grid of small cells (spatial discretization), and time is divided into small increments (temporal discretization). The technique solves Maxwell's curl equations, which describe how electric and magnetic fields propagate and interact. Using finite differences, the continuous partial differential equations are converted into difference equations, and the fields are updated at each time step using these discrete equations. Appropriate boundary conditions (Perfectly Matched Layers or PML) are applied to absorb outgoing waves and minimize reflections that could affect the simulation accuracy. Material properties, such as permittivity and permeability, are included in the simulation to account for different media. An

electromagnetic source is introduced into the computational domain to initiate the simulation, and the electric and magnetic fields are updated iteratively over time until the desired end time is reached or the fields have sufficiently evolved.

For simulation experiments, testing and benchmarking FDTD simulations is crucial to ensure reasonable and accurate results. First, we need to ensure that the simulation settings are correct. One important aspect is energy conservation: the total energy in the system, including absorption, reflection, transmission, and dissipation, must be conserved throughout the simulation. Additionally, boundary condition checks are necessary to verify that the boundary conditions (e.g., Perfectly Matched Layers, PML) are effectively absorbing outgoing waves without causing significant reflections back into the computational domain. Mode analysis should be performed for waveguides or resonators to ensure that the simulated modes match the theoretical or expected modes. Convergence tests are also essential; by refining the spatial and temporal discretization, the results should converge to a stable solution as the grid is refined. Secondly, simulation results should be compared with known analytical solutions for simple problems such as plane wave propagation, reflection, and transmission at interfaces. Comparing the simulation results with literature or one's own experimental data is also essential to confirm the validity of the simulation in a real-world scenario.

Reference

[1] R. Das and A. Chanda, "Fabrication and properties of spin-coated polymer films," in Nano-size polymers: Preparation, properties, applications, pp. 283-306, 2016.

[2] L. S. Melvin, "Optical and EUV lithography: A modeling perspective," 2021, pp. 85-86.

[3] A. W. Weimer, Ed., "Carbide, nitride and boride materials synthesis and processing," Springer Science & Business Media, 2012.

[4] D. Li, Ed., "Encyclopedia of microfluidics and nanofluidics," Springer Science & Business Media, 2008.

[5] K. Nojiri, "Dry etching technology for semiconductors," pp. 1-116, Springer International Publishing, 2015.

[6] R. J. Shul et al., "Inductively coupled plasma etching of GaN," Applied physics letters, vol. 69, no. 8, pp. 1119-1121, 1996.

[7] X. J. Li and Y. Zhou, Eds., "Microfluidic devices for biomedical applications," Woodhead Publishing, 2021.

[8] D. T. Tran et al., "Investigation of mask selectivities and diamond etching using microwave plasma-assisted etching," Diamond and Related Materials, vol. 19, no. 7-9, pp. 778-782, 2010.

[9] K. Kordás et al., "Laser direct writing of copper on polyimide surfaces from solution," Applied Surface Science, vol. 154, pp. 399-404, 2000.

[10] A. Mohammed and A. Abdullah, "Scanning electron microscopy (SEM): A review," in Proceedings of the 2018 International Conference on Hydraulics and Pneumatics—HERVEX, Băile Govora, Romania, 2018, pp. 7-9.

[11] H. Seiler, "Secondary electron emission in the scanning electron microscope," Journal of Applied Physics, vol. 54, no. 11, pp. R1-R18, 1983.

[12] F. J. Giessibl, "Advances in atomic force microscopy," Reviews of modern physics, vol. 75, no. 3, p. 949, 2003.

[13] R. Garcıa and R. Perez, "Dynamic atomic force microscopy methods," Surface science reports, vol. 47, no. 6-8, pp. 197-301, 2002.

[14] J. Frascaroli et al., "Automatic defect detection in epitaxial layers by micro photoluminescence imaging," IEEE Transactions on Semiconductor Manufacturing, vol. 35, no. 3, pp. 540-545, 2022.

[15] L. Uhlig et al., "Micro-electroluminescence and micro-photoluminescence study on GaN-based laser diode aging," in Gallium Nitride Materials and Devices XVII, vol. 12001, pp. 37-43, SPIE, March 2022.

[16] C. Zwahr, B. Voisiat, A. Welle, D. Günther, and A. F. Lasagni, "One-Step Fabrication of Pillar and Crater-Like Structures on Titanium Using Direct Laser Interference Patterning," Adv. Eng. Mater., vol. 20, no. 7, pp. 1–9, 2018, doi: 10.1002/adem.201800160.

[17] B. Voisiat, C. Zwahr, and A. F. Lasagni, "Growth of regular micro-pillar arrays on steel by polarization-controlled laser interference patterning," Appl. Surf. Sci., vol. 471, no. September 2018, pp. 1065–1071, 2019, doi: 10.1016/j.apsusc.2018.12.083.

[18] A. C. Tarn, I. K. Pour, T. Nguyen, D. Krajnovich, and P. Baumgart, "Experimental and theoretical studies of bump formation during laser texturing of ni-p disk substrates," IEEE Trans. Magn., vol. 32, no. 5 PART 1, pp. 3771–3773, 1996, doi: 10.1109/20.538831.

[19] M. D'Alessandria, A. Lasagni, and F. Mücklich, "Direct micro-patterning of aluminum substrates via laser interference metallurgy," Appl. Surf. Sci., vol. 255, no. 5 PART 2, pp. 3210–3216, 2008, doi: 10.1016/j.apsusc.2008.09.018.

[20] C. T. Foxon, J. A. Harvey, and B. A. Joyce, "The evaporation of GaAs under equilibrium and non-equilibrium conditions using a modulated beam technique," J. Phys. Chem. Solids, vol. 34, no. 10, pp. 1693–1701, 1973, doi: 10.1016/S0022-3697(73)80135-0.

[21] J. Y. Tsao, Material Fundamentals of Molecular Beam Epitaxy. San Diego: Academic Press, 1993.

[22] C. Heyn, S. Schnüll, D. E. Jesson, and W. Hansen, "Thermally controlled widening of droplet etched nanoholes," Nanoscale Res. Lett., vol. 9, no. 1, pp. 1–8, 2014, doi: 10.1186/1556-276X-9-285.

Chapter 4

Design and Fabrication of Photonic Crystal Structures by Single Pulse Laser Interference Lithography

4.1 Introduction

The expansive realm of surface nanostructuring has been extensively explored for its potential to augment the energy conversion efficacy of semiconductor photonic devices, including but not limited to solar cells, LEDs, and LDs [1–4]. Si and GaAs are particularly noteworthy for their prevalent use in the construction of such semiconductor optoelectronic apparatus. GaAs distinguishes itself from Si through its possession of a direct bandgap, superior breakdown voltage, enhanced thermal stability, and significant radiation resistance, all of which contribute to its exceptional operational stability under arduous conditions [5-8]. However, a critical challenge confronting both Si and GaAs, as well as other semiconductors, is their inherent high surface reflectivity, which detrimentally impacts the external efficiency of these devices. In the visible spectrum, GaAs demonstrate a reflectivity exceeding 39%, with Si exhibiting marginally better performance. Specifically in the context of GaAs-based solar cells, the power conversion efficiency currently reaches a maximum of approximately 17.57% [9]. In the domain of GaAs LEDs, the external quantum efficiency is limited to a paltry 3% [10]. It is imperative to acknowledge that surface reflectivity plays a pivotal role in these suboptimal efficiency values.

Consequently, the employment of advanced surface engineering methodologies, such as antireflective coatings (ARCs) [11]–[15] and surface nanostructuring [16]–[18], emerges as an

indispensable requisite for the attainment of high-performance in photonic devices. ARCs are instrumental in increasing the transmittance across the visible spectrum, playing a pivotal role in diminishing surface reflection losses and the dependency on angular reflectivity. These enhancements are critical for bolstering the LEE in LEDs, ameliorating the contrast and luminosity in display technologies, and optimizing the performance of photovoltaic systems [19]. Nevertheless, the attainment of wideband antireflectance through ARCs necessitates a meticulous selection of materials endowed with specific refractive indices, coupled with the precise calibration of layer thicknesses. This requirement substantially increases the complexity inherent in the fabrication process. The elaborate nature of this process invariably precipitates an escalation in the temporal demands, both during the developmental stages and throughout the actual production of these multilayer coatings [20-24].

As an alternative, top-down surface nanostructuring, particularly the integration of periodic PhC structures, has been recognized for its capacity to furnish broadband and wide-angle anti-reflectance against incident light, alongside a marked diminution in radiant heat transmission [25]. These structures, often referred to as 'Moth Eye' configurations, are adeptly engineered to effectuate a pronounced decrease in spectral reflectance. This reduction encompasses a broad spectrum, ranging from the visible light domain (approximately 400 nm) to the mid-infrared region (extending up to 11 µm), achieving an average reflectance below 2% [26], [27]. Furthermore, PhCs are distinguished by their enhanced adaptability in the modulation of light, thereby transcending the confines of mere antireflective applications. Through the strategic manipulation of light propagation within their periodic nanostructures, PhCs pave the way for novel methodologies in the regulation and guidance of light across a multitude of avant-garde technological endeavors [28], [29]. Such applications include but are not limited to, the advancement of LEDs [30], [31], the optimization of solar cell efficiency [29], [32], the innovation in telecommunications [33], the refinement of sensor technologies [34], and the enhancement of various other optical instruments.

A lot of methods have been developed for the synthesis of PhC structures, including EBL [35], [36] and NIL [37–39]. While these techniques are acknowledged for their effectiveness, they are frequently accompanied by considerable financial outlays, representing a significant constraint in terms of cost. In contrast, LIL is acclaimed for its relative simplicity and cost-effectiveness, mitigating the financial constraints typically associated with nanofabrication.

Furthermore, LIL is distinguished by its capacity for expeditious fabrication, a crucial factor in accelerating production cycles. Additionally, the ability of LIL to pattern extensive areas further amplifies its suitability for industrial-scale manufactures [40–42]. Scholarly investigations have documented the utilization of LIL in the fabrication of PhC structures across a diverse array of substrates, including Si [43], polymers [44], and tungsten trioxide (WO3) [45]. However, the literature conspicuously lacks reports on the utilization of single-pulse LIL for the creation of PhC nanostructures, especially in the context of GaAs. This absence of exploration in the specific application of single-pulse LIL to PhC fabrication on GaAs substrates presents an intriguing opportunity for groundbreaking research. Venturing into this uncharted territory could potentially yield substantial contributions to the advancement of photonic device technologies.

In this study, we employ single-pulse three-beam LIL to fabricate PhC structures on GaAs substrates. This process is succeeded by the application of ICP etching, a technique employed to create nanoholes of varying depths. Our observations reveal that these surface engineered PhC nanoholes markedly enhance the light extraction and trapping capabilities within specific wavelength ranges, primarily by simulating the photonic band gap (PBG) phenomenon. Furthermore, we conducted surface reflectivity measurements, which elucidated a significant reduction in average reflectance. The measured values exhibited a decrease to below 4% across the visible wavelength spectrum, ranging from 400 to 700 nm. This investigation into the reflectivity modifications resulting from PhC integration seeks to unravel the mechanisms by which these nanostructures augment optical performance. The comprehension of these intricate interactions between PhC structures and optical properties is pivotal for the refinement and optimization of current photonic technologies. Moreover, it holds considerable promise in spearheading the development of future devices characterized by their superior light management capabilities, thereby contributing significantly to the field of photonics.

4.2 Design of PhC Structures by LIL

In this investigation, the LIL apparatus constitutes an integral element of the experimental setup. The functionality of this system is dictated by the flash-lamp pumped Nd:YAG laser and its operational parameters. These include a wavelength of 355 nm, a repetition rate of 5 Hz, a pulse duration of 7 nanoseconds, a long coherence length (at least 5m) and a beam diameter measuring 6 millimeters. The Nd:YAG laser is pivotal in this setup, acting as the foundational source for the generation of interference patterns essential to the research methodology.

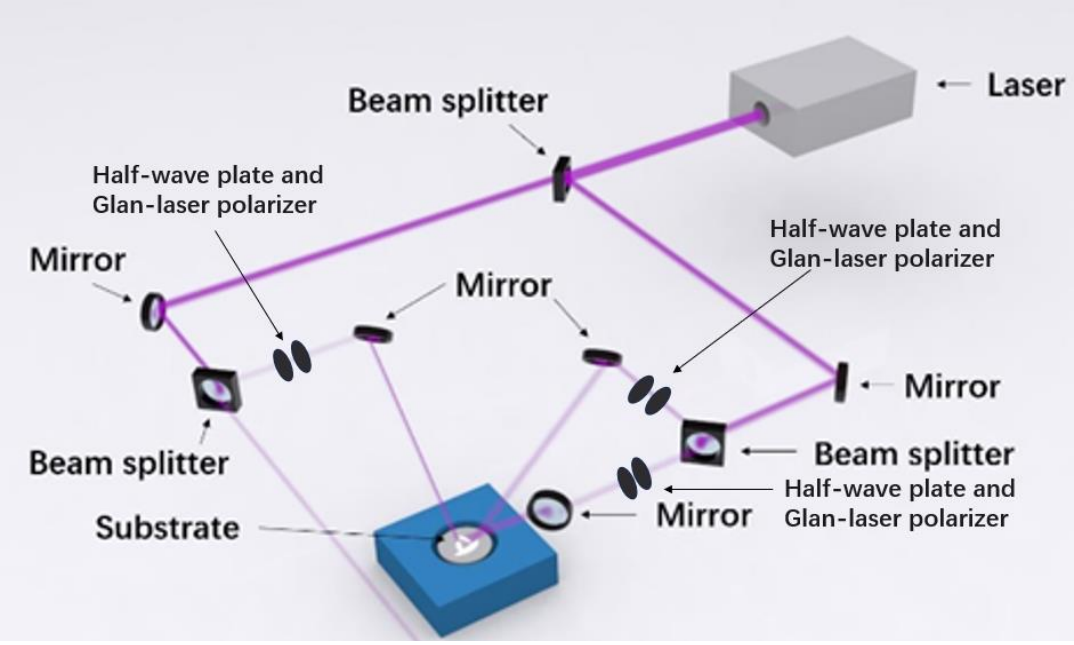

Figure 4.1. Three-beam LIL setup.

Figure 4.1 shows the configuration of the three-beam LIL apparatus. The operational paradigm of this LIL assembly entails the segmentation of the incident laser beam into four congruent beams, a process facilitated by the employment of beam splitters. It is worth noting that after the beams on the left side of the figure 4.1 have passed through the beam splitter, one of the beams is reflected by the mirror back to the sample, while the other beam is discarded for use. This is to ensure that the path and intensity of each beam arrived the sample is consistent. This three-beam approach offers a distinct advantage over the more

popular four-beam configurations by circumventing the generation of Moiré patterns, which could potentially compromise the integrity of the resultant nanostructures [42].

Optical pass design such as azimuth angles, incidence angles, and polarization need to consider our target PBG. Our work based on GaAs, particularly those within the light-emitting domain, predominantly function across the visible to near-infrared spectrum, with operational wavelengths typically spanning from approximately 850 nm to 1500 nm. In alignment with these operational parameters, an incidence angle of 43° has been strategically selected to yield a pitch size in the vicinity of 365 nm. This selection is strategically made to align with the operational wavelength range of GaAs-based devices. We expect to get square periodic mode with cycle patterns like figure 2.8 (a) in Chapter 2 shown. Using the foundational principles of LIL, which have been extensively delineated in Chapter 2 and our previous scholarly contributions [42], [46], the pattern formation employing a three-beam LIL setup can rigorously simulated utilizing MATLAB. This simulation process plays a pivotal role in the theoretical support and planning necessary for the effective realization of PhC structures. Figures 4.2 (a) and 4.2 (b) exhibit both 2D and 3D simulations of the laser intensity distribution pattern. Three beams LIL obviously make it difficult to achieve a standard circle, but it is possible to achieve an elliptical pattern that is very close to a circle (azimuthal angles set at 0°, 90°, and 180° , respectively and polarization angles are all set to 0°).

In this work, following their separation, these beams are coherently reconstituted at the substrate's surface. Within this arrangement, the beams are meticulously oriented at an incidence angle of 43°, with azimuthal angles precisely set at 0°, 90°, and 180° , respectively and polarization angles are all set to 0°. Such scrupulous alignment is paramount for the fabrication of nanostructures that conform to the specified configuration. The interference pattern engendered by this setup is anticipated to manifest the requisite periodicity and uniformity, characteristics that are essential for their application within the realms of photonics and nanotechnology.

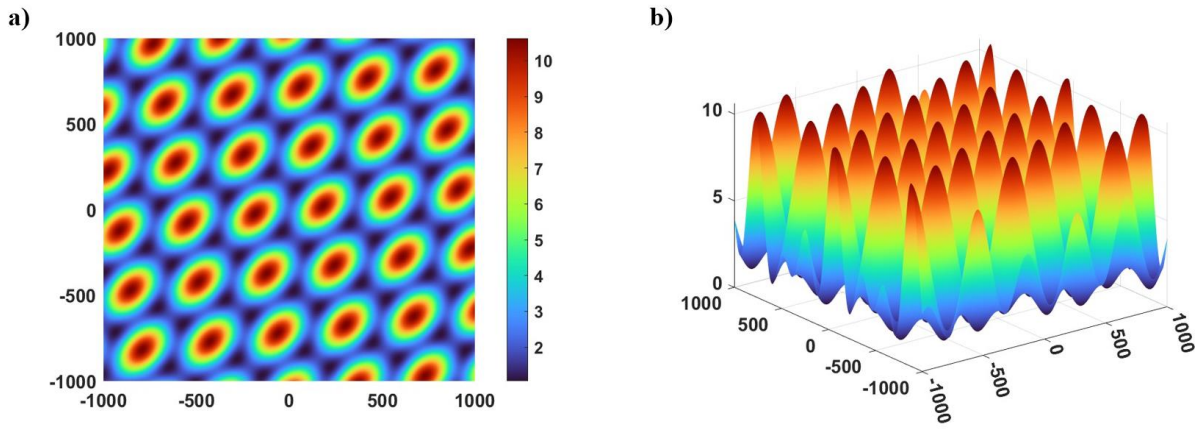

Figure 4.2. (a) 2D, (b) 3D laser intensity distribution pattern.

4.3 Experimental Details

The experimental methodology is delineated in Figure 4.3. Initial preparatory steps involved subjecting GaAs substrates to a comprehensive three-stage cleaning process. After this pre-cleaning phase, a 180 nm-thick layer of mr-P 1200LIL photoresist, a product of Microresist Technology GmbH specifically formulated for laser lithography applications, was uniformly applied to the substrates via a spin-coating technique. This photoresist is renowned for its high lithographic contrast, even at relatively minimal film thicknesses, a property that significantly aids our achievement of contrast. Previous experimental endeavors employing conventional greyscale lithography photoresists at increased thicknesses ranging from 1 to 2 µm encountered substantive challenges. Specifically, these thicker photoresist layers presented impediments in achieving uniform exposure throughout their entire depth, often resulting in residual unexposed photoresist that proved recalcitrant to subsequent etching processes. It is noteworthy, however, that the depth of photoresist exposure can be augmented by increasing the laser pulse power. Despite this, one must exercise caution as this (and perhaps *any*) photoresist is susceptible to laser-induced damage under high-energy regimes. The utilization of a thin, high-contrast photoresist, as in this study, facilitates complete etching by a lower energy single pulse in the LIL process. This approach optimizes

the etching process, ensuring thorough removal of the photoresist and thereby enhancing the overall efficacy and precision of the photonic structure fabrication.

After the application of the photoresist, it was subjected to a single pulse selected from the 10Hz output by means of a shutter. Following development and assessment of the photoresist pattern, the pattern is then transferred to the substrate via ICP etching. The etching process was meticulously regulated to achieve a consistent rate of 200 nanometers per minute. By modulating the duration of the etching process, a series of samples featuring PhC structures with different etch depths were successfully realized.

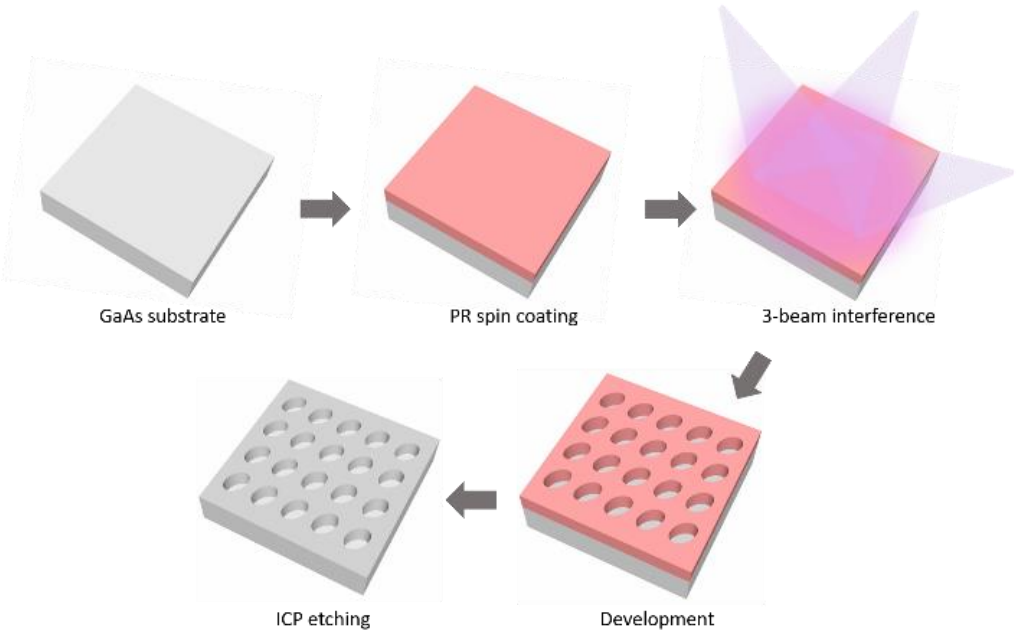

Figure 4.3. The fabrication process of the PhC structures.

4.4 Results and Discussion

4.4.1 Structural Analysis

Figures 4.4 (a), 4.4 (b), and 4.4 (c) present SEM images of GaAs surfaces, post-fabrication, which have been patterned with PhC structures following the completion of the fabrication process. These images reveal a consistent and periodic arrangement of nanoholes extending across a substantial surface area. Notably, the spatial periodicity of these nanoholes, as evidenced in the SEM images, is approximately 365 nm. This measured pitch aligns with the predictions established through prior MATLAB-based simulation efforts.

The dimensions of each nanohole in the PhC structures are dependent on the laser energy deployed during the lithographic process. When the laser energy is low, as depicted in Figure 4.2 (a) showing the laser intensity distribution pattern, only the central region with the highest energy concentration can alter the photoresist, resulting in a small size final nanohole. However, by increasing the laser energy, regions with lower energy distribution also affect the photoresist, leading to an enlargement of the final nanohole size. An adjustment of the nanohole radius (r) in proportion to the pitch (P), along with the consideration of the refractive index disparity between the nanoholes and the surrounding GaAs, can influence the characteristics of the PBG. A diminution in the r/P ratio is associated with a narrowing of the PBG, which exhibits a linear expansion in response to increases in this ratio. Additionally, an increase in the proportion of air within the structure, achieved by increasing the nanohole radius, results in an elevation of the central frequency of the bandgap. However, an increase in nanohole radius also introduces heightened optical losses attributable to the diminished presence of the guiding material. Furthermore, this escalation presents fabrication challenges, particularly in maintaining distinct separation between larger adjacent nanoholes [47]. This interplay necessitates a balance between the desired bandgap size and the practical limitations inherent in the fabrication process. The choice of laser intensity is pivotal, as excessive intensity may lead to the unintended merging of adjacent nanoholes, thereby compromising the PhC structure's architecture. Conversely, insufficient laser intensity may result in suboptimal exposure depth in the photoresist, leaving behind residual material that impedes efficient etching. To achieve a good pattern, a laser energy of 9 mJ was selected for this experiment, which yielded PhC structures with desirable characteristics. Under these specified conditions, the nanoholes predominantly exhibit an elliptical form, with the major axis of the ellipse extending up to approximately 315 nm and the minor axis measuring around 305 nm in diameter.

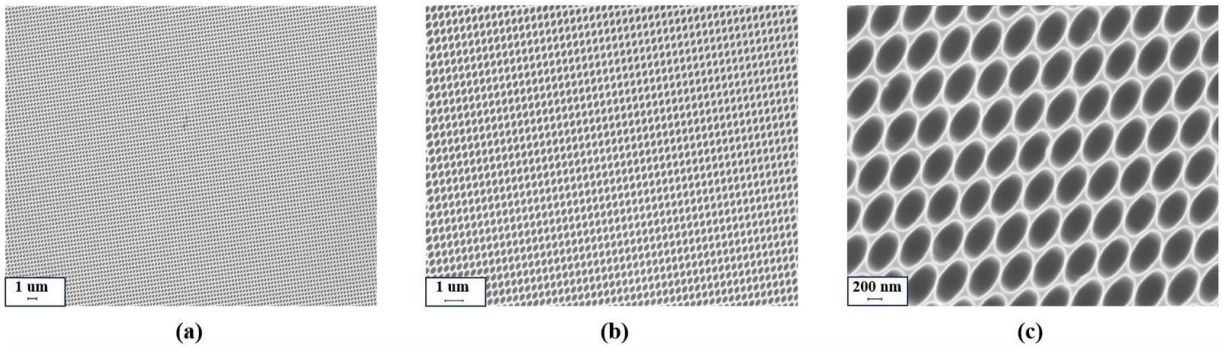

Figure 4.4. (a), (b), (c) SEM images of the GaAs substrate with the fabricated PhC structure.

4.4.2 Photonic Band Gap of the 2D PhC

The emergence of PBGs is closely connected to the configuration of the Brillouin zone, as illustrated in Figure 4.5 (a). The inherent periodicity of the PhC, which establishes the boundaries of the Brillouin zone, initiates Bragg scattering and wave interference, leading to the development of PBGs. Within the square Brillouin zone, the wave vectors trace the path ΓMXΓ. Figure 4.5 (b) displays the results from simulating the PBG using the FDTD approach, offering insights into the dimensions and spacing of the nanoholes derived from SEM investigations. The graph reveals the presence of PBGs in two specific frequency bands: initially between normalized frequencies of 0.28 and 0.31, and subsequently from 0.38 to 0.44. Such findings suggest that the analyzed 2D PhC structure serves effectively as an out-coupler for TE modes across its functional wavelength spectrum, which extends from 830 nm to 960 nm and 1177 nm to 1303 nm. The relevance of these spectral ranges is underscored by their congruence with the emission spectra of various semiconductor devices, notably the 830 nm to 960 nm range aligning with GaAs/InGaAs-based LEDs and LDs. Furthermore, the 1177 nm to 1303 nm spectrum corresponds to the O-band, renowned for its minimal dispersion and attenuation in optical fibers, thus rendering it suitable for long-range and high-precision data communication applications.

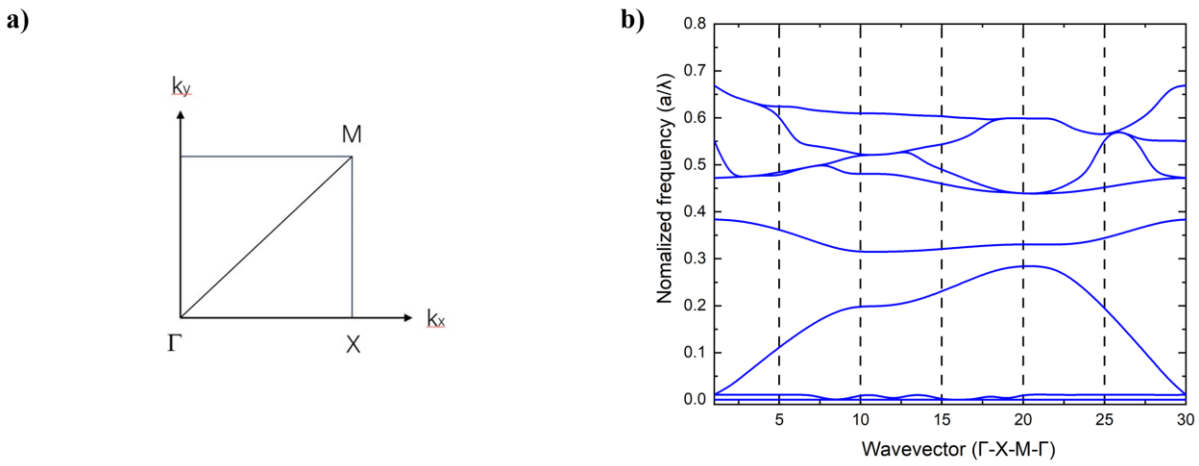

Figure 4.5. (a) The Brillouin zone, (b) The PBG for the 2D PhC obtained from FDTD.

4.4.3 AFM and Reflectance Results Analysis

The reflectance properties of the fabricated PhC structures, varying in depth, were analyzed utilizing a spectrometer equipped with an ASEQ instruments high-resolution spectrometer, which was integrated into an optical microscope providing visible spectrum illumination from 450 nm to 700 nm. As detailed in Chapter 3 and our prior publication [48], this experimental configuration facilitates the assessment of reflectance across distinct pattern depths. The incorporation of a panning stage within the setup ensures the precise alignment of the sample, thereby enabling accurate reflectance measurements of each pattern via the microscope. The microscope's adjustable aperture control mechanism allows for the concentration of illumination onto specific pattern areas. For this investigation, a 50X microscope objective was employed, characterized by a NA of 0.56 and a 33.3° half-cone angle, although objectives with an NA as high as 1 or a 100X magnification could also be utilized.

The reflectivity characteristics of GaAs substrates, with and without integrated PhC structures at different depths, were examined and compared. Utilizing the technique of ICP etching, a range of PhC structures were created at designated depths, specifically 80 nm, 200 nm, 300 nm, 350 nm, and 400 nm. The surface topographies of these fabricated structures were captured and illustrated using AFM, as presented in Figure 4.6.

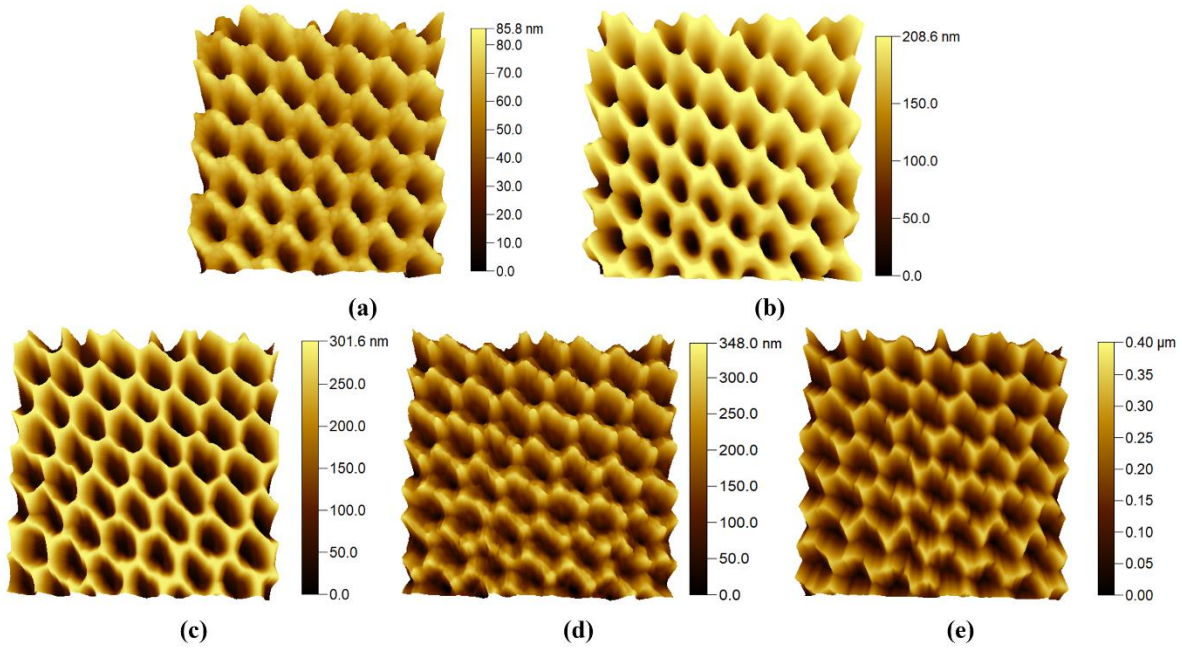

Figure 4.6. a) 80 nm, b) 200 nm, c) 300nm, d) 350 nm, e) 400nm depths PhC structure on GaAs substrate.

Figure 4.7 depicts the reflectance spectra derived from the analyzed samples. The bare GaAs substrate demonstrated a typically high reflectance, reaching up to 39% in the wavelength spectrum of 450 nm to 700 nm. This elevated reflectance level can be attributed to the stark difference in the refractive indices between air and the GaAs dielectric material, which has a refractive index of around 3.8. It's crucial to understand that PhC structures themselves do not alter this inherent high refractive index contrast. Instead, they use this contrast to intricately control the propagation of light, thus effectively reducing the perpendicular reflectance and trapping the light in the plane.

Our study highlights the significant impact of the depth of PhC structures on reflectivity. Analysis of the reflectance data presented in Figure 4.7 reveals a correlation between the depth of the nanoholes within the PhC structures and their effect on reflectivity. The data indicates that as the depth of the nanoholes increases from 80 nm to 350 nm, there is a corresponding reduction in reflectivity. Notably, at a nanohole depth of 350 nm, the average reflectance decreases to below 5% over the wavelength range of 400 nm to 700 nm, marking a substantial sevenfold decrease in reflectance compared to a GaAs substrate without the PhC structure. This reduction in reflectance is attributed to enhanced light trapping capabilities, where incident light is subjected to longer paths within the material, increasing

the likelihood of absorption. Moreover, deeper PhC structures enhance the Bragg scattering effect, a result of the periodic structure of the crystal leading to light diffraction and subsequent constructive or destructive interference. This interference effectively reduces the amount of light reflected off the surface, while the diffraction effects can also be tailored to steer light away from the surface, further diminishing reflectivity.

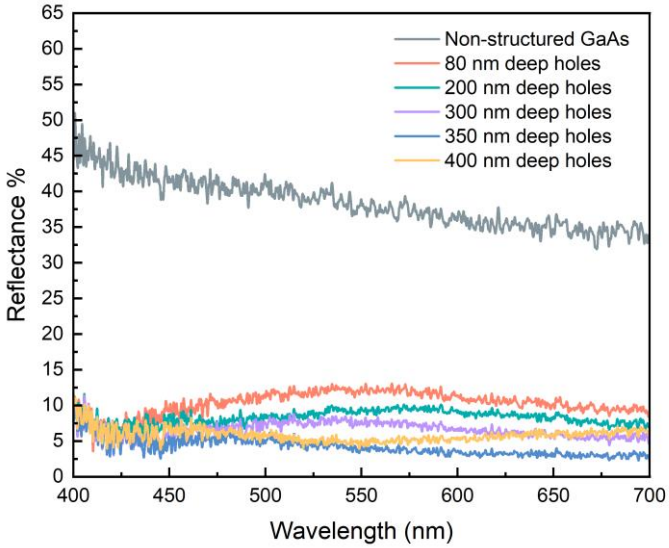

Figure 4.7 Comparative analysis of reflectance between bare GaAs substrates and GaAs substrates embedded with PhC structures ranging in depths from 80 nm to 400 nm.

However, at depths reaching 400 nm, the trend of decreasing reflectivity observed at shallower depths was not maintained, and a slight uptick in reflectivity was noted instead.

It appears that beyond a certain depth threshold, the impact on light trapping becomes counterproductive, or additional diffraction effects that are not favorable might be introduced, thereby altering the reflectivity in a manner that is not advantageous.

4.5 Conclusion

In this study, we have successfully engineered and constructed PhC structures on GaAs substrates using the single pulse LIL method. The surface morphology of these created PhC structures was confirmed to align with our initial designs, as evidenced by SEM and AFM analyses. FDTD simulations were performed to elucidate the PBG characteristics inherent to these structures. The findings indicate that these PhC structures hold promise for incorporation into GaAs-based optoelectronic devices, potentially augmenting their operational efficacy within certain wavelength domains. Our experimental data have shown that the average reflectance of GaAs substrates with PhC structures can be markedly reduced, falling below 5% over a wide wavelength range of 450 nm to 700 nm. Consequently, the PhC structures developed in this research are poised to improve light extraction efficiency in light-emitting devices and enhance light trapping in photovoltaic systems. The versatility of single pulse LIL allows for its application across various semiconductor materials, paving the way for the development of highly efficient optoelectronic devices suitable for broadband applications. The deployment of this cost-effective, high-throughput technique holds substantial promise for future advancements in the realms of photonics and optoelectronics.

Reference

[1] C. Ducros, A. Brodu, G. Lorin, F. Emieux, and A. Pereira, “Optical performances of antireflective moth-eye structures. Comparison with standard vacuum antireflection coatings for application to outdoor lighting LEDs,” *Surf Coat Technol*, vol. 379, Dec. 2019, doi: 10.1016/j.surfcoat.2019.125044.

[2] G. Tan *et al.*, “Broadband antireflection film with moth-eye-like structure for flexible display applications,” *Optica*, vol. 4, no. 7, p. 678, Jul. 2017, doi: 10.1364/optica.4.000678.

[3] S. Almenabawy, Y. Zhang, A. Flood, R. Prinja, and N. P. Kherani, “Nanometer-Mesa Inverted-Pyramid Photonic Crystals for Thin Silicon Solar Cells,” *ACS Appl Energy Mater*, vol. 5, no. 11, pp. 13808–13816, Nov. 2022, doi: 10.1021/acsaem.2c02437.

[4] D. Przybylski and S. Patela, “Modelling of a two-dimensional photonic crystal as an antireflection coating for optoelectronic applications,” *Opto-Electronics Review*, vol. 27, no. 1, pp. 79–89, Mar. 2019, doi: 10.1016/j.opelre.2019.02.004.

[5] A. Sharma and T. D. Das, “Electronic band structure and optical properties of GaAsSb/GaAs for optoelectronic device applications: A 14 band k.p study,” *Opt Mater (Amst)*, vol. 112, Feb. 2021, doi: 10.1016/j.optmat.2020.110734.

[6] T. Lin, J. nan Xie, S. huan Ning, Q. min Li, and B. Li, “Study on the p-type ohmic contact in GaAs-based laser diode,” *Mater Sci Semicond Process*, vol. 124, Mar. 2021, doi: 10.1016/j.mssp.2020.105622.

[7] S. Sederberg, F. Kong, F. Hufnagel, C. Zhang, E. Karimi, and P. B. Corkum, “Vectorized optoelectronic control and metrology in a semiconductor,” *Nat Photonics*, vol. 14, no. 11, pp. 680–685, Nov. 2020, doi: 10.1038/s41566-020-0690-1.

[8] T. Zaengle *et al.*, “A Novel Route to Fibers with Incongruent and Volatile Crystalline Semiconductor Cores: GaAs,” *ACS Photonics*, vol. 9, no. 3, pp. 1058–1064, Mar. 2022, doi: 10.1021/acsphotonics.2c00008.

[9] D. Parajuli, G. S. Gaudel, D. Kc, K. B. Khattri, and W. Y. Rho, “Simulation study of TiO2 single layer anti-reflection coating for GaAs solar cell,” *AIP Adv*, vol. 13, no. 8, Aug. 2023, doi: 10.1063/5.0153197.

[10] T. C. Lin *et al.*, “Large-Signal Modulation Performance of Light-Emitting Diodes with Photonic Crystals for Visible Light Communication,” *IEEE Trans Electron Devices*, vol. 65, no. 10, pp. 4375–4380, Oct. 2018, doi: 10.1109/TED.2018.2864346.

[11] G. Oh, Y. Kim, S. J. Lee, and E. K. Kim, “Broadband antireflective coatings for high efficiency InGaP/GaAs/InGaAsP/InGaAs multi-junction solar cells,” *Solar Energy Materials and Solar Cells*, vol. 207, Apr. 2020, doi: 10.1016/j.solmat.2019.110359.

[12] W. Zhang *et al.*, “Broadband graded refractive index TiO2/Al2O3/MgF2 multilayer antireflection coating for high efficiency multi-junction solar cell,” *Solar Energy*, vol. 217, pp. 271–279, Mar. 2021, doi: 10.1016/j.solener.2021.01.012.

[13] G. J. Hou, I. García, and I. Rey-Stolle, “High-low refractive index stacks for broadband antireflection coatings for multijunction solar cells,” *Solar Energy*, vol. 217, pp. 29–39, Mar. 2021, doi: 10.1016/j.solener.2021.01.060.

[14] M. A. Zahid, M. Q. Khokhar, Z. Cui, H. Park, and J. Yi, “Improved optical and electrical properties for heterojunction solar cell using Al2O3/ITO double-layer anti-reflective coating,” *Results Phys*, vol. 28, Sep. 2021, doi: 10.1016/j.rinp.2021.104640.

[15] T. Sertel, Y. Ozen, V. Baran, and S. Ozcelik, “Effect of single-layer Ta2O5 and double-layer SiO2/Ta2O5 anti-reflective coatings on GaInP/GaAs/Ge triple-junction solar cell performance,” *J Alloys Compd*, vol. 806, pp. 439–450, Oct. 2019, doi: 10.1016/j.jallcom.2019.07.257.

[16] S. Ji, K. Song, T. B. Nguyen, N. Kim, and H. Lim, “Optimal moth eye nanostructure array on transparent glass towards broadband antireflection,” *ACS Appl Mater Interfaces*, vol. 5, no. 21, pp. 10731–10737, Nov. 2013, doi: 10.1021/am402881x.

[17] F. Galeotti, F. Trespidi, G. Timò, and M. Pasini, “Broadband and crack-free antireflection coatings by self-assembled moth eye patterns,” *ACS Appl Mater Interfaces*, vol. 6, no. 8, pp. 5827–5834, Apr. 2014, doi: 10.1021/am500687f.

[18] Y.-J. Hung *et al.*, “5. Z. Fan, DChallenges and prospects of nanopillar-based solar cells,” 2006.

[19] H. K. Raut, V. A. Ganesh, A. S. Nair, and S. Ramakrishna, “Anti-reflective coatings: A critical, in-depth review,” *Energy and Environmental Science*, vol. 4, no. 10. pp. 3779–3804, Oct. 2011. doi: 10.1039/c1ee01297e.

[20] M. A. Zahid, M. Q. Khokhar, Z. Cui, H. Park, and J. Yi, “Improved optical and electrical properties for heterojunction solar cell using Al2O3/ITO double-layer anti-reflective coating,” *Results Phys*, vol. 28, Sep. 2021, doi: 10.1016/j.rinp.2021.104640.

[21] M. A. Zahid, M. Q. Khokhar, S. Park, S. Q. Hussain, Y. Kim, and J. Yi, “Influence of Al2O3/IZO double-layer antireflective coating on the front side of rear emitter silicon heterojunction solar cell,” *Vacuum*, vol. 200, Jun. 2022, doi: 10.1016/j.vacuum.2022.110967.

[22] M. A. Zahid, M. Q. Khokhar, Y. Kim, and J. Yi, “Utilization of CaF2/ITO Double-Layer Anti-Reflective Coating for Increasing the Efficiency in Rear Emitter SHJ Solar Cells,” *Crystal Research and Technology*, vol. 57, no. 8, Aug. 2022, doi: 10.1002/crat.202100233.

[23] Y. S. Lee, L. Y. Chuang, C. J. Tang, Z. Z. Yan, B. S. Le, and C. C. Jaing, “Investigation into the Characteristics of Double-Layer Transparent Conductive Oxide ITO/TNO Anti-Reflection Coating for Silicon Solar Cells,” *Crystals (Basel)*, vol. 13, no. 1, Jan. 2023, doi: 10.3390/cryst13010080.

[24] N. Sahouane and A. Zerga, “Optimization of antireflection multilayer for industrial crystalline silicon solar cells,” in *Energy Procedia*, 2014, pp. 118–125. doi: 10.1016/j.egypro.2013.12.017.

[25] A. H. Chiou, C. W. Chang, and C. J. Ting, “Spectrally selective antireflection of nanoimprint lithography-formed 3D spherical structures on film coated with a silver layer,” *Sci Rep*, vol. 12, no. 1, Dec. 2022, doi: 10.1038/s41598-022-23348-w.

[26] L. Dong *et al.*, “Controllable superhydrophobic surfaces with tunable adhesion fabricated by laser interference lithography,” *Surf Coat Technol*, vol. 372, pp. 434–441, Aug. 2019, doi: 10.1016/j.surfcoat.2019.05.039.

[27] L. Dong *et al.*, “Fabrication of hierarchical moth-eye structures with durable superhydrophobic property for ultra-broadband visual and mid-infrared applications,” *Appl Opt*, vol. 58, no. 24, p. 6706, Aug. 2019, doi: 10.1364/ao.58.006706.

[28] T. Sridarshini and S. Indira Gandhi, “Photonic band structure of 2D photonic crystals - A comparative study,” *Laser Phys*, vol. 30, no. 2, 2020, doi: 10.1088/1555-6611/ab5795.

[29] D. Przybylski and S. Patela, “Modelling of a two-dimensional photonic crystal as an antireflection coating for optoelectronic applications,” *Opto-Electronics Review*, vol. 27, no. 1, pp. 79–89, Mar. 2019, doi: 10.1016/j.opelre.2019.02.004.

[30] K. Wang, X. Dong, Y. Bu, and X. Wang, “Design of photonic crystals for light-emitting diodes,” *Journal of the American Ceramic Society*. John Wiley and Sons Inc, Dec. 01, 2023. doi: 10.1111/jace.19388.

[31] L. Suslik *et al.*, “Photonic crystal and photonic quasicrystal patterned in PDMS surfaces and their effect on LED radiation properties,” *Appl Surf Sci*, vol. 395, pp. 220–225, Feb. 2017, doi: 10.1016/j.apsusc.2016.07.051.

[32] S. Almenabawy, Y. Zhang, A. Flood, R. Prinja, and N. P. Kherani, “Nanometer-Mesa Inverted-Pyramid Photonic Crystals for Thin Silicon Solar Cells,” *ACS Appl Energy Mater*, vol. 5, no. 11, pp. 13808–13816, Nov. 2022, doi: 10.1021/acsaem.2c02437.

[33] M. A. Husanu, C. P. Ganea, I. Anghel, C. Florica, O. Rasoga, and D. G. Popescu, “Surface topography to reflectivity mapping in two-dimensional photonic crystals designed in germanium,” *Appl Surf Sci*, vol. 355, pp. 1186–1191, Nov. 2015, doi: 10.1016/j.apsusc.2015.07.218.

[34] H. Kaviani and J. Barvestani, “Photonic crystal based biosensor with the irregular defect for detection of blood plasma,” *Appl Surf Sci*, vol. 599, Oct. 2022, doi: 10.1016/j.apsusc.2022.153743.

[35] S. P. Yu, D. C. Cole, H. Jung, G. T. Moille, K. Srinivasan, and S. B. Papp, “Spontaneous pulse formation in edgeless photonic crystal resonators,” *Nat Photonics*, vol. 15, no. 6, pp. 461–467, Jun. 2021, doi: 10.1038/s41566-021-00800-3.

[36] J. Li, J. Yan, L. Jiang, J. Yu, H. Guo, and L. Qu, “Nanoscale multi-beam lithography of photonic crystals with ultrafast laser,” *Light Sci Appl*, vol. 12, no. 1, Dec. 2023, doi: 10.1038/s41377-023-01178-3.

[37] K. J. Byeon, S. Y. Hwang, and H. Lee, “Fabrication of two-dimensional photonic crystal patterns on GaN-based light-emitting diodes using thermally curable monomer-based nanoimprint lithography,” *Appl Phys Lett*, vol. 91, no. 9, 2007, doi: 10.1063/1.2776980.

[38] M. Torras, P. Molet, L. Soler, J. Llorca, A. Roig, and A. Mihi, “Au/TiO2 2D-Photonic Crystals as UV–Visible Photocatalysts for H2 Production,” *Adv Energy Mater*, vol. 12, no. 6, Feb. 2022, doi: 10.1002/aenm.202103733.

[39] H. Zhao, X. Cao, Q. Dong, C. Song, L. Wang, and L. Gao, “Large-area silicon photonic crystal supporting bound states in the continuum and optical sensing formed by nanoimprint lithography,” *Nanoscale Adv*, vol. 5, no. 5, pp. 1291–1298, Jan. 2023, doi: 10.1039/d3na00001j.

[40] N. Pérez, T. Tavera, A. Rodríguez, M. Ellman, I. Ayerdi, and S. M. Olaizola, “Fabrication of sub-micrometric metallic hollow-core structures by laser interference lithography,” in *Applied Surface Science*, Elsevier B.V., Sep. 2012, pp. 9370–9373. doi: 10.1016/j.apsusc.2012.03.185.

[41] M. Ellman *et al.*, “High-power laser interference lithography process on photoresist: Effect of laser fluence and polarisation,” *Appl Surf Sci*, vol. 255, no. 10, pp. 5537–5541, Mar. 2009, doi: 10.1016/j.apsusc.2008.07.201.

[42] Y. R. Wang, I. S. Han, C. Y. Jin, and M. Hopkinson, “Precise Arrays of Epitaxial Quantum Dots Nucleated by in Situ Laser Interference for Quantum Information Technology Applications,” *ACS Appl Nano Mater*, vol. 3, no. 5, pp. 4739–4746, May 2020, doi: 10.1021/acsanm.0c00738.

[43] L. Dong, Z. Zhang, Z. Wang, D. Li, and M. Liu, “Design an asymmetrical three-beam laser interference lithography for fabricating micro- and nano-structures,” *Journal of Laser Micro Nanoengineering*, vol. 15, no. 2, pp. 85–91, Sep. 2020, doi: 10.2961/jlmn.2020.02.2002.

[44] I. Martín-Fabiani *et al.*, “Micro- and submicrostructuring thin polymer films with two and three-beam single pulse laser interference lithography,” *Langmuir*, vol. 30, no. 29, pp. 8973–8979, Jul. 2014, doi: 10.1021/la5021059.

[45] I. Castro-Hurtado *et al.*, “Structural and optical properties of WO 3 sputtered thin films nanostructured by laser interference lithography,” *Appl Surf Sci*, vol. 276, pp. 229–235, Jul. 2013, doi: 10.1016/j.apsusc.2013.03.072.

[46] Y.-R. Wang, S. M. Olaizola, I. S. Han, C.-Y. Jin, and M. Hopkinson, “Direct patterning of periodic semiconductor nanostructures using single-pulse nanosecond laser interference,” *Opt Express*, vol. 28, no. 22, p. 32529, Oct. 2020, doi: 10.1364/oe.397709.

[47] M. Qiu and S. He, “Large complete band gap in two-dimensional photonic crystals with elliptic air holes,” *Phys Rev B Condens Matter Mater Phys*, vol. 60, no. 15, pp. 10610–10612, 1999, doi: 10.1103/PhysRevB.60.10610.

[48] S. Behera, P. W. Fry, H. Francis, C. Y. Jin, and M. Hopkinson, “Broadband, wide-angle antireflection in GaAs through surface nano-structuring for solar cell applications,” *Sci Rep*, vol. 10, no. 1, Dec. 2020, doi: 10.1038/s41598-020-63327-7.

Chapter 5

Photonic Crystal Enhanced Light Emitting Diodes Fabricated by Single Pulse Laser Interference Lithography

5.1 Introduction

PhC structures are increasingly acknowledged for their ability to substantially improve the performance of light-emitting devices, including LEDs [1], [2], OLEDs [3], and LDs [4], [5]. Among these, the conventional LED, a widely used technology, has attracted significant interest from the research community due to its numerous benefits such as energy efficiency and long lifetime. LEDs find application in a wide range of fields, including but not limited to general lighting [6,] [7], infrared illumination [8]–[10], display technologies [11–13], quantum computing [14], [15], and telecommunications [16–18]. However, despite their high internal quantum efficiency, the external quantum efficiency of standard LEDs typically remains around a modest 3% [19], primarily due to the high refractive index of the semiconductor materials used in LEDs. This limitation highlights the critical need for enhancing the LEE of LEDs [20], as the current inefficiency in light output constitutes a significant loss of energy, emphasizing the necessity for technological innovations in this area.

To improve the light output efficiency of LEDs, the research community has explored a variety of strategies, including the use of meta-surfaces [21], [22], patterned electrodes [23], [24], and alterations in epitaxial growth techniques [25], [26]. Each of these methods has shown potential in increasing the light-emitting capabilities of LEDs to different extents. However, the complexity and cost associated with these advanced techniques often render them

impractical for cost-sensitive applications. In contrast, PhC structures have been identified as a viable and efficient alternative for enhancing the luminous efficacy of LEDs. By employing periodic nanostructuring, PhC structures effectively manipulate light propagation, providing a straightforward approach to improve LEE. This method enables precise control over the efficiency, spectral purity, and directionality of the emitted light without necessitating any specialized device configurations [27], [28].

A fundamental feature of PhCs is the presence of a PBG, which defines a range of wavelengths that cannot propagate through the crystal structure, effectively allowing for the selective blocking or transmission of specific wavelengths. This characteristic facilitates the removal of unwanted spectral components [19].

Various methods have been employed to create PhC structures on LEDs, including traditional UV lithography [29], EBL [30], [31], and NIL [32], [33]. Although these techniques offer high precision in nanopatterning, they are often marked by high costs and limited throughput. In contrast, LIL emerges as a cost-efficient and maskless alternative to these conventional nanofabrication methods. LIL is especially noted for its quick processing capabilities, which are essential for reducing production timelines. Its ability to pattern large areas efficiently makes it particularly attractive for widespread industrial application. While there have been studies investigating the application of two-beam or multi-pulse LIL for the incorporation of PhC structures into LEDs, thereby significantly boosting their light efficiency [34–36], the use of single-pulse LIL for crafting PhC nanostructures on GaAs-based LEDs remains relatively unexplored in the existing literature.

Our method demonstrates that the application of a single nanosecond pulse exposure holds the promise to transform LED fabrication processes into a cost-efficient, high-throughput production paradigm. This approach, when integrated with a rapid step-and-repeat mechanism, enables the patterning of entire wafers with nanoscale periodic arrays swiftly and without the need for high vibrational stability, courtesy of the rapid exposure time.

In our study, we implemented a three-beam single-pulse LIL strategy to fabricate PhC structures with diverse depths on samples of GaAs/AlGaAs MQW LEDs. The adoption of a three-beam configuration is deliberate to avoid the Moiré pattern complications commonly associated with LIL techniques that use four or more beams [37]. After the exposure of the

photoresist, we employ ICP etching to generate arrays of nanoholes. To supplement our experimental efforts, FDTD simulations, conducted using Lumerical software, have been instrumental in evaluating the PBG attributes and in assessing the influence of varying PhC depths on the LEE enhancement.

Figure 5.1 delineates the method employed in the preparation of LED samples. In this investigation, the LEDs were produced using MBE on n-type GaAs substrates. The LED structure is characterized by its multilayer composition, beginning with a 400 nm thick n-doped GaAs buffer layer, succeeded by a 1300 nm thick n-doped $Al_{0.3}Ga_{0.7}As$ confinement layer. The core active region is constituted by three layers of 9 nm thick GaAs QWs, each interspersed with 24 nm thick $Al_{0.3}Ga_{0.7}As$ barrier layers. This is topped with an 800 nm p-doped $Al_{0.3}Ga_{0.7}As$ confinement layer, and the structure concludes with a 20 nm p-doped GaAs cap layer, forming the top section of the device.

Central to our experimental arrangement is the LIL system, which is powered by a flash-lamp pumped Nd:YAG laser. This laser is distinguished by its operational parameters, including a 355 nm emission wavelength, a 5 Hz repetition rate, a 7 ns pulse duration, and a 5 mm beam diameter. By employing a combination of beam splitters and mirrors, the laser output is divided into four coherent beams, with three of these beams being directed to converge precisely at a single point on the LED sample. This accurate alignment is essential to achieve the desired interference effects, which are critical to the aims of our research.

The preparation of the LED samples was initiated with a comprehensive three-step cleaning process, succeeded by a prebaking phase. Subsequently, the substrates were uniformly coated with a 180 nm layer of mr-P 1200LIL photoresist, a product specifically formulated by Micro Resist Technology GmbH for laser lithography applications. This photoresist is distinguished by its ability to provide high contrast for precise patterning, even at minimal film thicknesses. It's important to note that the depth of photoresist exposure can be adjusted by altering the laser pulse energy, although higher laser energies, necessary for deeper photoresist exposure, may risk laser-induced damage.

Following the photoresist application, the sample was exposed to a single 7 nanosecond pulse from a three-beam LIL setup, resulting in the formation of the desired PhC pattern. The pitch of this pattern could be modified by adjusting the incidence angles of the laser beams. The

pattern was then transferred from the photoresist onto the substrate through ICP etching. By varying the duration of the etching process, PhC structures with different depths were successfully created. A metallization step followed, where a 30 nm titanium layer and a subsequent 200 nm gold layer were applied to both the bottom and top surfaces of the samples. Any extraneous metal was removed using a lift-off process to define the electrode patterns clearly. The fabrication concluded with the formation of mesa structures via ICP etching, culminating in the production of 400 μm diameter LED devices embedded with PhC structures.

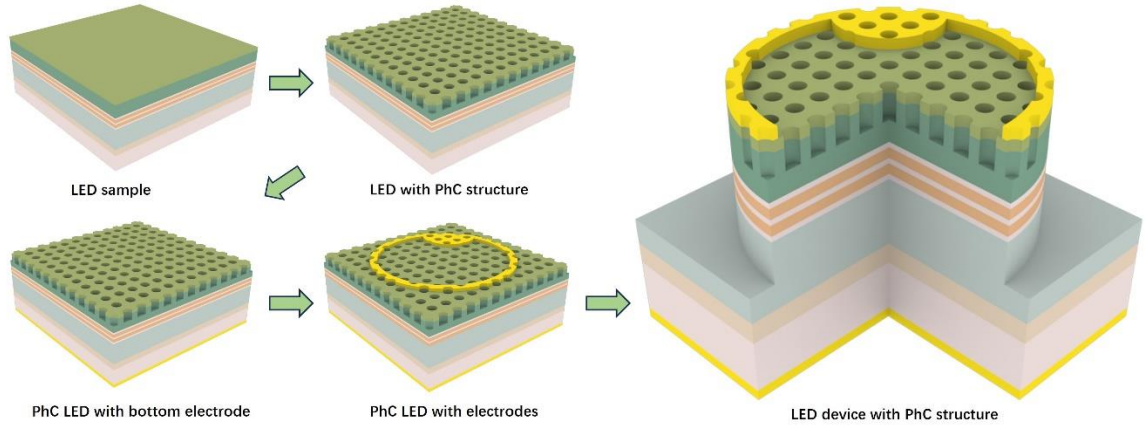

Figure 5.1. Fabrication process of the PhC structure on LED device.

5.2 PhC Structure Characteristics

This research focuses on the GaAs-based LEDs that operate around the 850 nm wavelength at room temperature, which necessitates the incorporation of PhC structures designed to amplify enhancements within this specific wavelength spectrum. The pitch and the dimensions of the nanoholes within the PhC structures play a pivotal role in defining the PBG characteristics. In the context of LIL, the pitch is inherently linked to the angle of incidence of the laser beam, while the dimensions of the nanoholes are influenced by the laser energy. An

excessively large pitch could diminish the PhC structure's capacity to enhance the emission efficiency at wavelengths characteristic of GaAs-based LEDs. Conversely, an overly small pitch could make the fabrication process more complex. To harmonize the operational wavelengths of GaAs-based devices with practical manufacturing approaches, an optimal laser incidence angle of 43° has been established. Additionally, a judicious selection of laser energy is imperative to avoid damaging the PhC pattern, with 9 mJ identified as the optimal energy level. At this setting, the nanoholes assume an elliptical configuration, as evidenced in the SEM images in Figure 5.2, where the ellipse's major and minor axes measure approximately 315 nm and 305 nm, respectively, and the pitch size is approximately 365 nm. These dimensions agree with the theoretical expectations based on the calculations outlined in the relevant equation.

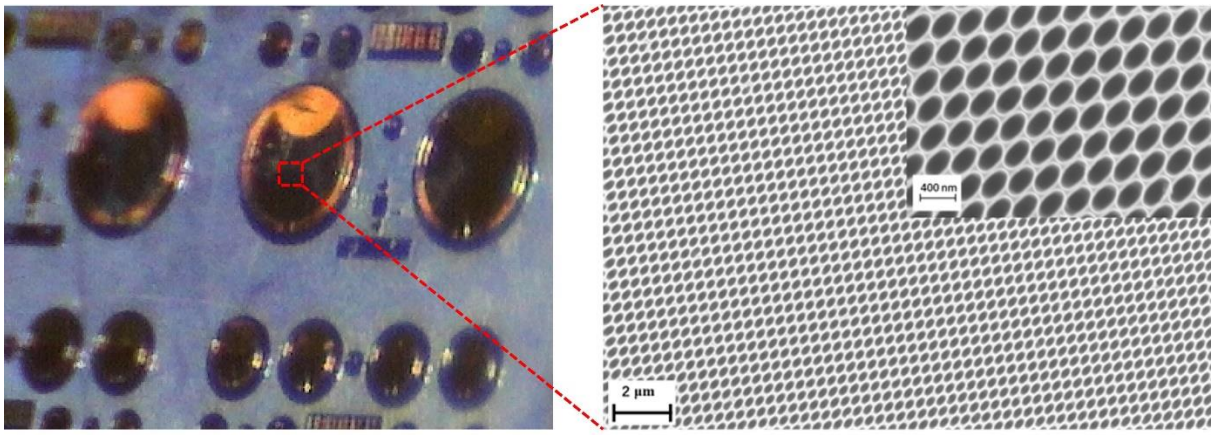

Figure 5.2. SEM images of the LED sample with PhC structures.

Figure 5.3 presents the results of a PBG simulation conducted using the FDTD technique, taking into account the dimensions and spacing of the nanoholes. The dispersion graph reveals the emergence of PBG within two distinct frequency bands, notably between normalized frequencies of 0.28 to 0.31 and 0.38 to 0.44. These frequency ranges correspond to the wavelength intervals of 830 nm to 960 nm and 1177 nm to 1303 nm, respectively. This indicates that the 2D PhC structure under analysis functions effectively as an out-coupler for TE modes, an essential feature for the enhancement of the performance of the LED samples in this study.

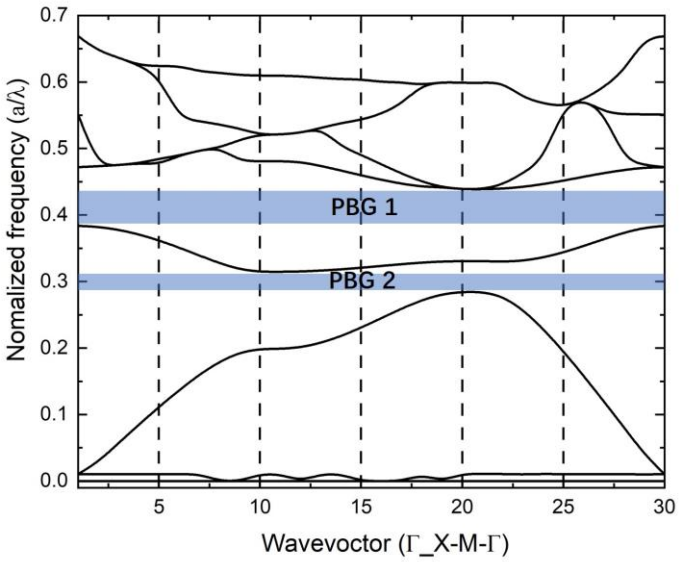

Figure 5.3. The PBG for the 2D PhC obtained from FDTD.

To investigate the impact of PhC structure depth on LEE enhancement in LEDs, a sequence of FDTD simulations was performed. These simulations, depicted in two-dimensional cross-sections in Figure 5.4, examined LEDs featuring PhC structures at various depths. Within the simulation, a dipole emitter was used to mimic the light-emitting source, strategically placed at the position corresponding to the MQW layer.

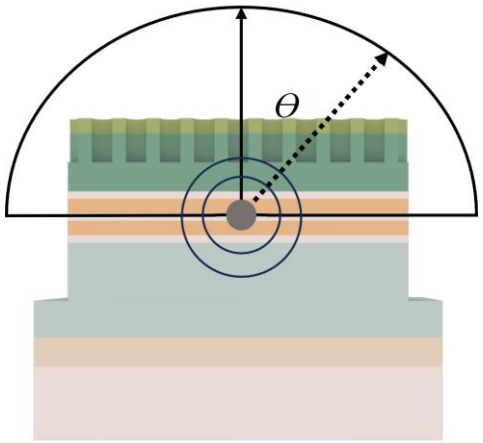

Figure 5.4. LED cross-sectional FDTD simulation schematic.

Figures 5.5 (a) through 5.5 (f) display the far-field angular distribution plots for LEDs with different PhC structure depths: one without a PhC structure, and others with depths of 100 nm, 200 nm, 300 nm, 400 nm, and 500 nm, respectively. In these figures, the bar indicates the light intensity, the horizontal axis denotes the light propagation direction, and the vertical axis reflects the light wavelength. Notably, the interaction of light with the PhC structure leads to constrained propagation for wavelengths outside the 830 nm to 960 nm range, a pattern that becomes increasingly evident in Figures 5.5 (c) to 5.5 (f).

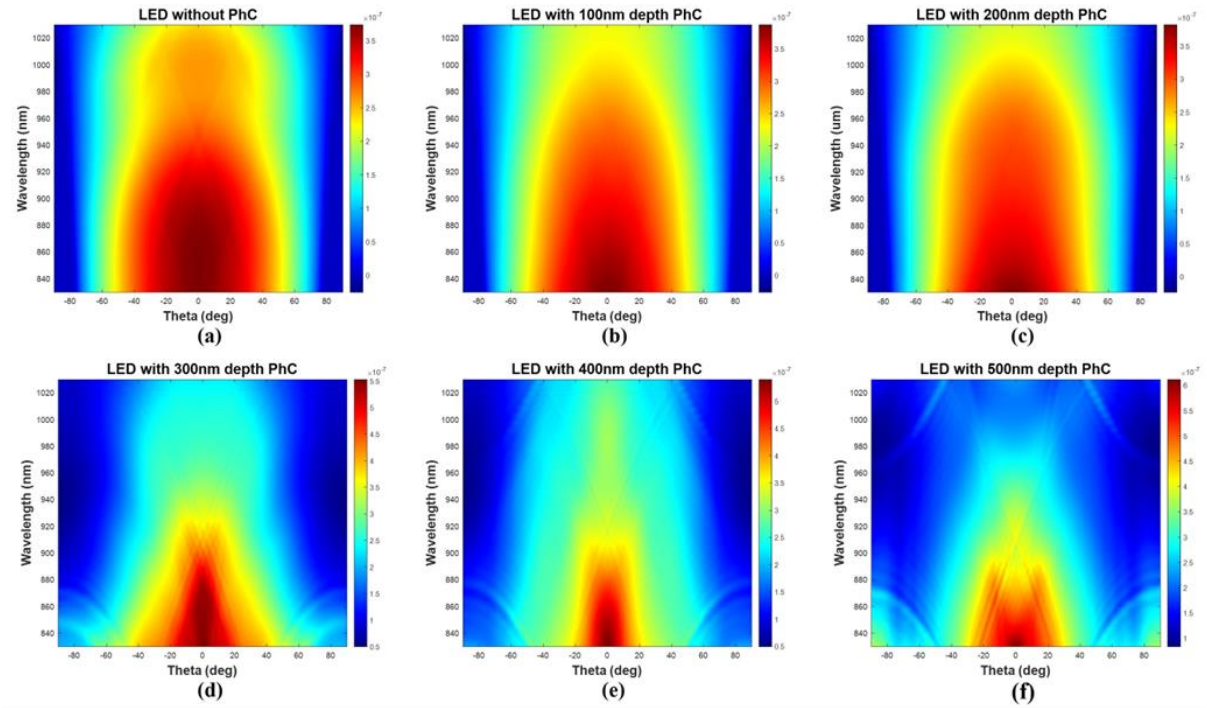

Figure 5.5. The far-field angular distribution plots for (a) LED without PhC structure, (b) 100 nm, (c) 200 nm, (d) 300 nm, (e) 400 nm, and (f) 500 nm depths of PhC structures on LEDs.

Figures 5.5 (b) and 5.5 (c) clarify that PhC structures with depths of 100 nm and 200 nm are insufficient for generating a pronounced photonic bandgap effect, leading to only a marginal improvement in LEE, as depicted in Figure 5.6. On the contrary, as shown in Figure 5.5 (d), an optimal depth for PhC structures strikes a delicate balance between proficient light manipulation and the reduction of losses attributable to absorption or scattering. Such an optimal depth capitalizes on the photonic bandgap effect to significantly enhance LEE (by an average factor of 1.3), a point underscored in Figure 5.6. However, as illustrated in Figures 5.5 (e) and 5.5 (f), PhC structures with greater depths, specifically 400 nm and 500 nm, fail to yield

additional enhancements. Instead, they induce diffraction limitations and intricate light interference patterns that can result in destructive interference and misdirect light at suboptimal angles. These deeper structures lead to more convoluted light pathways, which in turn cause internal light loss and diminish the overall light output efficiency. Thus, while a certain depth is indispensable for efficacious light manipulation, overly deep PhC structures may prove to be detrimental, as evidenced by the negligible LEE improvement observed with 400 nm and 500 nm depths in Figure 5.6.

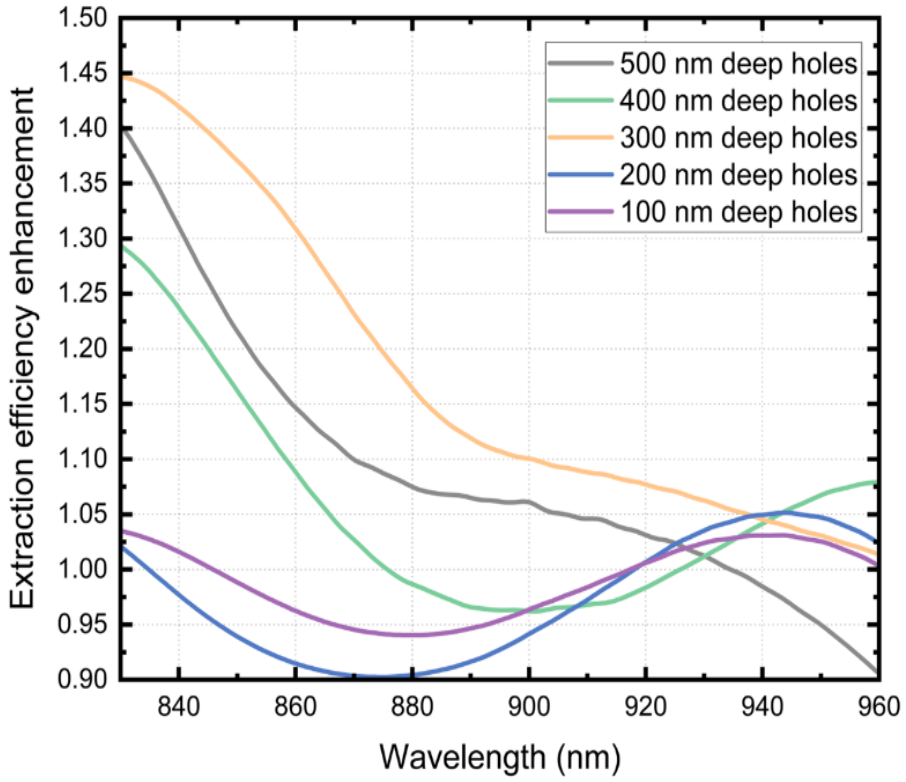

Figure 5.6. The relationship between LEE enhancement and wavelength of LEDs with different depth PhC structures.

5.3 Electroluminescence Results

Informed by the findings from our simulation studies, we have focused on optimizing the ICP etching process for PhC structures to a depth of approximately 300 nm. This etching is carried

out using a mixture of $SiCl_4$ and Ar_2 gases, maintaining an etching rate of 200 nm/min. Considering the photoresist layer thickness of 180 nm used in our experiments, we were cautious to avoid extended etching times that could potentially damage the integrity of the PhC structures. As a result, the LED samples in this study were subjected to ICP etching for durations of 60, 70, 80, 90, and 100 seconds.

To evaluate the effect of varying PhC structure depths on the LEE of LEDs, EL measurements were performed. These tests included LEDs with different depths of PhC structures as well as control samples without PhC structures. It is important to note that the etching depth for the PhC structures was deliberately kept at a significant distance from the MQW layer to ensure that the IQE of the LEDs remains largely unaffected, whether PhC structures are present. The similarity in the IV curves, as shown in Figure 5.7(a), confirms that incorporating PhC structures does not adversely affect the electrical performance of the diodes. The IV characteristics of the LEDs with various PhC depths and the conventional LED are very similar, displaying a turn-on voltage just above 2V and an exponential current increase in the forward bias region. The measurements indicate that the devices have minimal leakage current in the reverse bias region, suggesting high-quality diode junctions and stable performance. Additionally, the absence of reverse breakdown up to -2V further confirms the reliability of these LEDs under reverse bias conditions. These low dark current levels are beneficial for maintaining high efficiency and reducing noise in the LEDs, especially in applications requiring precise and stable light output. The photonic crystal structures do not adversely affect the dark current, making them suitable for enhancing the optical properties without compromising electrical performance.

Notably, AlGaAs/GaAs LEDs should exhibit smaller turn-on voltages at near IR wavelengths. However, our actual measurements deviate from this expectation. One contributing factor is the prolonged storage of our measurement probes. Poor contact between the probes and the LED leads can introduce additional resistance, resulting in elevated voltage readings.Moreover, as illustrated in Fig. 3.12 (a), the n-contact is plated on the backside of the substrate. During measurements, the sample is positioned on a gold-plated metal stage, with the two probes touching the n-contact on the sample's surface and the metal stage, respectively. This setup necessitates that the current flow path includes the entire substrate thickness (300 mm), increasing the path length and, consequently, the resistance. This added

resistance contributes to a higher turn-on voltage, diverging from the theoretically predicted values. Additionally, due to the various uncertainties associated with the measurement device, there is a concern about potential damage to the LED devices caused by excessive reverse voltages, such as avalanche breakdown. To mitigate this risk, reverse voltage is limited to a maximum of -2V during measurements.

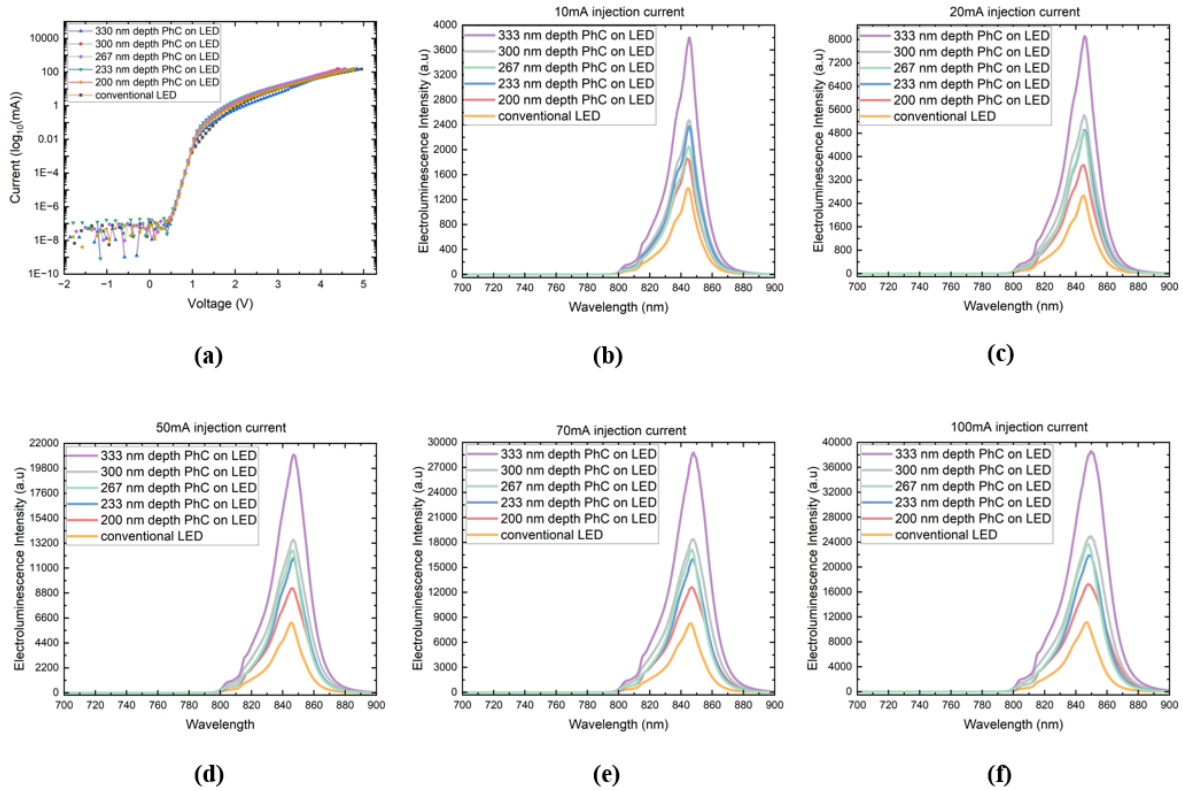

Figure 5.7. (a) The IV curves for LEDs with different depth PhC structures, (b) 10 mA, (c) 20 mA, (d) 50 mA, (e) 70 mA, (f) 100 mA injection current EL results for LEDs with different depth PhC structures.

Figures 5.7 (b) to 5.7 (f) show the EL profiles of LEDs equipped with PhC structures at various depths, juxtaposed with a standard LED, across different injection current settings (10, 20, 50, 70, 100 mA) at ambient temperature. An observable blueshift in the emission wavelength from 845 nm to 850 nm occurs with the increment of injection current from 10 mA to 100 mA, a shift predominantly attributed to the Burstein-Moss shift (BMS) [38]. Figures 5.8 (a) to 5.8 (f) illustrate the EL color fill contour profiles for LEDs with differing depths of PhC structures, compared to a conventional LED, under the same range of injection current conditions. These

visual representations elucidate the impact of variations in the depth of PhC structures on the EL properties of LEDs under various levels of electrical excitation.

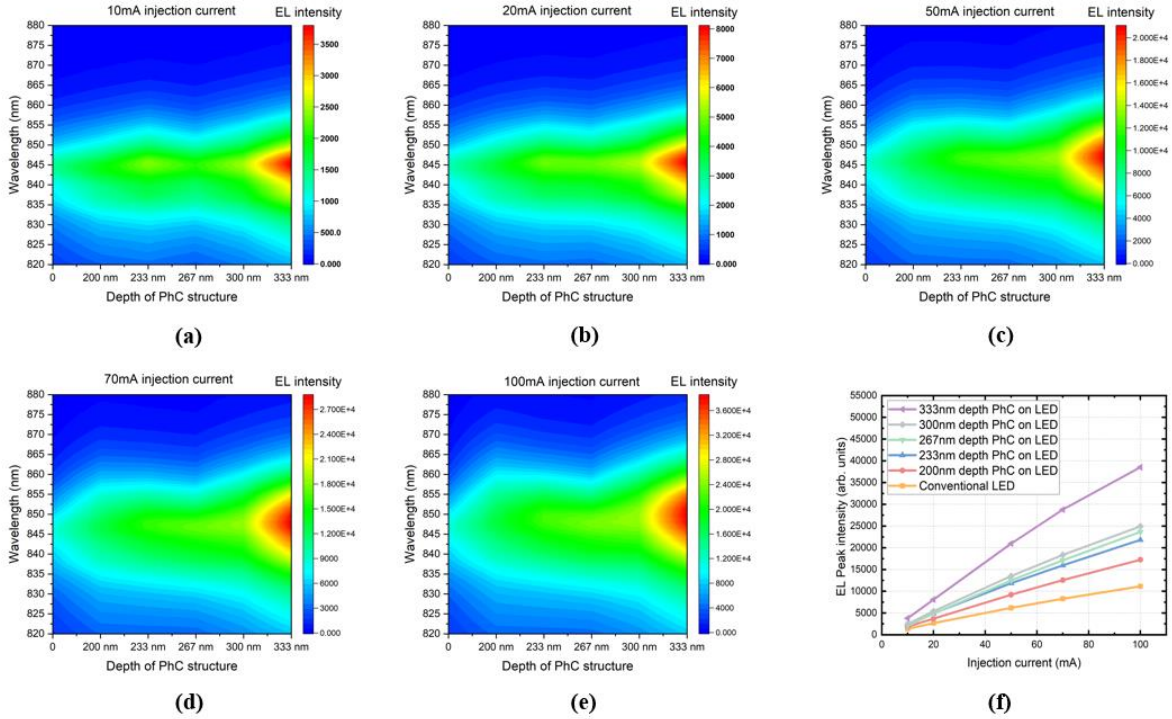

Figure 5.8. (a) 10 mA, (b) 20 mA, (c) 50 mA, (d) 70 mA, (e) 100 mA injection current EL colour fill contour pictures for LEDs with different depth PhC structures; (f) The relationship between EL peak intensity and injection current for conventional LED and LEDs with different depth PhC structures.

The observed enhancements in EL intensity are primarily ascribed to the improved LEE afforded by the integration of PhC structures, as the IQE of the LEDs remains essentially constant. This suggests that the increase in EL intensity is a direct result of the PhC structures' ability to enhance light extraction. This is supported by Figures 5.6 (b) to 5.6 (f), which consistently demonstrate that LEDs with PhC structures exhibit higher luminous intensity compared to standard LEDs under similar operational conditions. A more granular analysis, as depicted in Figure 5.8 (f). EL peak intensity is an effective metric for rapidly evaluating the maximum efficiency and comparing the peak performance of various LED structures, as illustrated in the graph. Although integrated EL intensity provides a comprehensive understanding of an LED's total light output, it presents several disadvantages, including measurement complexity, less intuitive data interpretation, and the influence of spectral

width. These drawbacks can reduce its practicality for quick performance assessments or applications where specific wavelength performance is critical. In our analysis, the full width at half maximum (FWHM) values differ slightly, but the wavelengths corresponding to the peaks remain consistent, with no emergence of new peaks. Consequently, the trends in EL peak intensity and integrated EL intensity do not show significant differences. In Figure 5.8(f) indicates that LEDs with a PhC depth of 200 nm exhibit an EL intensity increase, averaging a 1.5-fold enhancement. For PhC structures with depths of 233 nm, 267 nm, and 300 nm, there is a gradual increase in EL intensity enhancement, with average enhancements of 2-fold, 2.1-fold, and 2.15-fold, respectively. Notably, at a PhC depth of 333 nm, there is a significant leap in EL intensity, with an average increase factor of 3.5, highlighting the profound influence of PhC depth on the EL efficiency of LEDs.

5.4 Conclusion

In this study, we have developed and constructed PhC structures on LED substrates using nanosecond pulsed laser interference lithography, followed by pattern transfer via ICP etching. Our investigation focused on the effect of PhC structure depth on the LEE of GaAs/AlGaAs MQW LEDs, specifically those emitting at an 850 nm wavelength at room temperature. SEM analyses confirmed the high-quality fabrication of PhC structures on the LED samples, achieved through a three-beam single pulse LIL approach and precisely controlled ICP etching to adjust the etching depths. FDTD simulations were used to evaluate the PBG characteristics of the PhC structures, confirming their capacity to enhance light emission at the targeted 850 nm wavelength. Cross-sectional simulations of the LED structure identified an optimal nanohole depth of approximately 300 nm for maximal LEE enhancements. This finding was corroborated by EL measurements on LEDs with varying PhC depths, where a significant 3.5-fold increase in EL intensity was observed at a PhC depth of 333 nm, indicating a marked enhancement in light emission efficiency.

This research used a GaAs-based LED operating at 850 nm as a test model, a wavelength commonly employed in infrared illumination. However, the method is versatile and can be applied to various wavelengths and semiconductor materials by adjusting the three-beam single-pulse LIL configuration. This technique, characterized by its nanosecond-range exposure times, presents a high-throughput solution for creating nanoscale periodic arrays. When combined with rapid step-and-repeat stages, it offers a highly efficient and cost-effective fabrication method suitable for enhancing the luminous efficacy of LEDs across a broad spectrum of wavelengths.

References

[1] H. Lee *et al.*, “Structurally engineered colloidal quantum dot phosphor using TiO2 photonic crystal backbone,” *Light Sci Appl*, vol. 11, no. 1, Dec. 2022, doi: 10.1038/s41377-022-01020-2.

[2] S. M. Ko *et al.*, “Hexagonal GaN nanorod-based photonic crystal slab as simultaneous yellow broadband reflector and blue emitter for phosphor-conversion white light emitting devices,” *Sci Rep*, vol. 10, no. 1, Dec. 2020, doi: 10.1038/s41598-019-55684-9.

[3] D. Allemeier, B. Isenhart, E. Dahal, Y. Tsuda, T. Yoshida, and M. S. White, “Emergence and control of photonic band structure in stacked OLED microcavities,” *Nat Commun*, vol. 12, no. 1, Dec. 2021, doi: 10.1038/s41467-021-26440-3.

[4] K. Emoto *et al.*, “Wide-bandgap GaN-based watt-class photonic-crystal lasers,” *Commun Mater*, vol. 3, no. 1, Dec. 2022, doi: 10.1038/s43246-022-00288-6.

[5] Y. Yu, W. Xue, E. Semenova, K. Yvind, and J. Mork, “Demonstration of a self-pulsing photonic crystal Fano laser,” *Nat Photonics*, vol. 11, no. 2, pp. 81–84, Feb. 2017, doi: 10.1038/nphoton.2016.248.

[6] Y.-K. Wang *et al.*, “Self-assembled monolayer-based blue perovskite LEDs,” 2023. [Online]. Available: https://www.science.org

[7] A. M. Nahavandi, M. Safi, P. Ojaghi, and J. Y. Hardeberg, “LED primary selection algorithms for simulation of CIE standard illuminants,” *Opt Express*, vol. 28, no. 23, p. 34390, Nov. 2020, doi: 10.1364/oe.408754.

[8] X. Shen, A. Kamath, and P. Guyot-Sionnest, “Mid-infrared cascade intraband electroluminescence with HgSe–CdSe core–shell colloidal quantum dots,” *Nat Photonics*, vol. 17, no. 12, pp. 1042–1046, Dec. 2023, doi: 10.1038/s41566-023-01270-5.

[9] F. Yuan *et al.*, “Bright and stable near-infrared lead-free perovskite light-emitting diodes,” *Nat Photonics*, 2024, doi: 10.1038/s41566-023-01351-5.

[10] M. Ghali, K. Ohtani, Y. Ohno, and H. Ohno, “Generation and control of polarization-entangled photons from GaAs island quantum dots by an electric field,” *Nat Commun*, vol. 3, 2012, doi: 10.1038/ncomms1657.

[11] Y. Yao *et al.*, “A robust vertical nanoscaffold for recyclable, paintable, and flexible light-emitting devices,” 2022. [Online]. Available: https://www.science.org

[12] M. Woo Jeong *et al.*, “Intrinsically stretchable three primary light-emitting films enabled by elastomer blend for polymer light-emitting diodes,” 2023. [Online]. Available: https://www.science.org

[13] J. Park *et al.*, “Electrically driven mid-submicrometre pixelation of InGaN micro-light-emitting diode displays for augmented-reality glasses,” *Nat Photonics*, vol. 15, no. 6, pp. 449–455, Jun. 2021, doi: 10.1038/s41566-021-00783-1.

[14] C. Couteau *et al.*, “Applications of single photons to quantum communication and computing,” *Nature Reviews Physics*, vol. 5, no. 6. Springer Nature, pp. 326–338, Jun. 01, 2023. doi: 10.1038/s42254-023-00583-2.

[15] T. K. Hsiao *et al.*, “Single-photon emission from single-electron transport in a SAW-driven lateral light-emitting diode,” *Nat Commun*, vol. 11, no. 1, Dec. 2020, doi: 10.1038/s41467-020-14560-1.

[16] T. Müller *et al.*, “A quantum light-emitting diode for the standard telecom window around 1,550 nm,” *Nat Commun*, vol. 9, no. 1, Dec. 2018, doi: 10.1038/s41467-018-03251-7.

[17] Y. Zhou *et al.*, “Room temperature solid-state quantum emitters in the telecom range,” 2018. [Online]. Available: https://www.science.org

[18] Y. Yu *et al.*, “Telecom-band quantum dot technologies for long-distance quantum networks,” *Nature Nanotechnology*, vol. 18, no. 12. Nature Research, pp. 1389–1400, Dec. 01, 2023. doi: 10.1038/s41565-023-01528-7.

[19] K. Wang, X. Dong, Y. Bu, and X. Wang, “Design of photonic crystals for light-emitting diodes,” *Journal of the American Ceramic Society*, vol. 106, no. 12. John Wiley and Sons Inc, pp. 7146–7188, Dec. 01, 2023. doi: 10.1111/jace.19388.

[20] H. Hu *et al.*, “Boosted ultraviolet electroluminescence of InGaN/AlGaN quantum structures grown on high-index contrast patterned sapphire with silica array,” *Nano Energy*, vol. 69, Mar. 2020, doi: 10.1016/j.nanoen.2019.104427.

[21] P. Mao *et al.*, “Single-step-fabricated disordered metasurfaces for enhanced light extraction from LEDs,” *Light Sci Appl*, vol. 10, no. 1, Dec. 2021, doi: 10.1038/s41377-021-00621-7.

[22] E. Khaidarov *et al.*, “Control of LED Emission with Functional Dielectric Metasurfaces,” *Laser Photon Rev*, vol. 14, no. 1, Jan. 2020, doi: 10.1002/lpor.201900235.

[23] J. Chen, T. Wang, and X. Wang, “Enhancing light extraction efficiency of GaN LED by combining complex-period photonic crystals with doping,” *Journal of the American Ceramic Society*, vol. 106, no. 8, pp. 4752–4769, Aug. 2023, doi: 10.1111/jace.19122.

[24] L. Zhou *et al.*, “High-performance flexible organic light-emitting diodes using embedded silver network transparent electrodes,” *ACS Nano*, vol. 8, no. 12, pp. 12796–12805, Dec. 2014, doi: 10.1021/nn506034g.

[25] S. M. Lee, Y. Cho, D. Y. Kim, J. S. Chae, and K. C. Choi, “Enhanced Light Extraction from Mechanically Flexible, Nanostructured Organic Light-Emitting Diodes with Plasmonic Nanomesh Electrodes,” *Adv Opt Mater*, vol. 3, no. 9, pp. 1240–1247, Sep. 2015, doi: 10.1002/adom.201500103.

[26] M. L. Lee *et al.*, “Utilizing Two-Dimensional Photonic Crystals in Different Arrangement to Investigate the Correlation Between the Air Duty Cycle and the Light Extraction Enhancement of InGaN-Based Light-Emitting Diodes,” *IEEE Photonics J*, vol. 6, no. 3, Jun. 2014, doi: 10.1109/JPHOT.2014.2323304.

[27] T. Sridarshini and S. Indira Gandhi, “Photonic band structure of 2D photonic crystals - A comparative study,” *Laser Phys*, vol. 30, no. 2, 2020, doi: 10.1088/1555-6611/ab5795.

[28] D. Przybylski and S. Patela, “Modelling of a two-dimensional photonic crystal as an antireflection coating for optoelectronic applications,” *Opto-Electronics Review*, vol. 27, no. 1, pp. 79–89, Mar. 2019, doi: 10.1016/j.opelre.2019.02.004.

[29] X. Tang *et al.*, “Enhanced light extraction from AlGaInP-based red light-emitting diodes with photonic crystals,” *Opt Express*, vol. 29, no. 4, p. 5993, Feb. 2021, doi: 10.1364/oe.418944.

[30] L. Shterengas, R. Liu, A. Stein, G. Kipshidze, W. J. Lee, and G. Belenky, “Continuous wave room temperature operation of the 2 µm GaSb-based photonic crystal surface emitting diode lasers,” *Appl Phys Lett*, vol. 122, no. 13, Mar. 2023, doi: 10.1063/5.0137151.

[31] S. Hou *et al.*, “Concurrent Inhibition and Redistribution of Spontaneous Emission from All Inorganic Perovskite Photonic Crystals,” *ACS Photonics*, vol. 6, no. 6, pp. 1331–1337, Jun. 2019, doi: 10.1021/acsphotonics.8b01655.

[32] C. Wang *et al.*, “Discretely-supported nanoimprint lithography for patterning the high-spatial-frequency stepped surface,” *Nano Res*, vol. 14, no. 8, pp. 2606–2612, Aug. 2021, doi: 10.1007/s12274-020-3261-3.

[33] M. Modaresialam, Z. Chehadi, T. Bottein, M. Abbarchi, and D. Grosso, “Nanoimprint Lithography Processing of Inorganic-Based Materials,” *Chemistry of Materials*, vol. 33, no. 14. American Chemical Society, pp. 5464–5482, Jul. 27, 2021. doi: 10.1021/acs.chemmater.1c00693.

[34] D. Pudis *et al.*, “Effect of 2D photonic structure patterned in the LED surface on emission properties,” in *Applied Surface Science*, Elsevier B.V., 2013, pp. 161–165. doi: 10.1016/j.apsusc.2012.10.030.

[35] X. Tang *et al.*, “Enhancement of light extraction efficiency of AlGaInP-based light emitting diodes by silicon oxide hemisphere array,” *Opt Commun*, vol. 481, Feb. 2021, doi: 10.1016/j.optcom.2020.126539.

[36] P. Zuo *et al.*, “Improved optical and electrical performances of GaN-based light emitting diodes with nano truncated cone SiO2 passivation layer,” *Opt Quantum Electron*, vol. 48, no. 5, May 2016, doi: 10.1007/s11082-016-0551-9.

[37] Y. R. Wang, I. S. Han, C. Y. Jin, and M. Hopkinson, “Precise Arrays of Epitaxial Quantum Dots Nucleated by in Situ Laser Interference for Quantum Information Technology

Applications," *ACS Appl Nano Mater*, vol. 3, no. 5, pp. 4739–4746, May 2020, doi: 10.1021/acsanm.0c00738.

[38] S. Ni *et al.*, "Burstein-Moss shift of lead halide perovskite quantum dots induced by electron injection from graphene oxide," *Appl Surf Sci*, vol. 545, Apr. 2021, doi: 10.1016/j.apsusc.2021.149003.

Chapter 6

Optical Properties of Precise Arrays Quantum Rings by Direct Laser Interference Patterning

6.1 Introduction

Self-assembled quantum nanostructures (QNs) have attracted the attention of many researchers due to their excellent optical and electrical properties [1-8]. Especially for precisely arrayed self-assembled QNs, which hold promise for future technologies in photonics, and quantum information science due to their enhanced quantum confinement, scalability, cost-effectiveness, and customizable properties for specific applications. Quantum nanostructures, such as QDs and QRs, exhibit 3D confinement. QRs, in comparison to QDs, display unique energy levels that are influenced not only by their size but also by their topological structure. This difference also is caused by the Aharonov-Bohm (AB) effect, where a magnetic flux penetrating the center of a QR induces oscillations in its energy levels, offering an additional layer of control over qubit states through the application of a magnetic flux [9-11]. This unique characteristic of QRs, stemming from the AB effect, provides a novel degree of freedom in manipulating quantum states. They bring notable improvements to devices like quantum ring lasers, providing stable and energy-efficient operation with precise emission control; photodetectors, offering heightened sensitivity and reduced noise; and solar cells, where they improve efficiency through better charge carrier separation. Additionally, QRs enable the development of LEDs with improved color purity and efficiency and find

applications in quantum information processing and THz technology, showcasing their versatility and potential in next-generation optoelectronic technologies.

However, the practical fabrication of QRs presents considerable challenges, predominantly due to the complexities associated with crafting ring-like nanostructures that necessitate precise control over dimensions and the application of an external magnetic field to exploit the AB effect. The MBE (DE method) has been employed to synthesize QRs. The kinetics of crystallization, influenced by the flux of Group V elements and the crystallization temperature, play a pivotal role in determining the ultimate morphology and composition of the quantum structures, including GaAs QDs, and QRs. It has been observed that the crystallization process may proceed more rapidly at the periphery of the Ga droplet compared to its center. When the V/III ratio is high, the crystallization across the Ga droplet is efficient, potentially impeded by the abundant presence of As atoms, which may restrict the mobility of Ga atoms within the droplets, culminating in the formation of GaAs QDs with symmetrical shapes. Conversely, a lower V/III ratio results in a slower crystallization process due to the diminished bonding rate between Ga and As atoms, with crystal growth at the droplet edges outpacing that at the center, thus leading to the emergence of asymmetrically shaped GaAs QRs [12]. Further reduction in the intensity of the As flux diminishes the average height of the nanocrystals, giving rise to concentric double-ring structures [13]. At even lower As flux rates, triple-ring structures can be formed [14], and advancements in this methodology have led to the successful fabrication of structures comprising up to five concentric rings [15].

Despite the extensive literature on various growth methods for QDs, and QRs in semiconductor materials, the prevalent issue of their random distribution presents significant disadvantages, such as inhomogeneity in optical and electronic properties, challenges in device integration, and reduced scalability and reproducibility, thereby impacting their potential applications in nanotechnology and quantum devices. To improve this situation, researchers have employed a variety of innovative techniques, including EBL, NIL, and tip-assisted patterning [16-18]. These techniques are designed to precisely position QNs at predetermined locations through a series of fabrication steps, such as photolithography and etching. However, these pre-patterning and re-growth strategies often introduce defects as a consequence of the fabrication processes, potentially compromising the integrity of the QNs. To avoid these limitations, our approach has incorporated the use of a direct laser

interference lithography patterning (DLIP), which offers a more direct and potentially less defect-inducing method for structuring QNs. We have employed this technique before to produce precise arrays of single QDs [19], [20].

In this study, we propose to fabricate precisely arrayed GaAs QRs utilizing the DLIP technique during MBE epitaxial growth. The structural parameters, including pitch, size, and dimensions of the QR arrays, will be analyzed through AFM. Furthermore, to evaluate the optical properties of the QRs, comprehensive analyses will be conducted using both temperature-dependent and power-dependent PL techniques. Preliminary assessments indicate that the DLIP technique can achieve precise QR arrays without compromising the intrinsic characteristics of the QRs, suggesting a promising avenue for the development of advanced optoelectronic devices.

6.2 Experimental Details

In this work, we used a 2-inch semi-insulating GaAs (100) face wafer as the substrate. After the substrate was transferred into the MBE chamber, epitaxial growth was performed via the DE method. The epitaxial process commenced with the deposition of a 300 nm thick GaAs buffer layer, followed by the growth of a 100 nm $Al_{0.3}Ga_{0.7}As$ barrier layer on the substrate's surface. Thereafter, an in situ single 7 ns pulse DLIP technique was applied to the surface of the $Al_{0.3}Ga_{0.7}As$ barrier layer, employing a laser fluence range of 27 mJ/cm^2.

For the DLIP process, the 355 nm wavelength light was divided into four beams using a beam splitter and subsequently introduced into the MBE chamber through four symmetrical optical windows, each beam entering at an incidence angle of 58 degrees. The specific parameters of this experiment are detailed in our previous publications [19], [20]. These beams then reconverged at the center of the $Al_{0.3}Ga_{0.7}As$ barrier layer surface. Following the DLIP treatment, Ga was injected to form Ga droplets, which subsequently transformed into GaAs quantum rings in an As_2-rich environment. This was followed by the growth of a 20 nm $Al_{0.3}Ga_{0.7}As$ capping layer over the quantum rings. The process was concluded with the

addition of an 80 nm $Al_{0.3}Ga_{0.7}As$ barrier layer and a final 10 nm GaAs capping layer. The comprehensive structure of this assembly is depicted in Figure 6.1.

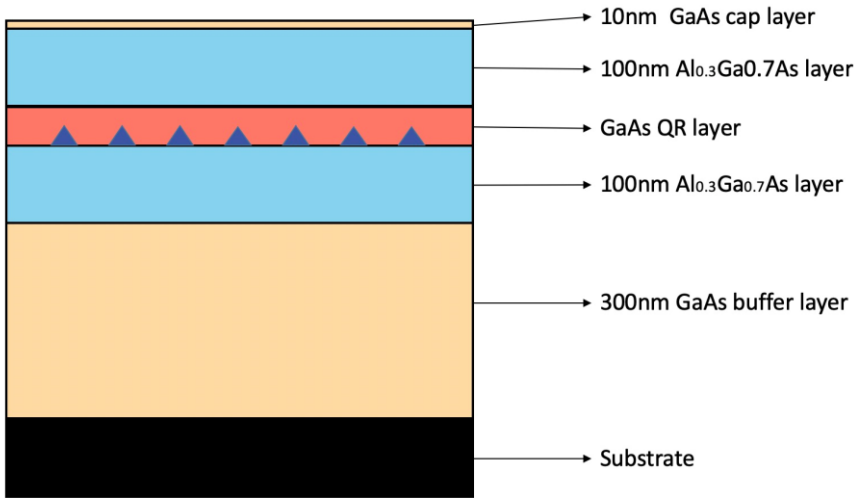

Figure 6.1. Schematic cross-sectional illustrations of GaAs/$Al_{0.3}Ga_{0.7}As$ QRs structure.

6.3 Morphological Characterization

AFM analysis was used to examine the surface characteristics of the quantum rings, with the results presented in Figure 6.2. The AFM image in Figure 6.2 (a) was obtained through a scanning area of 3 μm x 3 μm. Figure 6.2 (b) provides a three-dimensional representation of Figure 6.2 (a), illustrating the quantum rings positioned as pre-determined by the DLIP system. From the AFM imagery, a quantum ring spacing of 300 nm was discerned. Incorporating the incidence angle of the four beams post-beam splitter, as discussed in Chapter 2, a theoretical pitch of 300 nm between quantum rings was deduced. Consequently, it can be inferred that the DLIP system effectively facilitates precise periodic alignment of the quantum rings, as evidenced by the congruence between the theoretical predictions and the observed AFM results.

The AFM map of a 1.5 μm X 1.5 μm quantum ring is shown in Fig 6.2 (c). A single quantum ring from this figure was selected at random for cross-sectional analysis, and its profile is

illustrated in Fig 6.2 (d). From this analysis, it is inferred that the quantum ring exhibits a height of approximately 2 nm, an internal diameter of about 45 nm, and an overall diameter of about 110 nm.

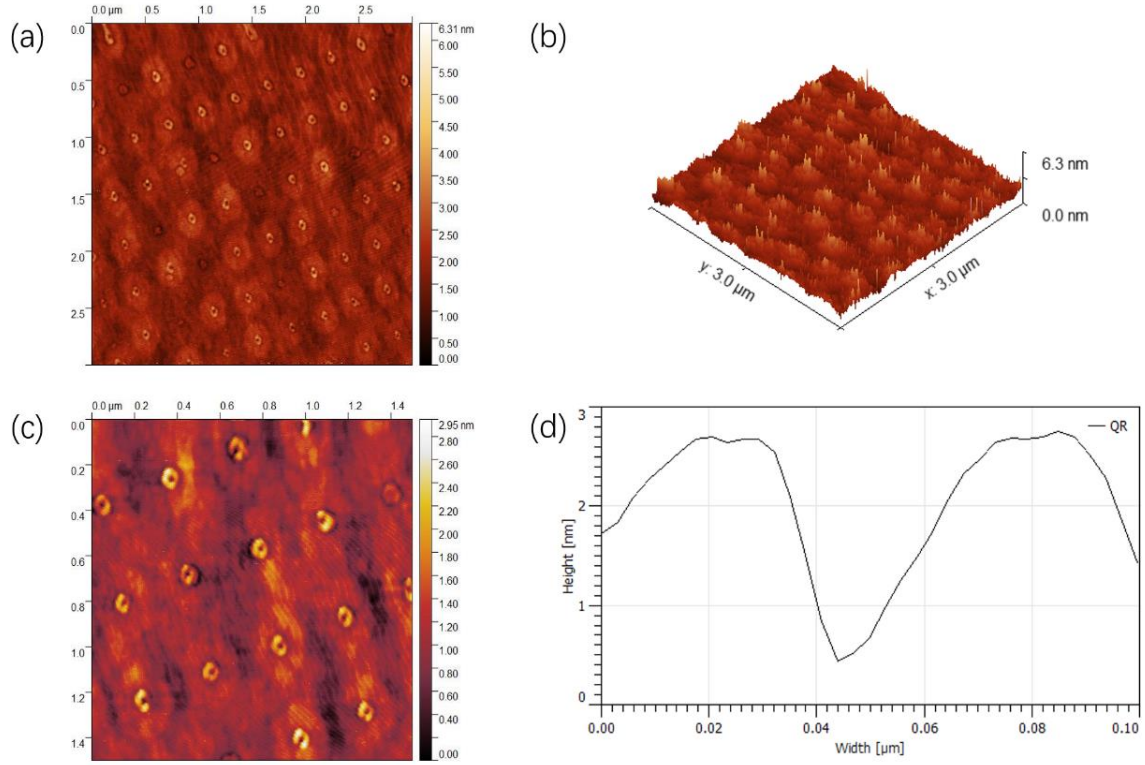

Figure 6.2. (a) AFM image (3 X 3 μm^2), (b) 3-D AFM image (3 X 3 μm^2) (QRs), (c) AFM micrographs (1.5 X 1.5 μm^2) of GaAs/$Al_{0.3}Ga_{0.7}As$ QRs. (d) The cross-sectional profiles of a single quantum ring.

6.4 Optical Characterization

The PL spectra of GaAs QRs are shown in Figure 6.3, obtained at a measurement temperature of 55 K and under an excitation laser power of 1 µW. The focused laser spot diameter on the sample's surface measures 2 µm. According to AFM analyses, the pitch is approximately 300 nm, facilitating the estimation of roughly 28 QRs encompassed within the area of measurement, with the excitation power density being $3X10^{-2}$ kW/cm^2.

Lower temperatures provide significant advantages for PL measurements in semiconductor materials. Reduced thermal quenching at low temperatures enhances radiative recombination, resulting in higher PL intensity and better detection of emissions from impurity states and quantum structures. Additionally, lower temperatures minimize phonon interactions, leading to narrower emission peaks and increased spectral resolution, which allows for more precise identification of emission origins. The suppression of non-radiative pathways and phonon-assisted processes further clarifies the PL spectra, making it easier to identify defect and impurity states. Moreover, the improved signal-to-noise ratio at lower temperatures enhances the detection of weak signals, providing more accurate and reliable data. Lastly, the stabilization of bandgap energy at reduced temperatures allows for precise measurement of band-edge transitions and intrinsic material properties. These benefits make low-temperature PL an essential tool for investigating the electronic structure, defect states, and overall quality of semiconductor materials. Due to the limitations of the experimental equipment, our cooling system can only lower the temperature to a maximum of 55k.

As illustrated in Figure 6.3, the PL spectra exhibit three distinct peaks: a broad peak centered around 715 nm, and two sharper peaks positioned at 818 nm and 830 nm, respectively. Emission wavelengths spanning from 812 nm to 823 nm are attributed to intrinsic GaAs transitions, whereas emissions from 825 nm to 836 nm are associated with carbon-related impurities [21], [22]. Carbon introduces acceptor states and potentially deeper defect levels that can modify the PL emission characteristics. The peak at 825 nm likely corresponds to near-band-edge recombination influenced by shallow acceptor states, while the peak at 836 nm might be related to deeper carbon-related defect levels or complex acceptor states within the bandgap. A clear decrease in the intensity of these peaks with increasing temperature, shown in Figure 6.5 (a), eventually leading to their disappearance, supports the idea that these peaks are associated with shallow acceptor states or defect levels introduced by carbon impurities. In addition, If the peaks were due to other mechanisms, such as intrinsic defects or complex centers not related to carbon, different temperature-dependent behaviors might be observed, including the possible emergence of new peaks or shifts in existing ones. Meanwhile, the broad peak featuring a shoulder on the PL spectrum's left side is ascribed to the nanostructured quantum rings.

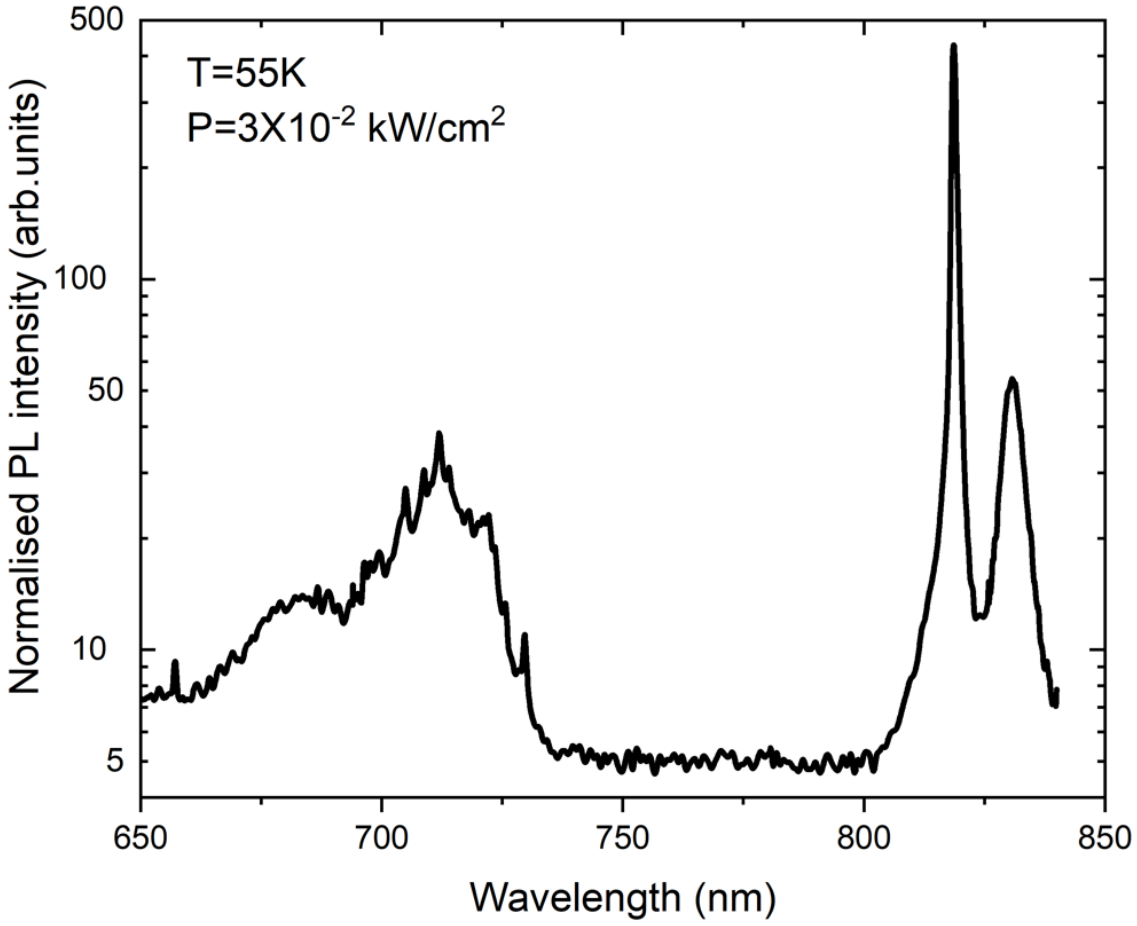

Figure 6.3. GaAs/$Al_{0.3}Ga_{0.7}As$ QRs PL spectra at 55 K with 3 X 10^{-2} kW/cm^2 excitation power density.

The PL spectra of $Al_{0.3}Ga_{0.7}As$/GaAs quantum ring structures, contingent upon varying excitation power densities, were examined and delineated in Figure 6.4 (a), illustrating the spectra as a function of normalized PL intensity at a temperature of 55 K. A dataset comprising seven distinct measurements was acquired across a spectrum of power densities, ranging from 3 X 10^{-1} kW/cm^2 to 1.5 X 10^{1} kW/cm^2. Figure 6.4 (b) specifically elucidates the behavior of peak emissions within the quantum rings, while Figures 6.4 (c), (d), and (e) present the extracted data for peak positions, FWHM, and normalized PL intensity, respectively.

An observable augmentation in peak intensities within Figure 6.4 (a) correlates with the increase in excitation energy. Figure 6.4 (e) shows a nearly linear enhancement in the normalized PL intensity of the quantum rings with escalating power densities. Notably, an emergent peak becomes discernible at power densities exceeding 3 kW/cm^2, situated at approximately 845 nm, attributed to impurity. Analysis of Figure 6.4 (c) reveals a progressive

shift in peak positions toward shorter wavelengths (UV region), indicative of a blueshift phenomenon. This shift spans from 714.6 nm to 709 nm, concomitant with a fiftyfold increase in power density from 3 X 10^{-1} kW/cm^2 to 1.5 X 10 kW/cm^2, potentially ascribed to quantum confinement effects. Furthermore, Figure 6.4 (d) documents the FWHM values for the aggregate peaks of the quantum rings, where the linewidth expands from 50 nm to 88.3 nm with the power density elevation from 3 X 10^{-1} kW/cm^2 to 1.5 X 10^{1} kW/cm^2. It is noteworthy that the rate of increase in FWHM values decelerates with rising power density.

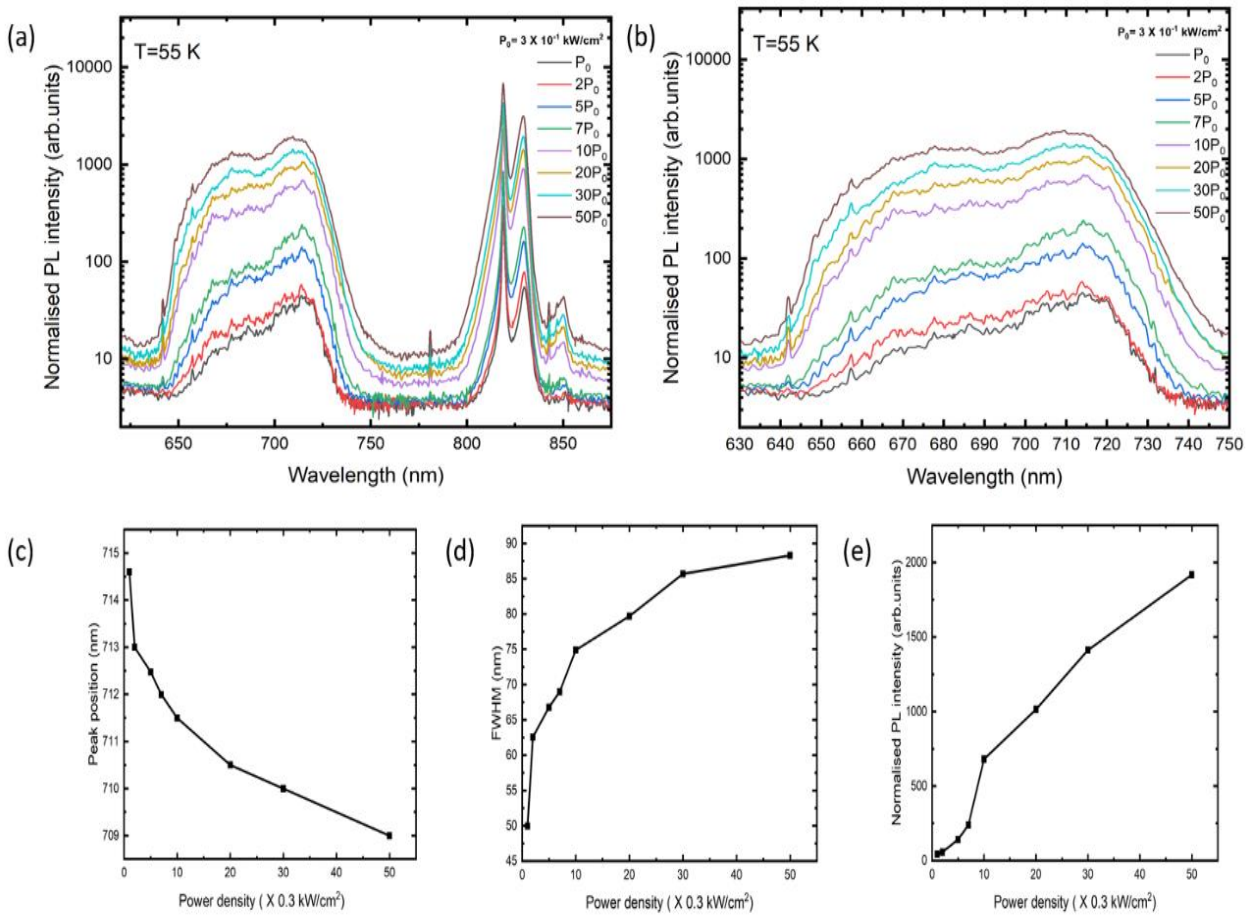

Figure 6.4. Power-dependent PL (a) full spectra of $Al_{0.3}Ga_{0.7}As$ / GaAs QRs and (b) $Al_{0.3}Ga_{0.7}As$ / GaAs QRs peaks are measured at T=55 K as a function of the power density. (c) The peak position, (d) FWHM, and (e) Normalized PL intensity of the QRs extracted as functions of the power density.

To determine the temperature-dependent PL characteristics of GaAs QRs, PL spectroscopy was conducted over a temperature range of 60 K to 100 K, employing a constant excitation power density of 3 X 10^{-1} kW/cm^2. This analysis result is shown in Figure 6.5 (a). Figure 6.5 (b)

concentrates on the PL emission features attributable to the QRs, offering a detailed view of the spectral region of interest. Figure 6.5 (c) delineates the evolution of the QRs PL peak positions as a function of temperature, revealing a redshift from 712 nm to 719 nm as the temperature increased from 60 K to 100 K. This spectral shift, amounting to 7 nm, is primarily attributed to the thermally induced alterations in carrier recombination dynamics within the QRs.

In addition, the FWHM of the QRs PL peaks was presented in Figure 6.5 (d). A notable contraction in FWHM from 54 nm at 60 K to 24 nm at 100 K was observed, indicative of a narrowing of the emission linewidth with temperature elevation. This phenomenon is particularly pronounced in the transition from 60 K to 70 K, where the linewidth experiences a substantial reduction of approximately 20 nm. The underlying mechanism for this linewidth narrowing is conjectured to be linked to the AB effect, which is known to induce oscillatory behavior in the electronic energy levels of QRs under the influence of a magnetic field. At lower temperatures, where quantum phase coherence is more robust, these energy level oscillations can manifest as discernible features in the PL spectrum, reflecting the magnetic flux-dependent modulation of electronic states.

Furthermore, Figure 6.5 (e) presents the temperature dependence of the normalized PL intensities of the QRs. A linear decrement in normalized PL intensity from 59 at 60 K to 13 at 100 K was observed, illustrating the inverse relationship between PL intensity and temperature. This trend is likely due to enhanced non-radiative recombination processes at elevated temperatures.

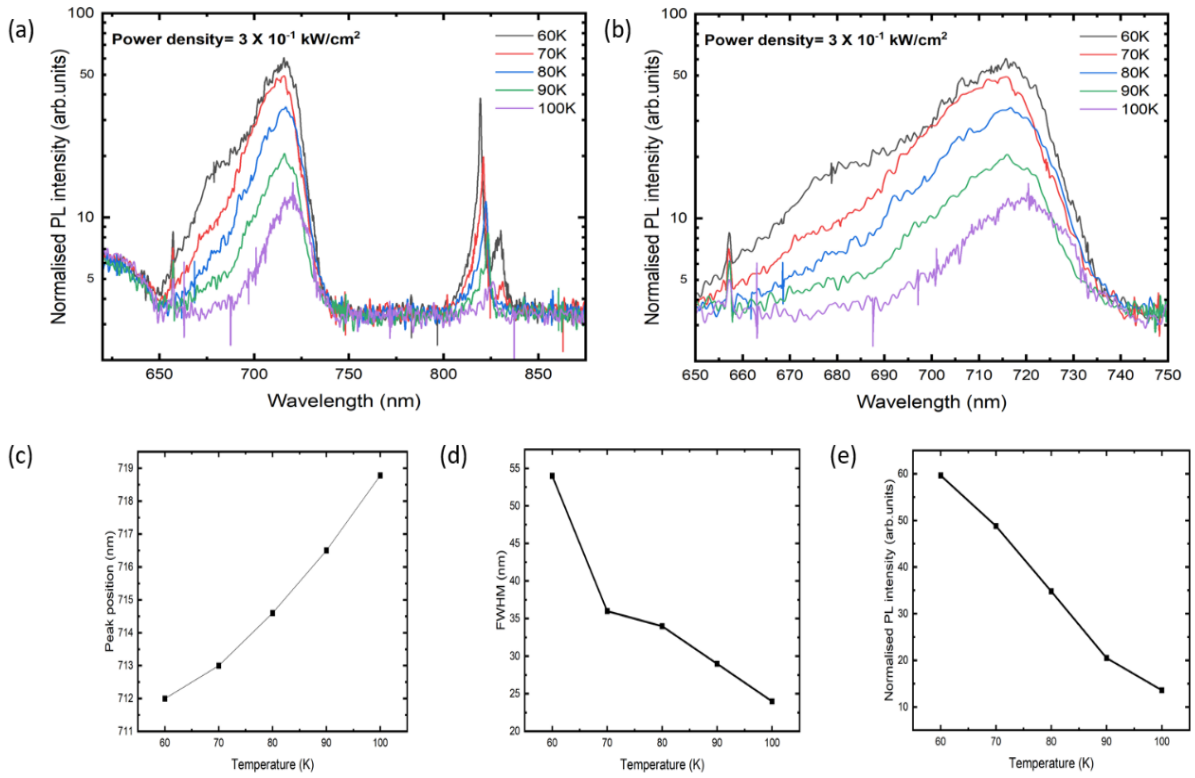

Figure 6.5. Temperature-dependent PL (a) full spectra of $Al_{0.3}Ga_{0.7}As$ / GaAs QRs and (b) $Al0.3Ga_{0.7}As$ / GaAs QRs peaks measured at an excitation laser intensity of 3 X 10^{-1} kW/cm^2. (c) The peak position, (d) FWHM, and (e) Normalised PL intensity of QR peak are plotted as a function of temperature.

6.5 Conclusion

In this study, precisely arrayed GaAs QRs were achieved by the DLIP technique during the MBE epitaxial growth process. AFM analyses were conducted to ascertain the structural integrity and alignment of the QRs. The results revealed a well-defined structure of periodically aligned QRs with a uniform pitch of 300 nm, indicating the efficacy of the DLIP method in achieving precision alignment. PL spectroscopy was employed to evaluate the optical properties of the QRs. The findings suggest that the DLIP method preserves the optical qualities of the QRs. In the analysis of power-dependent photoluminescence, an increase in excitation power correlates with a rise in luminescence intensity. Moreover, the temperature-dependent PL studies revealed a noteworthy phenomenon; a distinct shoulder peak emerged at lower temperatures, attributable to the AB effect, a characteristic unique to the quantum ring

structures. The implications of these findings are significant, suggesting that the DLIP method holds considerable promise for the precise alignment of QRs without compromising their optical and quantum mechanical properties. This advancement opens new avenues for the fabrication of quantum devices, where precision alignment is crucial for optimizing performance and harnessing quantum effects for applications in quantum computing, optoelectronics, and nanophotonics.

Reference

[1] R. Yuan *et al.*, "A composite electrodynamic mechanism to reconcile spatiotemporally resolved exciton transport in quantum dot superlattices," 2023. [Online]. Available: https://www.science.org

[2] H. Min *et al.*, "Spin coating epitaxial heterodimensional tin perovskites for light-emitting diodes," *Nat Nanotechnol*, 2024, doi: 10.1038/s41565-023-01588-9.

[3] F. Grillot, J. Duan, B. Dong, and H. Huang, "Uncovering recent progress in nanostructured light-emitters for information and communication technologies," *Light: Science and Applications*, vol. 10, no. 1. Springer Nature, Dec. 01, 2021. doi: 10.1038/s41377-021-00598-3.

[4] H. Tahara, M. Sakamoto, T. Teranishi, and Y. Kanemitsu, "Coherent electronic coupling in quantum dot solids induces cooperative enhancement of nonlinear optoelectronic responses," *Nat Nanotechnol*, 2024, doi: 10.1038/s41565-024-01601-9.

[5] D. Zhang *et al.*, "Large-scale planar and spherical light-emitting diodes based on arrays of perovskite quantum wires," *Nat Photonics*, vol. 16, no. 4, pp. 284–290, Apr. 2022, doi: 10.1038/s41566-022-00978-0.

[6] Z. Y. AbuWaar, Y. I. Mazur, J. H. Lee, Z. M. Wang, and G. J. Salamo, "Optical behavior of GaAs/AlGaAs ringlike nanostructures," *J Appl Phys*, vol. 101, no. 2, 2007, doi: 10.1063/1.2425194.

[7] J. S. Kim, "Investigation of various optical transitions in GaAs/Al0.3Ga0.7As double quantum ring grown by droplet epitaxy," *Physica Status Solidi - Rapid Research Letters*, vol. 10, no. 9, pp. 696–702, Sep. 2016, doi: 10.1002/pssr.201600171.

[8] C. Chen, X. Luo, A. E. K Kaplan, M. G. Bawendi, R. J. Macfarlane, and M. Bathe, "Ultrafast dense DNA functionalization of quantum dots and rods for scalable 2D array fabrication with nanoscale precision," 2023. [Online]. Available: https://www.science.org

[9] M. Bayer, M. Korkusinski, P. Hawrylak, T. Gutbrod, M. Michel, and A. Forchel, “Optical Detection of the Aharonov-Bohm Effect on a Charged Particle in a Nanoscale Quantum Ring,” *Phys Rev Lett*, vol. 90, no. 18, p. 4, 2003, doi: 10.1103/PhysRevLett.90.186801.

[10] A. O. Govorov, S. E. Ulloa, K. Karrai, and R. J. Warburton, “Polarized excitons in nanorings and the optical Aharonov-Bohm effect,” *Phys Rev B Condens Matter Mater Phys*, vol. 66, no. 8, pp. 813091–813094, Aug. 2002, doi: 10.1103/PhysRevB.66.081309.

[11] N. A. J. M. Kleemans *et al.*, “Oscillatory persistent currents in self-assembled quantum rings,” *Phys Rev Lett*, vol. 99, no. 14, Oct. 2007, doi: 10.1103/PhysRevLett.99.146808.

[12] J. Kim *et al.*, “Different shape of GaAs quantum structures under various growth conditions,” in *Thin Solid Films*, Sep. 2010, pp. 6500–6504. doi: 10.1016/j.tsf.2010.03.151.

[13] T. Kuroda *et al.*, “Optical transitions in quantum ring complexes,” *Phys Rev B Condens Matter Mater Phys*, vol. 72, no. 20, Nov. 2005, doi: 10.1103/PhysRevB.72.205301.

[14] M. Abbarchi *et al.*, “Micro-photoluminescence of GaAs/AlgaAs triple concentric quantum rings,” *Nanoscale Res Lett*, vol. 6, pp. 1–5, 2011, doi: 10.1186/1556-276X-6-569.

[15] C. Somaschini, S. Bietti, N. Koguchi, and S. Sanguinetti, “Fabrication of multiple concentric nanoring structures,” *Nano Lett*, vol. 9, no. 10, pp. 3419–3424, Oct. 2009, doi: 10.1021/nl901493f.

[16] J. S. Kim, M. Kawabe, and N. Koguchi, “Ordering of high-quality InAs quantum dots on defect-free nanoholes,” *Appl Phys Lett*, vol. 88, no. 7, 2006, doi: 10.1063/1.2174097.

[17] J. Skiba-Szymanska *et al.*, “Narrow emission linewidths of positioned InAs quantum dots grown on pre-patterned GaAs(100) substrates,” *Nanotechnology*, vol. 22, no. 6, Feb. 2011, doi: 10.1088/0957-4484/22/6/065302.

[18] J. Tommila, A. Schramm, T. V. Hakkarainen, M. Dumitrescu, and M. Guina, “Size-dependent properties of single InAs quantum dots grown in nanoimprint lithography patterned GaAs pits,” *Nanotechnology*, vol. 24, no. 23, Jun. 2013, doi: 10.1088/0957-4484/24/23/235204.

[19] Y.-R. Wang, S. M. Olaizola, I. S. Han, C.-Y. Jin, and M. Hopkinson, “Direct patterning of periodic semiconductor nanostructures using single-pulse nanosecond laser interference,” *Opt Express*, vol. 28, no. 22, p. 32529, Oct. 2020, doi: 10.1364/oe.397709.

[20] Y. R. Wang, I. S. Han, C. Y. Jin, and M. Hopkinson, “Precise Arrays of Epitaxial Quantum Dots Nucleated by in Situ Laser Interference for Quantum Information Technology Applications,” *ACS Appl Nano Mater*, vol. 3, no. 5, pp. 4739–4746, May 2020, doi: 10.1021/acsanm.0c00738.

[21] X. Mei *et al.*, “Highly-ordered GaAs/AlGaAs quantum-dot arrays on GaAs (001) substrates grown by molecular-beam epitaxy using nanochannel alumina masks,” *Appl Phys Lett*, vol. 82, no. 6, pp. 967–969, Feb. 2003, doi: 10.1063/1.1544065.

[22] T. Mano, K. Watanabe, S. Tsukamoto, H. Fujioka, M. Oshima, and N. Koguchi, “Fabrication of InGaAs quantum dots on GaAs(0 0 1) by droplet epitaxy,” 2000.

Chapter 7

Conclusion and Future Works

7.1 Conclusion

In conclusion, the research presented in this paper successfully demonstrates the capability of single-pulse LIL in fabricating PhC structures on GaAs and GaAs-based LEDs. The analysis of SEM and AFM results confirms that the PhC structures created via single pulse LIL exhibit remarkable periodicity across extensive areas, indicating the technique's precision and scalability. Furthermore, the experimental data provided within this study highlight the significant enhancement in optical device performance attributable to the PhC structures, particularly in terms of GaAs-based LEDs.

While the focus of this thesis has been primarily on the LEE enhancement in GaAs LEDs, the potential applications of single pulse LIL extend beyond this material and device type. Previous research within the field has illustrated the feasibility of implementing PhC structures across a diverse range of semiconductor materials and devices. However, the application of single-pulse LIL as described in our research remains unprecedented, marking a novel contribution to the field of semiconductor device fabrication.

Compared to alternative methods (EBL, NIL), single pulse LIL offers several distinct advantages, including reduced fabrication costs, increased throughput due to its rapid processing capabilities, and the ability to pattern large areas with high fidelity, making it an attractive option for industrial-scale production. These benefits, coupled with the demonstrated improvements in device performance, underscore the value of further exploring and optimizing single pulse LIL for the development of advanced semiconductor devices.

In addition to the photoresist method, it is also possible to create patterns directly on semiconductor materials using the single pulse LIL method under certain conditions (high temperature, high pressure), such as those mentioned in Chapter 6. Single-pulse LIL is used in conjunction with the MBE system to directly inscribe patterns onto the surface of the sample as it grows, initiating a localized interaction between the laser and material. This interaction can alter the diffusion on the surface. As a result, arrays of nano islands, each just a monolayer in height, are formed on the surface, providing energetically favorable sites for the nucleation of QDs or QRs. Consequently, this method has enabled the formation of precisely ordered QD nanostructures.

By pushing the boundaries of conventional nanofabrication techniques, this study contributes valuable insights into the field of photonic device development, encouraging further exploration and optimization of single-pulse LIL to unlock new dimensions of semiconductor device functionality and efficiency.

7.2 Future Work

7.2.1 PhC structure on GaAs solar cell

As delineated in Chapter 4, the implementation of our PhC structure on the surface of GaAs markedly decreases its reflectivity, thereby enhancing the ingress of light into the GaAs wafer. This increase is particularly beneficial when applied to the surface of GaAs-based solar cells, where it significantly bolsters the cell's efficiency in light absorption.

However, it is pertinent to note that the diameter of the pattern generated by our LIL exceeds 2 mm. While this dimension is adequate for applications in LEDs, it falls short of the requirements for solar cell devices, which typically measure 1 cm by 1 cm. To solve this, it necessitates a modification to our experimental setup, incorporating a motorized stage

capable of both horizontal and vertical directional movement to facilitate the sequential exposure of adjacent areas by displacing the stage by 2 mm after each exposure cycle.

During our experimentation, when sequential exposures were conducted at two distinct points on a sample separated by a certain distance, the development process revealed not only the intended patterns at the exposure sites but also an emergent pattern in the intervening space. This phenomenon suggests that the area between the two points does not suffice to prevent pattern formation after a single exposure; however, the accumulation of effects from multiple exposures leads to the manifestation of a pattern. To address this, an experimental adjustment was made by employing a silicon wafer to partially mask the sample, thus exposing only the desired area. Subsequently, the initially exposed sections were masked, and a second exposure was administered. This approach yielded pristine patterns devoid of any unintended interference between the exposure points. Accordingly, the fabrication of a shielding plate equipped with a 2 mm by 2 mm aperture may be advisable to facilitate precise and localized exposure.

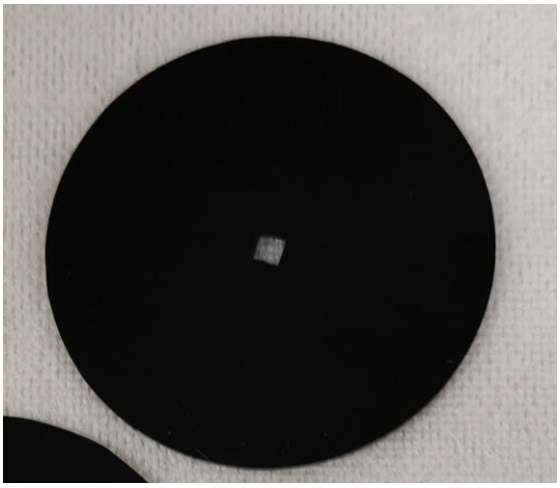

Figure 7.1. acrylic plate with a 2 mm by 2 mm aperture.

An initial experiment involved creating an aperture in an acrylic plate as illustrated in Figure 7.1. However, a subsequent issue was encountered. Given that the angle of incidence of our laser does not align perfectly at 180 degrees, the substantial thickness of the acrylic plate posed a risk of obstructing the laser beam, as depicted in Figure 7.2. Secondly, acrylic tends to be melted by the laser after many uses. We need to reconsider the setup.

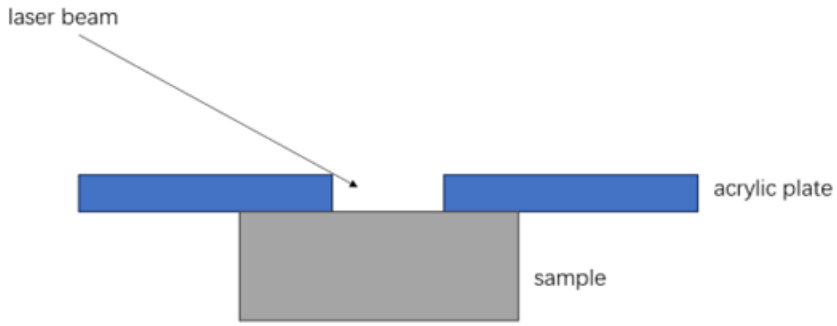

Figure 7.2. Laser beam Lithography Schematic.

7.2.2 Other PhC Structural Fabrication

Materials such as Indium Tin Oxide (ITO) and Titanium Dioxide (TiO_2) are frequently utilized in the fabrication of semiconductor devices due to their unique electrical and optical properties. In developing Photonic Crystal (PhC) structures within these materials, the conventional Inductively Coupled Plasma (ICP) etching technique is not viable. To illustrate, let us consider the fabrication of a PhC structure in ITO as a case study.

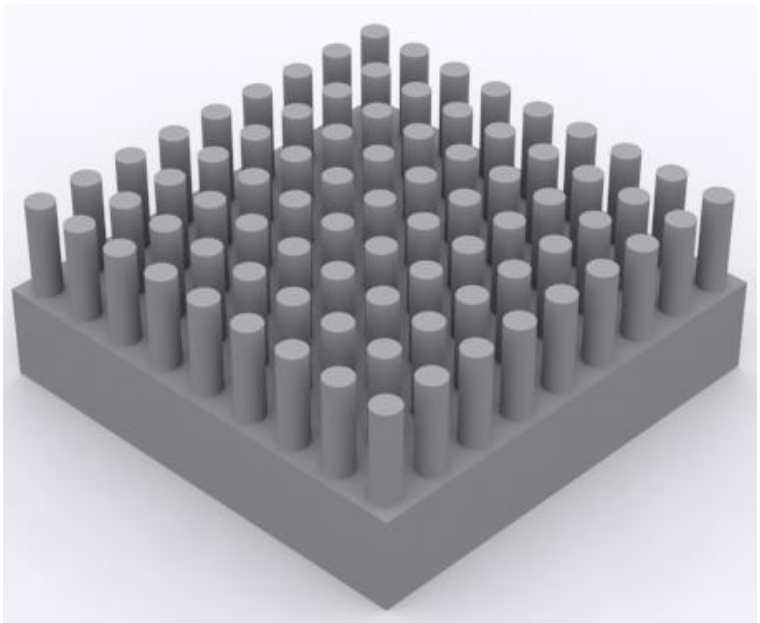

Figure 7.3. Photonic crystal structure.

Initially, a layer of photoresist is applied to the substrate. Using the LIL method, a pattern of holes is etched into the photoresist layer, effectively creating a template for the PhC structure. Following this, an ITO layer is deposited over the patterned photoresist, covering both the exposed and masked regions of the substrate. The final step involves the removal of the photoresist along with the overlying portion of the ITO layer, a process known as lift-off, which reveals the PhC structure on the substrate, as depicted in Figure 7.3. The use of LIL for patterning, followed by strategic deposition and lift-off processes, offers a viable alternative to traditional etching methods, enabling the creation of intricate PhC structures that enhance the performance of semiconductor devices.

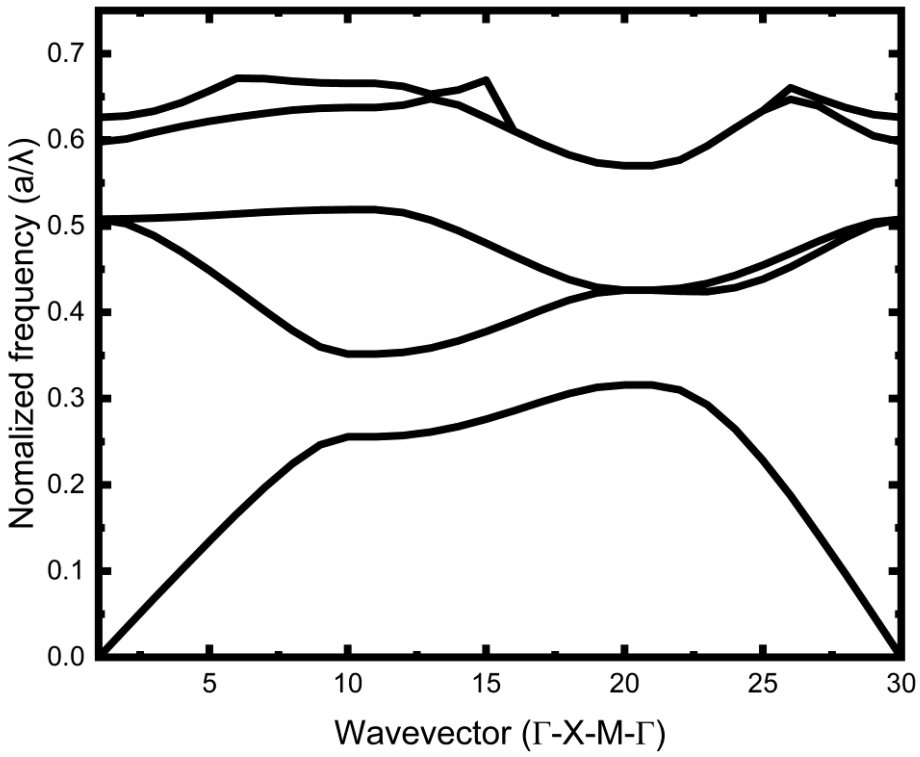

Figure 7.4. PBG for TiO_2 2D PhC structure.

The method delineated above applies to GaN-based LEDs. Given the propensity for GaN-based LEDs to emit in the visible spectrum, we must engineer 2D PhC structures with small

pitch dimensions to augment the LEE for GaN LEDs. The sample of our LED is characterized by an emission wavelength of 550 nm. Using the nanohole PhC structure directly on the GaN LED necessitates a pitch dimension of around 220 nm. Such a requirement presents considerable challenges for LIL setup. To mitigate this problem, the proposed method involves the employment of TiO_2, which possesses a higher refractive index, to fabricate nanopillar-configured PhC structures upon the GaN LED samples. Through the FDTD simulation results as shown in Fig. 7.4, when the pitch is 310 nm and the diameter of the nanopillar is 105 nm, two PBGs are generated. The first PBG is observed within the spectral domain spanning 544 to 596 nm, and the second emerges in the spectral interval ranging from 885 to 969 nm. Our GaN LED combined with TiO_2 PhC structure gives effective enhancement.